8-1994

Asymmetric Adsorbate and Substrate Interactions in Physisorbed Systems: N2 on Graphite and Dipolar Molecules on Ionic Substrates

Teresa Ellen Burns
Utah State University

ASYMMETRIC ADSORBATE AND SUBSTRATE INTERACTIONS IN PHYSISORBED SYSTEMS: N_2 ON GRAPHITE AND DIPOLAR MOLECULES ON IONIC SUBSTRATES

by

Teresa Ellen Burns

A dissertation submitted in partial fulfillment
of the requirements for the degree

of

DOCTOR OF PHILOSOPHY

in

Physics

Approved:

J R. Dennison Major Professor	D. M. Riffe Committee Member
W. N. Hansen Committee Member	J. J. Sojka Committee Member
J. L. Hubbard Committee Member	J. P. Shaver Dean of Graduate Studies

UTAH STATE UNIVERSITY
Logan, Utah

1994

To many strong and beautiful women,
especially Gran

ACKNOWLEDGMENTS

I respectfully acknowledge the help and support of my major professor, J.R. Dennison, whose undefatigable optimism and high standards have kept me hard at work, and constantly improving. Jan Sojka has been a mentor and friend since my arrival at USU; I thank him for providing me a model of the kind of physicist I want to be. I am grateful to my committee members, W.N. Hansen, J. L. Hubbard, and D.M. Riffe, for their help and encouragement. I also gratefully acknowledge W.J. Raitt, J. Wheeler, and B. Phillips for various acts of support during my tenure at USU. Full candy bowls and friendly conversation from D. Eckburg and M. Griggs made work a pleasant place to be.

There have been many people in the course of my studies who have made life a little smoother. I thank my fellow graduate students (especially R. Davies, T. Will, and N. Penley) for their comraderie, conversation, and cram sessions. My roommates and friends have provided me with a life outside my lab; for each one, I am very grateful. I especially thank T. K. Raghuram for many late nights, curry dinners, and extra hands in the lab, and Jennifer Newell for her friendship, loyalty, and example; I am a better person because of them.

Balraj Menon is a true friend and companion. I am especially grateful to him for constantly reminding me of what it means to love physics.

I especially thank my parents and family. Their encouragement and support through all my academic endeavors has made everything possible.

I am indebted to the Claude Zobell Scholarship Fund, and the Vice-

Presidential Research Fellowship Fund. This work was supported by the Utah State University Research Office, and by the Donors to the Petroleum Research Fund of the American Chemical Society.

Teresa Ellen Burns

CONTENTS

LIST OF TABLES

LIST OF FIGURES

ABSTRACT

Asymmetric Adsorbate and Substrate Interaction in Physisorbed Systems: N_2 on Graphite and Dipolar Molecules on Ionic Crystals

by

Teresa Ellen Burns, Doctor of Philosophy

Utah State University, 1994

Major Professor: Dr. J.R. Dennison
Department: Physics

Asymmetries in physisorbed systems give rise to interesting phases and phase transitions in two-dimensional (2D) monolayer and multilayer systems. The effects of asymmetric adsorbate and substrate interactions in monolayers of dipolar molecules on ionic substrates and N_2 on graphite are studied.

In the case of dipolar molecules on ionic substrates, 2D dielectric phase transitions using a modified Blume-Emery-Griffiths (BEG) model are determined theoretically. A dipole adsorbed vertically above a metal ion lattice site, and pointing up (down), is assigned a spin S=+1 (S=-1). An empty lattice site is assigned a spin S=0. Analytic solutions for both ferroelectrically and antiferroelectrically ordered systems are found. The model is applied to CO adsorbed on MgO and NaCl, and halogenated methanes on NaCl. Phase diagrams for CO on MgO and NaCl, and preliminary results for the phase diagram of CH_3F on

NaCl, are presented.

Multilayer phase transitions for N_2 on graphite are studied experimentally using synchrotron x-ray diffraction. The system is measured to undergo layering transitions, where the number of layers increases as the temperature of the system increases. A new multilayer phase diagram based on our results and the combined results published by other researchers is presented. The effects of capillary condensation on this multilayer system are quantified, and it is determined that its primary effect is to broaden the discrete layering transitions. The results for both studies are put into context with other adsorption systems with asymmetric interactions.

(241 pages)

CHAPTER I

INTRODUCTION

Physisorbed systems have been the focus of much experimental and theoretical work in the past. Simple adsorption systems, such as rare gases on graphite, are readily understood largely because the spherical symmetry of the adsorbate molecule simplifies the adsorbate–adsorbate and adsorbate–substrate interactions. Experimental and theoretical methods were used in this dissertation to explore how asymmetries in these interactions manifest themselves in the structural and thermodynamic behavior of physisorbed systems (where asymmetric interactions are defined as those which do not have spherical symmetry). For single layers of adsorbed material (monolayers), we study how asymmetric electrostatic adsorbate–adsorbate and adsorbate–substrate interactions add new dielectric ordering phases to the simple two–dimensional (2D) solid–liquid–gas phase diagrams of dipolar molecules on ionic substrates. For several layers of adsorbed material (multilayers), we study how asymmetries add orientational phase transitions to the 2D and three–dimensional (3D) phase diagrams of adsorbed gases, and how 3D phase transitions affect 2D structural and layering transitions. It is our intent to show the asymmetries in the systems studied here lead to rich 2D monolayer and multilayer phase diagrams.

As a tutorial for the unfamiliar, this chapter begins with a brief historical overview of the relevant aspects of adsorption on surfaces (Sec. A). Physisorption mechanisms, models of adsorption, and 2D monolayer and multilayer phases are discussed in Sec. B. We

discuss how asymmetries will add new phases to the monolayer (Sec. C) and multilayer (Sec. D) phase diagrams. Descriptions of the particular systems are included in these two sections.

A. Overview of adsorption on surfaces

1. What is adsorption ?

It has been known for centuries that many surfaces exposed to a gaseous environment will have gas molecules condense on them. This phenomenon was experimentally measured as early as 1777 by Fontana and Scheele, working independently.[1] Fontana observed that cooled charcoal would adsorb several times its volume of various gases. Scheele observed that gas emitted by charcoal upon heating was reabsorbed when the charcoal was cooled. From these and other simple studies, researchers realized that the volume of gas desorbed depended on both the gas and the type of charcoal used. In 1814, de Saussure proposed that the amount of gas condensed was proportional to the exposed surface area; this was the impetus for our current understanding of adsorption systems.[1]

This adsorption can be described as follows: When a surface is exposed to a gaseous environment, gas molecules will condense on the surface until an equilibrium is reached between the chemical potential of the adsorbed molecules (adatoms) and the chemical potential of the gas. This will decrease the Gibbs free energy of the system, as well as decrease the entropy of the system (the adsorbed molecules have at least one less degree of freedom). Under certain conditions, it is

energetically favorable for the molecules to condense on the surface. The surface is comprised of adsorption sites (positions where it is energetically favorable for molecules to adsorb), where the adsorption mechanism is one of two types: physical or chemical. In physical adsorption, or physisorption, the forces which bind the molecule to the surface are intermolecular or van der Waals in nature. Chemisorption involves significant charge transfer between the adsorbed molecule (adsorbate) and surface (substrate).[2]

2. What are two-dimensional systems?

In the early part of the century, Landau and Peierls showed theoretically that 2D systems of atoms exhibit very different properties than those of 3D systems.[3] 2D systems exhibit various phases (such as solid, liquid, and gaseous phases) entirely in two dimensions. These 2D phases are physically distinct from 3D phases exhibited by the bulk material (see Fig. I.1). Further interest in 2D systems was piqued by a theoretical paper by Kosterlitz and Thouless[4] which predicted a continuous melting transition in 2D systems, in contrast to the strictly first order melting transitions observed in 3D systems. These theoretical predictions prompted scientists to attempt experimental preparation of ideal 2D systems to observe the predicted behavior.

Experimental adsorption isotherm work had been used for many

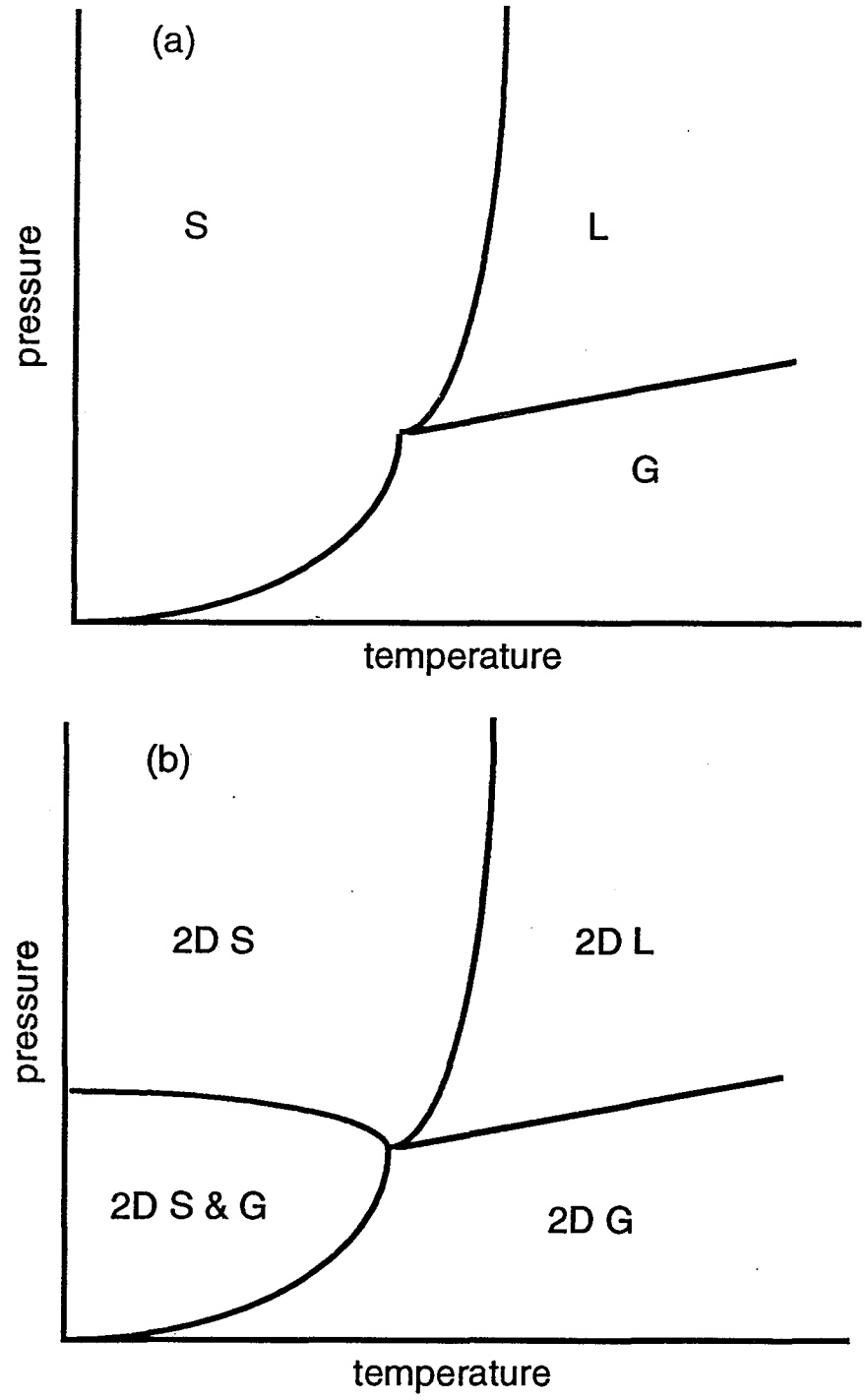

FIG. I.1. (a) Schematic bulk phase diagram for a simple material. S represents the solid phase, L is the liquid phase and G is the gaseous phase. (b) Schematic 2D phase diagram for a simple 2D monolayer. These 2D phases are physically distinct from 3D phases.

years to study physisorbed systems. However, in the late 1960's (e.g., see the work of Thomy and Duvall in 1969[5]), pure rare gases adsorbed on atomically smooth substrates were observed to exhibit a series of steps in adsorption isotherms which were attributed to formation of a series of 2D layers. The density of these adlayers is controlled at equilibrium by varying the pressure [or amount of adsorbed material (θ)] and temperature. These systems provided the first approximation to pure 2D systems, and allowed scientists to apply a myriad of techniques to probe their behavior.

3. Applications of 2D systems

Scientists have found that physisorption systems not only test the theoretically predicted behavior of ideal 2D systems, but are important to the study of adsorbate-substrate interactions and adsorbate-adsorbate interactions.[6] It is these interactions which determine the 2D phases observed in physisorbed systems and are fundamental to understanding low dimensional and surface phenomena. The 2D phase diagrams of physisorbed systems are also important in the understanding of 3D systems. The 2D systems are simpler to understand and provide clues as to how interactions cause complex phase behavior in thermodynamic systems. Additionally, adsorbate and substrate interactions play important roles in many practical applications of chemisorption phenomena, such as catalysis, surface electronics, and eptiaxial thin film growth (used in the development of new semi-conducting materials).[7] Physisorbed systems (which are considerably

more simple than any system mentioned above) provide clues to the behavior of more complex chemisorbed systems.

B. Review of physisorption

1. Mechanisms of physisorption

Adsorption is the process by which atoms (or molecules) adhere to a solid surface. There are two types of adsorption: chemisorption and physisorption. We will not study any systems here which involve chemisorption.

Physisorption occurs through van der Waals attraction between adsorbate and substrate. To understand this, let us first consider two isolated atoms (or molecules). The electron distribution of an atom (or molecule) is constantly changing due to quantum mechanical flucuations of the electron density around the atom. As the two atoms (or molecules) approach each other, the varying electron distribution of one atom (the atom appears to have a dipole moment) induces an image dipole in the other. There is an attraction between the two dipoles; the potential energy is:

$$U_{att} = -\frac{C}{r^6}, \tag{I.1}$$

where r is the distance between the dipoles (atoms), and C is a constant.[1] C is directly proportional to the product of the polarizabilities; the more polarizable the atoms, the stronger the attractive energy. As the atoms get closer together, the electron clouds of the atoms begin to overlap and the force between the atoms

becomes repulsive. One representation of the repulsive part of the potential energy is:

$$U_{rep} = \frac{b}{r^{12}}, \tag{I.2}$$

where b is an empirical constant quantifying the repulsion. Therefore, the total energy between two atoms is:

$$U = \frac{b}{r^{12}} - \frac{C}{r^{6}}. \tag{I.3}$$

The sum of U_{rep} and U_{att} is referred to as the dispersion (or Lennard-Jones 6-12) potential.[1]

These ideas are now applied to the interaction between an adsorbate (molecule) and a surface. In order to calculate the attractive energy between a molecule and a surface, one sums up the dispersion energy between a single adatom and each atom comprising the surface. This can be fairly computationally intensive for most systems, but rapid fall off of the potential at larger r and replacement of discrete substrate atoms with an effective medium (density of atoms) reduce the task. For metallic substrates, the attractive force is simply the interaction of the adatom dipole with its image charge in the substrate.[1]

For adsorbates with electric multipole moments, the situation is more complicated. In this case, electrostatic interactions will also contribute to (or perhaps dominate) the interaction energy. For example, if the admolecule has a permanent dipole moment, this dipole will interact with the surface electric field of the substrate.

Higher adsorbate multipole moments will contribute in a similar way.[1]

The most complex system considered here is the interaction of a molecule possessing electrostsatic multipole moments and a substrate with a strong surface electric field. In this case, the multipole moments interact with the strong electric field of the substrate. Additionally, the strong substrate field can induce a significant dipole moment in the adsorbate; to first order, this is superimposed on the natural dipole. Calculation of the interaction energy in this case is computationally very difficult and taxing because of the interdependence of the interactions.

To zeroth order, one can speak of the substrate electric field without making any statement about the exact details of the substrate. The surface is not, however, a smooth plane; it consists of atoms (or ions) and has a topography defined by the position of the atoms in the surface plane. Indeed, the electric field of the substrate changes as a function of position. The potential energy surface seen by an admolecule is corrugated, with positions favorable for adsorption, and those less favorable.[1] The difference between high and low potential energies is the corrugation energy. Once a molecule is adsorbed, it must acquire an energy greater than the corrugation energy to tranlate substantial distances over the surface.[1]

2. Models of adsorption

In order to understand 2D phases and phases transitions, we now study different models of adsorption and the thermodynamics which

govern adsorption systems. Imagine beginning an experiment with a clean substrate in a vacuum-tight sample cell. This sample has no molecules adsorbed on its adsorption sites. The temperature of the sample cell is controlled and the pressure of the 3D gas in diffusive equilibrium with the surface is monitored. The sample is cooled and gas is admitted to the cell to a certain pressure. Gradually the system comes into equilibrium as the pressure lowers. There is some number of gas molecules adsorbed to the surface at some pressure and temperature. This number of molecules adsorbed is determined by some appropriate function which depends on the thermodynamic variables such as pressure and temperature. This thermodynamic function can be derived from different models of adsorption, as described below.

The first model of adsorption is the kinetic theory of adsorption, originally proposed by Langmuir in 1916 for the first adsorbed layer. In 1938, Brunauer, Emmet, and Teller (BET) extended Langmuir's theory to include adsorption in the second and higher layers.[1] The model supposes that the solid surface of an adsorbate is comprised of a lattice of adsorption sites, and on each site one molecule can adsorb. When gas comes in contact with the surface, molecules from the gas attach themselves to the adsorption sites, stay there for some time, τ, and then desorb.[1] The number of molecules adsorbing to the surface is equated to the number of molecules desorbing from the surface. The "BET equation" is thus derived:

$$\theta = \frac{c(p/p_o)}{(1-p/p_o)\,(1+cp/p_o-p/p_o)}, \qquad \text{(I.4)}$$

where θ is the fraction of adsorbate sites filled, p is the pressure of the 3D gas, p_o is the saturation vapor pressure for the 3D gas at the system temperature, and c is a constant directly related to the average time an adsorbate molecule will spend in the adsorbed state. (For a complete discourse on this model, see Ref. 1, p. 36–54.)

The second model of adsorption involves purely thermodynamic considerations. Again, the substrate is a lattice of possible adsorption sites. Each of these lattice sites has an associated binding energy, i.e., when a molecule is adsorbed at a lattice site the energy of the system is changed by an amount equal to the binding energy. The number adsorbed to a clean substrate surface is determined by equating the chemical potential of the adsorbed molecules to that of the 3D gas phase adsorbate in thermal equilibrium with the surface. This leads to the Langmuir equation:

$$\theta = \frac{Bp}{1 + Bp}, \qquad \text{(I.5)}$$

where B is related to the single particle partition function, and is constant for constant temperature. For a single adsorbed layer, the BET equation reduces to the Langmuir equation.

Further layers can be described thermodynamically by the Gibbs theory of surface phenomenon. The state of the system depends on the Gibbs free energy function, which depends on the thermodynamic variables such as the pressure, temperature, and number of particles

in the adsorbed layer. The Gibbs free energy for the adsorbed layer also includes surface excess energies such as the surface tension, and surface stress and strain. The equilibrium configuration of the adsorbed layer is that which minimizes the Gibbs free energy function. (See, for example, Ref. 7, pp. 7-12.)

3. Surface (2D) phases and phase transitions

Systems of adsorbed gases can exhibit a wide variety of phases, both in the monolayer and in the multilayer phase diagrams. A monolayer can be in gas, liquid, and solid phases, with phase transitions occurring between the phases. Fig. I.1(b) illustrates a simple, idealized 2D phase diagram. These can also exhibit phases transitions between different structural (solid) states. The condensation and phase of the adsorbed state is determined by thermodynamic variables, as described above. Once adsorbed, the 2D adlayer can be solid, liquid, or gas. The gaseous phase is a low density phase with no translational order where the molecules are free to move over the surface of the substrate. The liquid phase is a higher density phase, where again adsorbate molecules are free to move over the surface; they have very limited translational order, on the order of 1 to 2 molecular spacings. A 2D solid phase occurs when the adsorbate molecules take on well-defined equilibrium positions; a 2D crystalline solid has a periodic structure in 2D.

The state of the adsorbed layer is determined by the Gibbs free energy, which includes interactions between the adsorbate molecules,

and between the adsorbate and the substrate. For a liquid layer, one expects a 2D film formation if the adsorbate-substrate interactions are sufficiently strong. However, one sees no layer formation if the adsorbate-adsorbate interactions are very much stronger than the adsorbate-substrate interactions. For solid crystalline phases, the situation is further complicated by the crystal structure of the adsorbed layer.

One of the earliest descriptions of the structure of the adsorbed state is attributed to Frank and van der Merwe.[8] This model considered the adsorbed molecules as balls connected by springs (the unstretched length determined by the adsorbate 3D cleavage plane lattice spacing), and the substrate as a periodic corrugated surface of peaks and troughs (the periodicity determined by the substrate surface lattice spacing). The lowest energy configuration exists if the balls sit at the bottom of all the troughs without any stretching of the springs which connect them. This would correspond to a complete match between a 3D lattice spacing of the adsorbed material and the lattice spacing of the substrate. However, there is usually a mismatch between these lattice constants. This mismatch manifests itself as additional energy required to stretch the springs, or to raise the balls out of the trough minima. The preferred configuration is then the one which minimizes the total energy of the springs and balls in the troughs.

More recent modeling rephrases basically the same concepts in terms of the adsorbate-adsorbate potential versus the corrugation

potential. If the equilibrium position for adsorbate molecules determined by adsorbate-adsorbate interactions is different than the equilibrium positions determined by adsorbate-substrate interactions, a commensurate to incommensurate phase transition may occur. For example, the minimum for the Lennard-Jones potential interaction between two Kr atoms is 4.04 Å; the lattice spacing between energetically preferred adsorption sites for Kr on graphite (the centers of carbon rings) is 4.26 Å.[9] The krypton on graphite system has a low temperature $\sqrt{3} \times \sqrt{3}$ commensurate phase; at higher temperature, it undergoes a phase transition to an incommensurate phase.[10] This phase transition has been successfully modeled with molecular dynamics.[11] Similar behvaior is observed for N_2, CO, and CH_4.[9] In contrast, lattice mismatch for Ne, Ar, and Xe on graphite leads to incommensurate low temperature phases.[10]

4. *Asymmetries in monolayer phases*

We now have a qualitative appreciation of the phases and phase transitions which are found for monolayers of simple (spherically symmetric) adsorbed gases. We are interested in how asymmetries can add new phases and phase transitons to the phase diagrams of simple adsorbed gases. For example, we are interested in how the simple 2D phase diagram of Fig. I.1(b) becomes more complex (e.g., see Fig. II.1 and Fig. III.8) when asymmetries are considered.

The simplest way to introduce asymmetries is to consider not spherical molecules, but ellipsoidal molecules, like N_2. For these

molecules, we have the possibility of orientational ordering, i.e., the major axes of the molecules in a fixed directional relationship to each other. For example, for N_2 on graphite, the low temperature submonolayer configuration is called herringbone, where the molecular axes are pointed almost perpendicular to each other in alternating rows.[12] This phase is actually driven by the large quadrupole moment of the N_2. Above 28 K, this orientationally ordered state makes a phase transition to an orientationally disordered state.[12] In this state, the molecules still have a fixed position with respect to the substrate (i.e., they still have a 2D crystal structure); however, the molecules are allowed to rotate rapidly.

The example of N_2 raises an important point. While the shape aymmetries allow us to assign an orientation to the molecule, it is really asymmetries in the intermolecular (e.g., electrostatic for N_2) interactions that cause the orientational ordering. The simplest asymmetric interaction to consider is the steric interaction. This asymmetry occurs when the shape of the electron cloud surrounding a molecule is not symmetric, i.e., at certain positions around the molecule, a second molecule can get "closer." Steric interactions are thought to cause a low T end-to-end orientationally ordered phase in CO on graphite (see Chapter II, Sec. G).[13,14] Also, molecular dynamics studies have determined that steric interactions are responsible for continuous melting in the hexane (a cigar-shaped long chain hydrocarbon) monolayer on graphite.[15] In this system, the molecules have a low temperature herringbone orientation with the long molecular

axis parallel to the graphite plane; at higher temperature, the structure becomes rectangular. At still higher temperature, the molecular chains begin to curl and to rise up out of the graphite plane until melting has occurred.

Electrostatic interactions are also responsible for ordering in 2D monolayers, like the quadrupole ordering mentioned above for N_2 on graphite. Quadrupole interactions favor an orientation where the quadrupole moments are perpendicular; this is realized in herringbone or pinwheel molecular ordering. Systems where quadrupole interactions cause orientationally ordered phases are CO_2, CS_2, Cl_2, C_2H_6, and CO on graphite.[9] (Note: For CO on graphite, quadrupole interactions cause the CO to have a herringbone molecular orientation; steric intractions cause end-to-end ordering.)

Another asymmetric interaction is dipole interaction within the adsorbed monolayer. Free electric dipoles prefer to be aligned antiparallel, with their dipole moments pointed in opposite directions. If a molecule with a dipole moment is adsorbed to a substrate, an orientationally ordered state can ensue due to dipole-dipole interactions. Various dipole-ordered phases are observed for the halogentated methanes adsorbed on graphite (Chapter II, Sec. G).[16,17,18]

In thinking back to Sec. B.1, if the substrate has a strong surface electric field (such as an ionic crystal), it can induce an additional dipole moment in the admolecule. The total dipole moment is then asymmetric and depends on molecular orientation with respect

to the substrate. There has not been a great deal of work on such systems. Most experimental work has focussed on CO on NaCl and MgO; understanding the behavior of these systems is the focus of Chapter II and III. Theoretical monolayer structures for methyl bromide and methyl iodide on LiF have determined high density dipole ordered states.[9] CO_2 on NaCl is seen to have a rectangular unit cell with some molecular tilting; this tilting is probably due to quadrupole interactions.[9] Interestingly, N_2 on NaCl is observed to have a vibrational spectrum very similar to that of CO.[9] It is inferred that the strong substrate electric field induces an ir active dipole moment in the N_2, which is perpendicular to the substrate.

5. Multilayer phases

As material physisorbs to a surface, one sees three different classes of film growth.[19] Class I multilayer growth is characterized by an infinite number of 2D layers condensing on a substrate before bulk formation begins. This is also called complete wetting. Class II growth or incomplete wetting is characterized by only a finite number of layers grown before bulk nucleation. Class III or non-wetting is characterized by no layers grown.[19]

At first it was believed that the wetting mode is determined by the relative strength of adsorbate-adsorbate and adsorbate-substrate interactions. If the adsorbate-adsorbate interactions were much stronger than the adsorbate-substrate interactions, then the adsorbate would most likely exhibit incomplete wetting. If the adsorbate-

substrate interactions were strong, the adsorbed layer would (completely) wet the substrate. This simple picture failed to accurately predict the wetting mode in several systems, such as Ne, Ar, Xe, and N_2 on graphite.[20] Its main deficiency is that is does not consider strain in the adsorbed film, which arises when the lattice spacings of 2D crystal structure do not match those of a cleavage plane of the 3D material.

For a complete wetting system, there is very little mismatch between the monolayer crystal structure and a 3D cleavage plane, and the system continuously approaches the 3D bulk (e.g., Ar and Xe on graphite).[20] For an incomplete wetting system, the monolayer has a structure sufficiently different from a 3D cleavage plane and a discontinuity in growth occurs, with a finite number of layers grown; additional material nucleates as bulk crystallites (e.g., Ne and N_2 on graphite).[20] For some incomplete wetting systems, the number of layers grown changes as the temperature changes.

The type of growth mode a substrate-adsorbate system exhibits is a function of the Gibbs free energy of the system. Since the Gibbs free energy is a function of temperature,[21] the equilibrium number of film layers that stabilize before bulk nucleation begins can change as the temperature changes.[22] This phenomenon is called layering. For example, an increase in the number of layers of N_2 grown on graphite for increasing temperature was observed with ellipsometry;[23] similar behavior was observed for ethylene on graphite.[24] Delayering, or a decrease in the number of film layers, at the 2D melting temperature

was observed for iron pentacarbonyl.[25]

Many adsorbate-substrate systems exhibit wetting transitions, which are usually driven by bulk structural transitions.[23] An common example is triple point wetting, where the number of layers grown approaches infinity as the adsorbate temperature reaches the bulk triple point temperature.[26] Here, the loss of 3D translational symmetry negates strain between the 2D system and the 3D system, thus allowing continuous layer by layer growth of 2D layers.[27] Systems which are strong candidates to exhibit triple point wetting include C_2H_4, Ne, N_2, O_2, and CH_4 on graphite.[27]

For asymmetric molecules, additional 3D phase transitions (other than solid-liquid-gas transitions) can exist, due to orientational ordering. For example, bulk N_2 exhibits a structural phase transition between an orientationally ordered (determined by quadrupole interactions) and orientationally disordered crystal structure[28] (such ordering is not possible for spherically symmetric rare gases). Similar bulk orientational phase transitions are observed for CO and O_2.[10] Additional 3D orientational ordering phase transitions (aside from melting and condensation) allow us to look for phase transitions in the 2D multilayer phase diagram (such as layering) which are correlated to the 3D structural phase diagram, in analogy to triple point wetting. Addressing precisely this question is the main focus of Chapter IV.

C. Asymmetric interactions in dipolar molecules on ionic substrates and N_2 on graphite

After studying (qualitatively) the general physical concepts behind physisorbed systems, and how asymmetries manifest themselves as additional phase transitions in mono- and multilayer phase diagrams of many systems, we are in a position to understand why the particular systems studied in this dissertation are interesting. This is briefly outlined in the next two subsections.

1. Dipolar molecules adsorbed on ionic crystals

For these systems, there are two different asymmetric interactions. First, the binding energy is asymmetric with respect to adsorbate dipole orientation. Secondly, the interactions between these dipoles are asymmetric; this is further complicated by induced dipole moments which arise from interaction of the molecule with the strong substrate electric field. These asymmetries allow for dipole ordering, or dielectric phases in the monolayer phase diagram.

Dielectric ordering is studied in Chapter II using a spin-1 Ising model. The problem is formulated for a general adsorbed dipolar molecule system, and applied in detail to CO adsorbed on MgO and NaCl, and preliminarily to halogenated methanes on NaCl. Phase diagrams, including dielectric phases, are determined and presented. In Chapter III, attempts to measure the structure of CO on MgO (knowledge of which is important to correctly modeling the system) using x-ray diffraction are presented. We discuss why these measurements yielded

no useful structural information.

2. N_2 on graphite

Asymmetric quadrupolar interactions cause bulk N_2 to have a structural phase transition, from an α-phase at low temperature (orientationally ordered fcc crystal) to a ß-phase (orientationally disordered hcp crystal). This order-disorder phase transition allows the bulk N_2 additional degrees of freedom. Here, in Chapter IV, we study how the 3D orientational disorder is reflected in a corresponding 2D phase transition, using x-ray diffraction of N_2 adsorbed on a graphite foam sample. The use of a foam sample raises questions about how porosity affects the measurements. These questions are also addressed.

In addition to the body of the work, two appendices are included. Appendix A describes the technique used in both of our structural studies, i.e., powder x-ray diffraction. We also detail the experimental station used at the National Synchrotron Light Source at Brookhaven National Laboratory. Appendix B describes an automated gas handling system in development. It is being built in order to experimentally address some of the issues raised in our studies of multilayer adsorbed systems.

CHAPTER II

CO ON IONIC CRYSTALS

A. Introduction

As discussed in the introduction, asymmetric adsorbate interactions, such as dipolar interactions, can lead to new phases present in the 2D phase diagram of a gas adsorbed to a solid surface. For example, a molecular species with a magnetic dipole may prefer to have its dipole aligned with its neighbors, and a ferromagnetic state would be preferred. Alternatively, adjacent electric dipoles may prefer to be anti-parallel, hence prefer antiferroelectric ordering. Also, for adsorbed dipolar molecules, binding asymmetries due to the inequivalence of the interaction of the dipole with the substrate can occur. This asymmetry will lead to adsorbate states driven by adsorbate-substrate interactions. None of these ordering states can exist for spherically symmetric adsorbates such as the rare gasses.

There are myriad interesting 2D dielectric (dipole ordering) phases and phase transitions which may occur due to asymmetric dipolar interactions; these are shown schematically for a hypothetical system in Fig. II.1. If the adsorbate-substrate interaction has a relatively strong, energetically preferred dipole orientation, a zero-temperature ferroelectric (FE) configuration is favored, i.e., a phase where all adsorbed molecules align in one orientation (see Fig. II.1). A phase transition (at T_{od}) may exist from a ferroelectric state to a spin disordered orientation state (SDO) as the temperature is increased.

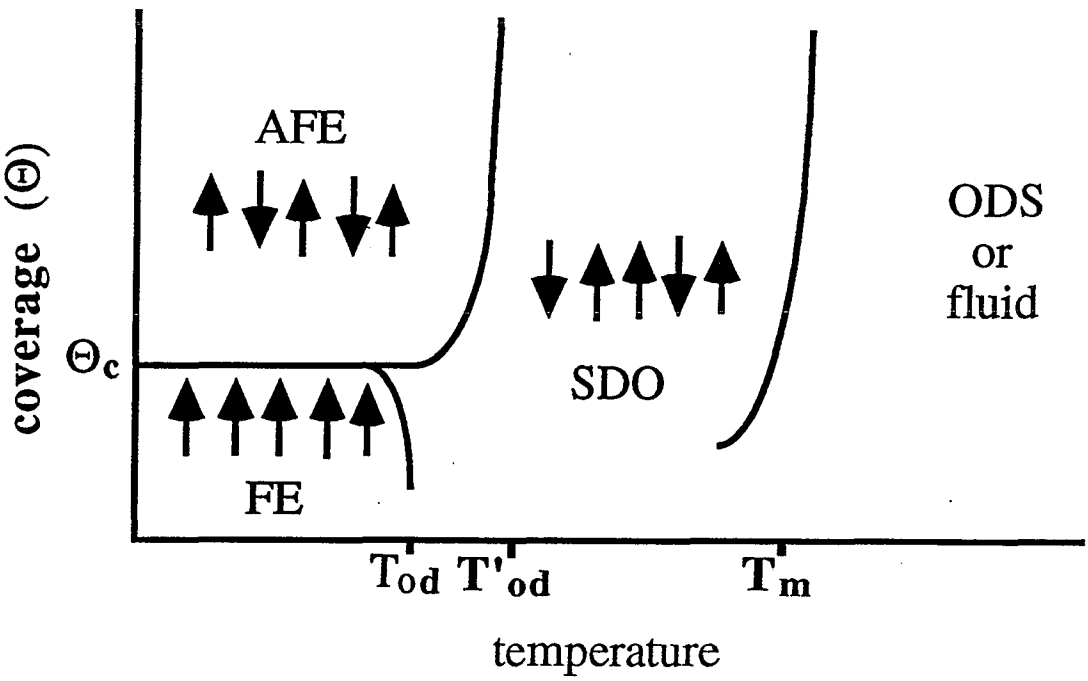

FIG. II.1. Schematic diagram of the possible phase transitions for a hypothetical lattice of perpendicular electric dipoles interacting with an external (substrate) field. AFE represents an antiferroelectric or ferrielectric phase, FE is a ferroelectric phase, SDO is a spin-disordered phase, and ODS is an orientationally disordered solid or fluid phase. The temperatures T_{od}, T'_{od}, and T_m represent the two dipole-orientation order-disordered transitions and the translational orientation order-disorder (melting) transitions, respectively.

This is analogous to a paramagnetic system, where magnetic dipoles align with an applied magnetic field at low temperature, but entropy effects destroy this order at higher T.[29] The configuration which minimizes the interaction energy for simple electric dipoles is antiferroelectric, with neighboring dipoles aligned in opposition. Thus, strong adsorbate-adsorbate dipole interactions may induce a ground state configuration which is antiferroelectric or ferrielectric (AFE). The dipole-dipole interaction energy becomes more important with decreasing separation or increasing coverage; therefore, a phase transition at low temperature from a ferroelectric state to an antiferroelectric state could occur (at θ_c), driven by increasing coverage. The antiferroelectric state may also exhibit a dipole order-disorder transition driven by temperature (at T'_{od}).

Systems such as CO adsorbed to ionic crystals are natural prototypes for the study of dipole ordering. Carbon monoxide on MgO and NaCl has been studied theoretically and experimentally. It is a diatomic molecule which has a weak permanent dipole moment.[30] It can be further polarized in the presence of an electric field, such as the substrate surface electric field associated with ionic crystals. The total electric dipole moment is, $p_{tot} = p_{nat} + p_{ind}$, where p_{nat} is the natural dipole moment of free CO, and p_{ind} is the dipole moment induced in the CO by the substrate on adsorption, which depends on orientation.[31,32] The addition of an induced dipole moment implies that the interaction energy between two neighboring molecules is dependent on the orientation of both neighbors. Further, the binding

energy is different for the situation where the CO is adsorbed C-down as opposed to O-down[31,32] in the neighbor of a substrate with a strong electric field (e.g., an ionic surface) such as magnesium oxide or NaCl. Both MgO and NaCl have a rock salt structure. The (100) faces both have square symmetry; they are composed of interpenetrating fcc anion and cation lattices each with a lattice constant a.

The spin-1 Ising model is an ideal preliminary tool to study how the asymmetric dipole-dipole and dipole-substrate interactions manifest as dipole ordered phases in the 2D phase diagram of polar adsorbates on ionic crystals. A dipole adsorbed at lattice site i is modeled as a spin where $S_i = +1$ (-1) if the dipole is pointed away (towards) the substrate. An empty lattice site is assigned $S_i = 0$. Binding asymmetries are modeled as a chemical potential which depends on spin orientation. The thermodynamic state, or ordering, is determined by minimizing the appropriate Gibbs free energy. Specific adsorbate-adsorbate and adsorbate-substrate interactions can easily be incorporated into this model, once the energies of these interactions are determined.

In this chapter, we use the spin-1 Ising model to study the dielectric 2D phases of dipolar molecules adsorbed to ionic substrates. The two main objectives of this research are: (1) to develop a simple model that predicts, for the adsorption of dipoles on a square lattice with only two allowed oreientations, the 2D dielectric phases that exist and the approximate range of transition temperatures, and (2) to test the results of the general model by

application to experimental systems. The model is applied to two dipolar physisorption systems: CO on MgO (100) and CO on NaCl (100). A preliminary extension of this model to the halogenated methanes adsorbed on NaCl is also detailed. Hamiltonians for FE and AFE ordered dipole systems are identified, and mean field equations for average spin and coverages are verified. The interaction parameters for each system are calculated, based on physical constants reported in the literature, by relating the medium-range dipole interaction energy to the expectation value of the Hamiltonian. The mean field equations are explored in a previously unmapped region of parameter space. Phase diagrams, including new dielectric phases, for these two adsorption systems are presented.

A brief history and development of the Ising model is given in Sec. B. The problem is then formulated for a general system of asymmetric adsorbed molecules (Sec. C), applied to CO on MgO and NaCl (Sec. D), and compared to the results of experiment (Sec. E). Application to other dipolar systems is discussed (Sec. G), and preliminary results for the halogenated methanes on NaCl are presented (Sec. G).

B. The Ising model

The spin-½ Ising model was originally proposed by Wilhelm Lenz in 1920. He proposed that one consider the atoms of a ferromagnetic material as elementary magnetic dipoles, which could assume one of two orientations, either in the $\theta = 0$ or $\theta = \pi$ direction (with respect to

some arbitrary coordinate system). Neighboring dipoles are either aligned in the same direction or in opposite directions. Nearest neighbor interactions determine the magnetization of the entire lattice, and hence whether a material is ferromagnetic.[33]

Mathematically, the system is described as follows: one assumes a regular lattice of magnetic dipoles. A spin of $\sigma = +½$ is assigned to a dipole aligned in the $\theta = 0$ direction and spin of $\sigma = -½$ to a dipole aligned in the $\theta = \pi$ direction. The dipoles exist in only these two orientations. Each dipole then interacts with its nearest neighbors. The interaction energy for two like dipoles is +U, and the interaction energy for two unlike dipoles is -U. The system can also interact with an external applied field, B, aligned along the $\theta = 0$ direction. The interaction of each dipole with the external field contributes $+\mu B$ if the dipole is aligned with the external field, or $-\mu B$ if the dipole is directed opposite to the applied field. The Hamiltonian for the system is:

$$H=\sum_{\langle ij\rangle} -(U\sigma_i\sigma_j) +\sum_i -(\mu B\sigma_i)\,. \qquad \text{(II.1)}$$

From this, the partition function for the system is constructed, and the existence and order of any phase transitions is determined. In particular, an order parameter, $\langle\sigma\rangle$, is defined, which specifies the net dipole orientation in the system. If this order parameter is non-zero for any finite temperature, one concludes that the material is ferromagnetic. (For a complete development of the model, see, e.g., Ref. 29.)

Ernst Ising, Lenz's student, carried out the exact calculation for the system in one dimension for no external applied field.[34] He found that there was no spontaneous magnetization expected for this system (i.e., $\langle\sigma\rangle$ was always zero). He and Lenz took this as a failure of the model and made no further progress in its development.[33] Later study proved that the 1D system indeed does not exhibit a ferromagnetic state, and that the Ising model does predict a ferromagnetic to paramagnetic phase transition for materials in two and three dimensions.

Indeed, other scientists adopted and developed the spin-½ model for application to different and varied phenomena. The spin-½ Ising model has been successfully applied to order-disorder transitions in binary alloys, the adsorption of gases on solid surfaces, as well as ferromagnetic systems.[35] The model has been solved exactly in one and two dimensions for the spin-½ system both in the absence of an external field and in the presence of a weak applied field.[29,35] The exact solution for 2D systems is somewhat cumbersome, as it involves solving nonanalytic elliptical integrals.

A significant advance in the usefulness and versatility of the spin-½ model (and spin-1 model discussed below) is the mean field approximation (MFA). In the MFA, the interaction of each spin with its nearest neighbors is replaced with the interaction of each spin with the average spin of the entire system. Physically, this asserts that the behavior of one spin is determined by the behavior of the entire system, and not necessarily only by the configuration of its

nearest neighbors. The MFA becomes exact in the limit of an infinite number of nearest neighbors, in the limit of infinite range interaction potentials (i.e., each spin interacts equally with all other spins), and for systems with dimensionality d $\geq$4.[35] This assumption allows one to find analytic solutions for the average spin of the system. For the ferromagnetic system, the magnetization, M = $\mu\langle\sigma\rangle$, is directly related to the average spin and is given by:[29]

$$M=N\mu\tanh\left(\frac{zUM}{Nk_BT\mu}\right), \qquad \text{(II.2)}$$

where z is the number of nearest neighbors (coordination number; e.g., z = 8 for a body-centered cubic crystal structure), N is the number of molecules in the lattice, k_B is Boltzmann's constant, and T is the temperature of the system. This approach leads to the Curie law for no applied field. It is the same as Weiss'[29] original description for a ferromagnetic system and leads to the Curie-Weiss law in the presence of an applied field.

One can also extend the Ising model to higher spin systems. In particular, consider a spin-1 system. This is a three state system, where the spins can take on the values +1, 0, and -1. In analogy with the spin-½ system, we expect the appropriate Hamiltonian to be a linear sum of terms which represent the interacting spins, i.e., energy constants multiplied by powers of the spin. The most general Hamiltonian we can write down for this system will have no higher than quadratic terms in spin, since cubic terms are degenerate with linear terms ($S^3 = S$).[35] The appropriate Hamiltonian is:[36]

$$\mathcal{H}_{FE}=\sum_{\langle i,j\rangle} -(JS_iS_j+KS_i^2S_j^2+L(S_iS_j^2+S_i^2S_j))+\sum_i -(\Delta S_i^2+HS_i), \qquad \text{(II.3)}$$

which includes a summation over nearest neighbor spin interactions <ij>, and a summation over all spins <i> to representing the interaction of each spin with an external field. Both terms depend on the spin orientation. S_i is the spin at lattice site i; J (bilinear interaction), K (biquadratic interaction), and L (crossed linear-quadratic interaction) are constants which are determined from the interaction energy between neighboring spins; and Δ and H are constants which represent the interaction energy between each spin and an external (applied) field. $\mathcal{H}_{FE}$ is a modified version of the Hamiltonian used by Blume *et al.*[37] to study the λ transition of ^{3}He-^{4}He mixtures (it is referred to here as a modified BEG Hamiltonian).

It is the interplay of these energy parameters which determines the phase diagram of a particular system. Physically, J is the interaction energy difference between a heterogeneous ferroelectric state (two spin domains, one all spin up and one all spin down) and a homogeneous antiferroelectric state; K is the average of the interaction energies; and L is the difference in the two ferroelectric state interaction energies. The constant Δ is the average spin-lattice site energy, and H is the difference in spin-lattice site energies due to spin orientation. [See Eqn. (II.10) for details.]

Antiferroelectric ordering can occur if $J < 0$. In this case we split the lattice of spins into two interpenetrating sublattices, u and d. The Hamiltonian becomes:

$$\mathcal{H}_{AFE}=\sum_{(i,j)} -(JS_{u_i}S_{d_j}+KS_{u_i}^2S_{u_j}^2+L(S_{u_i}S_{d_j}^2+S_{u_i}^2S_{d_j})) \\ +\sum_{i} -(\Delta(S_{u_i}^2+S_{d_j}^2)+H(S_{u_i}+S_{d_j})) . \qquad \text{(II.4)}$$

The first term is a sum over nearest neighbors <ij> for the interaction between a spin S_{ui} on the u-sublattice and a spin S_{dj} on the d-sublattice. The second term accounts for the interaction of the spins with the lattice site. AFE ordering occurs when all the spins on sublattice u are aligned with S=+1, and all the spins on sublattice d are aligned with S=−1. This is distinguished in the model from the case of a random distribution of equal numbers of each S=+1, and S=−1 on the full lattice. Hamiltonian $\mathcal{H}_{FE}$ does not distinguish these two cases.

We study $\mathcal{H}_{FE}$ and $\mathcal{H}_{AFE}$ the mean field approximation. For $\mathcal{H}_{FE}$, this collapses the sum over nearest neighbor pairs to a sum over each lattice site. We construct an approximate free energy function by minimizing the Bogoliubov inequality:[35]

$$\mathcal{F} \leq \Phi = \mathcal{F}_o + \langle H + H_o \rangle . \qquad \text{(II.5)}$$

Here, we assume that the true free energy, $\mathcal{F}$, is less than or equal to some free energy, Φ, which is composed of a trial free energy, $\mathcal{F}_o$, and H_o, a trial Hamiltonian which depends on a parameter λ (a Lagrange multiplier). We minimize the trial free energy with respect to λ to find an expression for the approximate free energy. Analytic expressions for the order parameters, $M = \langle S \rangle$ (the average spin), and $\theta = \langle S^2 \rangle$ (the average number of spins on the lattice), are thus found:[36]

$$M=\frac{2\exp(\beta(Kz\theta+LzM+\Delta))\sinh(\beta(JzM+Lz\theta+H))}{1+2\exp(\beta(LzM+Kz\theta+\Delta))\cosh(\beta(JzM+Lz\theta+H))}, \qquad [II.6(a)]$$

$$\theta=\frac{2\exp(\beta(Kz\theta+LzM+\Delta))\cosh(\beta(JzM+Lz\theta+H))}{1+2\exp(\beta(LzM+Kz\theta+\Delta))\cosh(\beta(JzM+Lz\theta+H))}. \qquad [II.6(b)]$$

The thermodynamics of the system follow from the expressions for the equilibrium free energy $\phi_E = (1/ß)\ln(1-\theta)+z(K\theta^2+2M\theta+JM^2)$, the pressure $p=-\phi_E$, and from the ratio of Eqs. [II.6(a)] and [II.6(b)]:[36]

$$M = \theta\tanh[ß(JzM+Lz\theta+H)]. \qquad (II.7)$$

For $\mathcal{H}_{AFE}$, we also make the mean field approximation, which, in this case, states that the spin on lattice site i of sublattice u interacts with the average spin of its nearest neighbors on site j of sublattice d, or equivalently $\langle S_d\rangle$ of sublattice d. The appropriate order parameters are $M_u = \langle S_u\rangle$, $\theta_u = \langle S^2_u\rangle$, $M_d = \langle S_d\rangle$, and $\theta_d = \langle S^2_d\rangle$. Analytic solutions for the order parameters are:

$$M_u=\frac{2\exp(\beta(LzM_d+Kz\theta_d+\Delta))\sinh(\beta(JzM_d+Lz\theta_d+H))}{1+2\exp(\beta(LzM_d+Kz\theta_d+\Delta))\cosh(\beta(JzM_d+Lz\theta_d+H))}, \qquad [II.8(a)]$$

$$\theta_u=\frac{2\exp(\beta(Kz\theta_d+LzM_d+\Delta))\cosh(\beta(JzM_d+Lz\theta_d+H))}{1+2\exp(\beta(LzM_d+Kz\theta_d+\Delta))\cosh(\beta(JzM_d+Lz\theta_d+H))}, \qquad [II.8(b)]$$

$$M_d=\frac{2\exp(\beta(LzM_u+Kz\theta_u+\Delta))\sinh(\beta(JzM_u+Lz\theta_u+H))}{1+2\exp(\beta(LzM_u+Kz\theta_u+\Delta))\cosh(\beta(JzM_u+Lz\theta_u+H))}, \qquad [II.8(c)]$$

$$\theta_d=\frac{2\exp(\beta(LzM_u+Kz\theta_u+\Delta))\cosh(\beta(JzM_u+Lz\theta_u+H))}{1+2\exp(\beta(LzM_u+Kz\theta_u+\Delta))\cosh(\beta(JzM_u+Lz\theta_u+H))}. \qquad [II.8(d)]$$

We determine the phases and phase transitions from the ratios of these equations for each sublattice:

$$M_u=\theta_u \tanh(\beta(JzM_d+Lz\theta_d+H)), \qquad [II.9(a)]$$

$$M_d=\theta_d \tanh(\beta(JzM_u+Lz\theta_u+H)). \qquad [II.9(b)]$$

$\mathcal{H}_{FE}$ has been studied for several different combinations of the energy coefficients. Blume *et al.*[37] solved the case where L = H = 0, and successfully applied it to the phase separation of ^{3}He and ^{4}He. Schick and Shih[38] have also successfully applied this case to the phases of a microemulsion. Lajzerowicz and Sivardiere[39] have studied this Hamiltonian extensively for many different combinations of interaction constants. Specifically, they studied the cases where J = H = L = 0, and where L = H = 0. The latter case was successfully applied to the condensation and solidification of a simple fluid. Wu investigated the case where J = L = 0.[40] The full Hamiltonian has also been studied in the mean field approximation by Sivardiere and Lajzerowicz.[36] They used numerical calculations to determine complicated phase diagrams for K > 0 and L = 0.5. While they studied a full range of J, they did not consider antiferromagnetic ordering.

Hoston and Berker[41] have studied Hamiltonian $\mathcal{H}_{AFE}$ for J < 0 and K < 0, and L = H = 0. They found complicated phase diagrams with antiferromagnetic and ferrimagnetic phases, as well as ferromagnetic phases. As discussed below, none of these studies considered parameters which describe adsorbed dipolar systems studied here.

The mean field approximation is a useful tool in describing phase transitions in physical systems to first approximation. Because

mean-field theory only takes into consideration the effect of the average of the system, it is not very accurate for systems where short-range fluctuations have significant impact on the state of the system, such as lower dimensional systems, or systems where the interactions are truly nearest neighbor. For example, mean field theory incorrectly predicts a finite critical temperature for the 1D ferromagnetic system.[35]

The simplicity of the Ising model in the mean field approximation makes it a very desirable first step in understanding any system which can be described by Hamiltonians similar $\mathcal{H}_{FE}$ or $\mathcal{H}_{AFE}$. For a 2D system, one can use this model to determine whether the physical system exhibits any phase transitions, and determine the order of the transition, and hence whether the physical system warrants study by more powerful techniques, such as numerical studies of the exact partition function, or by renormalization group theory.

C. Application of Ising model in the mean field approximation to adsorbed dipolar molecules

1. Introduction

As discussed above, monolayer adsorption of asymmetric molecules may exhibit interesting observable phases and phase transitions which depend on adsorbate orientation. In this section, we apply the spin-1 Ising model in the MFA to the adsorption of dipolar molecules on square ionic substrates. We focus on the adsorption of CO, in anticipation of detailed study of this sytem in a later section (Sec.

D). The following discussion is easily abstracted to other dipolar systems. For example, in Sec. H we discuss its application to halogenated methanes on ionic crystals.

2. Formulation of adsorbed molecules as a spin-1 model

We model the adsorption of dipolar molecules with two allowed dipole orientations as a 2D spin-lattice problem using a spin-1 Ising model.[42] In the CO on MgO and NaCl systems, we model the substrate as a square lattice of adsorption sites. We assign a spin $S_i = +1$ ($S_i = -1$) to a CO molecule adsorbed with the C-down (O-down) at a lattice site i and a spin $S_i = 0$ to an empty lattice site i [see Fig. II.2(a)]. The general spin-1 system (applied here to CO adsorbed on ionic crystals) is equivalent to the symmetrized direct product of two spin-½ systems.[36,40] Adsorption site occupation is modeled by a lattice-gas system. In the lattice-gas model, the order parameter is $\theta = \langle S^2 \rangle$; $S^2 = 0$ for an empty site, and $S^2 = 1$ for filled site, irrespective of molecular orientation. A spin-lattice system models the dipole orientation of occupied sites. The appropriate order parameter is $\langle S \rangle$; a molecule adsorbed C-down contributes +1 to the average, a molecule adsorbed O-down contributes -1, where the average is a measure of the relative amounts adsorbed C- and O-down.

For this system, the appropriate Hamiltonian is $\mathcal{H}_{FE}$ [Eq. (II.3)], because $J > 0$, as discussed below (Sec. D). The constants J, K, L, Δ, and H are linear combinations of the adsorbate-adsorbate and adsorbate-substrate interaction energies, and are defined as follows:

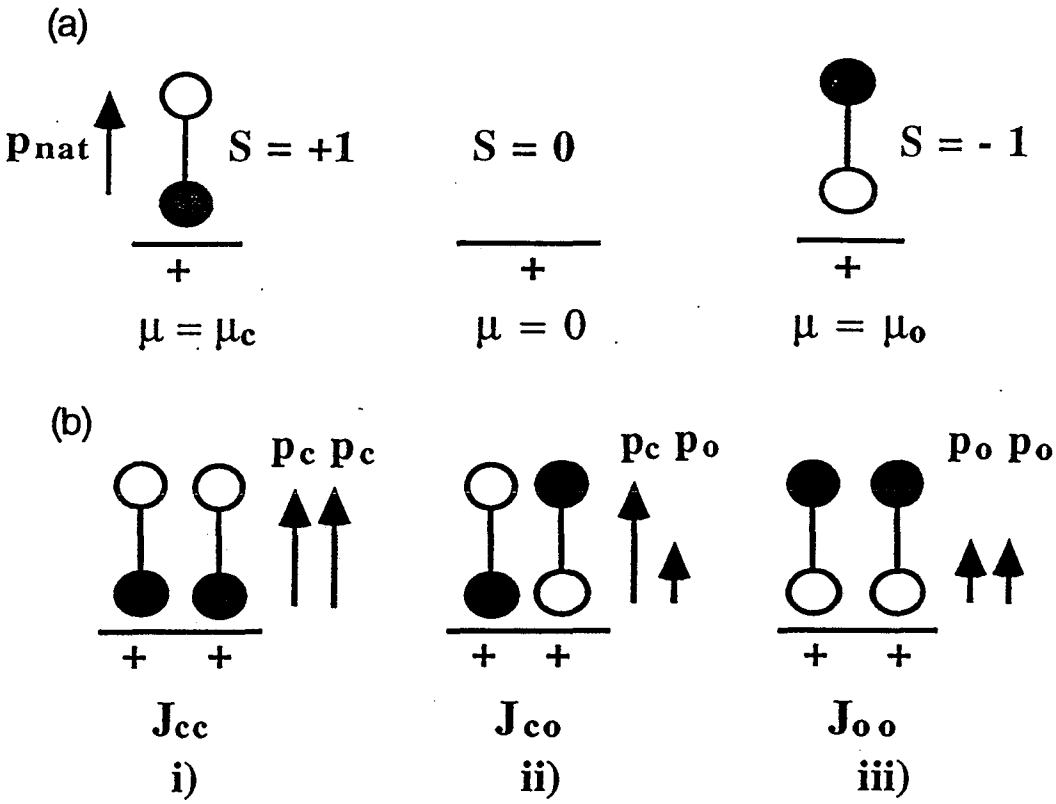

FIG. II.2. (a) Spin assignment for CO adsorbed vertically above a cation lattice site (+) on an ionic crystal surface. The circles represent C(●) and O (○) atoms. (b) Dipole and molecular orientations for the three configurations of CO adsorbed vertically above metal ion lattice sites on ionic crystal surfaces.

$$J = \tfrac{1}{4}(J_{cc} + J_{oo} - 2J_{co}),$$

$$K = \tfrac{1}{4}(J_{cc} + J_{oo} + 2J_{co}),$$

$$L = \tfrac{1}{4}(J_{cc} - J_{oo}), \qquad \text{(II.10)}$$

$$\Delta = \tfrac{1}{2}(\mu_c + \mu_o), \text{ and}$$

$$H = \tfrac{1}{2}(\mu_c - \mu_o).$$

J_{cc} (J_{oo}) is the interaction energy between two neighboring molecules adsorbed C-down (O-down) [see Fig. II.2(b) i) and iii)], J_{co} is the interaction energy between neighboring CO molecules adsorbed in opposite directions [one C-down and one O-down, as in Fig. II.2(b) ii)], and μ_c (μ_o) is the chemical potential of a molecule adsorbed C-down (O-down) [Fig. II.1(a)].

We study $\mathcal{H}_{FE}$ in the mean field approximation. Since the interaction energy of any individual admolecule is assumed to depend only on the average dipole orientation, the interaction parameters J_{cc}, J_{oo}, and J_{co} can be related to the long-range interaction energy function per particle. To calculate this, let us separate the Hamiltonian into two parts: $\mathcal{H}_{int}$ and $\mathcal{H}_{sub}$. $\mathcal{H}_{int}$ is the part of the Hamiltonian which represents the adsorbate-adsorbate interactions, and $\mathcal{H}_{sub}$ represents the adsorbate-substrate interactions. In the mean field approximation, we replace the sum over exact nearest neighbor interactions with the interaction of each spin with the average spin of the entire lattice. We then take the expectation value of the interaction energy per molecule, U_{int}. From Eq. (II.3), we find:[39]

$$U_{int} = \langle \mathcal{H}_{int}(\langle S \rangle, \langle S^2 \rangle) \rangle / N = -z\{J\langle S \rangle^2 + 2L\langle S^2 \rangle\langle S \rangle + K\langle S^2 \rangle^2\}, \qquad \text{(II.11)}$$

where U_{int} is determined by the long-range interaction energies of the adsorbed molecules.[43]

3. Energy parameters and possible phase transitions for adsorbed systems

While the Hamiltonian $\mathcal{H}_{FE}$ has been studied in the MFA for a variety of energy parameters, none of the studies considered energy parameters which fully describe the adsorption systems examined here. For the application to adsorption, the binding energy is always attractive, so that μ_c, $\mu_o > 0$, Δ is always positive definite, and one can always choose the S = +1 state such that $\mu_c > \mu_o$ and H is nonnegative. However, the interactions represented by J_{cc}, J_{oo}, and J_{co} can each be in general either attractive or repulsive, so that J, K, and L may take on any combination of signs. For application to CO on ionic crystals, Δ,H $\gg$ 0 and J > 0 and K,L < 0, since $0 > J_{cc} > J_{co} > J_{oo}$, as discussed below.

To illustrate how the interplay of the energy parameters determines the adsorbed phase of the system, consider the possible ground states at zero temperature. For dipolar adsorption, L = 0 ($J_{cc} = J_{oo}$) implies there is no interaction energy asymmetry (e.g., no induced dipoles), while H = 0 implies the binding energy is independent of dipole orientation. When H$\gg$|J| or |L|, binding energy asymmetries dominate and a ferroelectric ground state occurs. However, in the regime where H<|J| or |L|, more phases are possible. If the interaction energies for the three possible dipole pair orientations are equal ($J_{co} = J_{oo} = J_{cc}$), then J = 0 and L = 0

(originally studied by Yang and Lee[44]). In this case, only the binding energies depend on dipole alignment. In the limit $H \to 0_+$ with $J = L = 0$, $\mathcal{H}_{FE}$ becomes symmetric in spin orientation and no dipole ordering will occur. If $J > 0$ ($J_{oo} + J_{cc} > 2J_{co}$), a ferroelectric state is expected when one spin orientation is energetically preferred over another ($L \neq 0$ or $H \neq 0$).

If $H \approx L$ (i.e., the binding and interaction energies are of comparable value), one may observe a low temperature, low coverage ferroelectric state determined by binding asymmetry, which crosses over to the other ferroelectric state favored by dipole interactions as the coverage increases (separation decreases), and dipole interaction becomes more important. This would occur as the argument of the tanh in Eq. (II.7) changes sign, e.g., as the terms in J and L overcome H. J and L are functions of adsorbate interaction and increase as the coverage increases, while H is (nominally) independent of coverage. Such a transition could be observable in systems with strong dipoles (i.e., large J) that are relatively weakly bound to the substrate.

Antiferroelectric or ferrielectric states require $J < 0$ ($2J_{co} > J_{oo} + J_{cc}$). This implies that the interaction energy between two opposed dipoles [see Fig. II.2(b) ii)] is less than the average interaction energy between two dipoles in alignment with either orientation [Figs. II.2(b) i) & iii)]. The appropriate Hamiltonian is $\mathcal{H}_{AFE}$. If $J \approx H$, the low coverage, low temperature phase may be the ferroelectric phase favored by binding asymmetry. As the coverage

increases, the system may make a transtitons from this ferroelectric phase to the antiferroelectric phase favored by dipole interactions.

D. Application to CO on NaCl (100) and CO on MgO (100)

We now focus our attention on two specific systems: the adsorption of dipolar CO physisorbed to NaCl (100) and MgO (100). Before applying the model to determine the 2D dielectric phases and phase transitions for the two systems, we must first determine the energy parameters in Eq. (II.10) and verify that our simple model is applicable to CO on NaCl and MgO.

1. Determination of substrate field strength parameters

H can be determined from binding energy calculations, by relating the binding energy to the chemical potential of a molecule adsorbed to the substrate. As discussed above, the CO binding energy is dependent on adsorbate orientation and on adsorbate position above the substrate, due to the substrate potential corrugation. To fulfill the model requirement of only two allowed energy states, we restrict our application to vertical adsorption above only cation sites. This restriction is consistent, for the most part, with the limited available data of the structure of the two systems, as discussed below.

Both MgO and NaCl have a rock salt structure,[45] with lattice constants a = 4.21 Å and 5.64 Å, respectively. CO adsorbs to the NaCl (100) surface with the CO bond axis perpendicular to the surface.[46,47]

The heat of adsorption has been measured.[46,48,49] Several theoretical studies have predicted that adsorption above Na^+ lattice sites is perpendicular,[48-51] and have determined different binding energies for the C-down and O-down orientations.[31,48] For the CO on NaCl (100) interactions, we use binding energies for both orientations calculated by Gready *et al.*[31] (see Table II.1).

Theoretical studies of CO adsorbed on MgO(100) have shown that the most energetically favored position for adsorption is above a Mg^{++} site and that the CO bond axis is perpendicular to the surface at these sites.[52-54] The positions above the O^{--} and the Mg::O bonds are energetically disallowed.[53,54] Other studies have mapped out the potential energy surface of the MgO as seen by a monolayer of CO.[54] These studies find that the Mg^{++} troughs are essentially potential energy minima. The CO can adsorb anywhere along the trough. It will prefer to lie parallel to the surface in all positions except when adsorbed above the Mg^{++} lattice sites. Here it will adsorb perpendicular to the surface. Theoretical studies have also determined binding energies which depend on vertical orientation.[32,52,53,55,56] For CO on MgO, a wide range of binding energies is reported in the literature. We will apply our model to an upper limit[53b] and a lower limit[52] on the difference in binding energies for the two orientations (Table II.1). Dovesi *et al.*[52] calculated the lower limit energies as a function of coverage.

For the CO on MgO system, LEED studies found a series of uniaxially compressed, higher-order commensurate structures with

TABLE II.1. Binding energies of CO on NaCl (100) and MgO (100) as a function of orientation and coverage (θ).

	NaCl (eV)[a]	MgO		
		Lower Limit[b]		Upper Limit[c] (eV)
		θ	(eV)	
C-down	0.417	0.5	0.179	0.390
		≤ 0.25	0.194	
O-down	0.171	0.5	0.143	0.273
		≤ 0.25	0.184	

[a] Ref. 31.
[b] Ref. 52.
[c] Ref. 53b.

TABLE II.2. Natural and induced dipole moments of CO as a function of orientation.

	NaCl		MgO	
	Natural	Induced	Natural	Induced
C-down	+0.112D[a,b]	+ 0.29D[c]	+ 0.112D[b]	+ 0.49D[d]
O-down	-0.112D[b]	+ 0.29D[c]	- 0.112D[b]	+ 0.58D[d]

[a] 1 D = 3.336×10^{-30} C-m
[b] Ref. 30.
[c] Ref. 31.
[d] Ref. 32.

increasing coverages $\theta > 0.5$ ML as T decreased.[57] ($\theta = 1$ ML is defined as a coverage of one CO molecule for every cation site.) Some CO molecule tilting is inferred from these LEED studies.[57] These results are consistent with theoretical studies which determined that the Mg^{++} troughs are essentially potential energy minima for CO adsorption.[54] These observed adsorbed phases are inconsistent with our simple model where adsorption is restricted to cation sites. This proves not to be problematic because our analysis of the adsorbate-adsorbate interaction potential in Sec. D.3 limits the applicable region of our model to $\theta \leq 0.5$ ML.

2. Determination of adsorbate interaction energy parameters

Carbon monoxide is an asymmetric, diatomic molecule with a weak permanent dipole moment, p_{nat}[30] (see Table II.2) and a strong quadrupole moment ($q = 8.34 \times 10^{-40}$ C-m^2).[58] The total electric dipole moment of adsorbed CO is determined by the linear combination of the natural and induced dipole, such that $p_{tot} = p_{nat} + p_{ind}$, where p_{ind} is the dipole moment induced in the CO by the substrate surface electric field. The total dipole moment, and hence the interaction energy between CO admolecules, depends on dipole orientation.[31,32]

U_{int} is determined by taking the expectation value of the interaction energy per molecule [see Eq. (II.11)]:

$$U_{int} = \langle \mathcal{H}_{int}(M,\theta) \rangle / N = -z(JM^2 + 2LM\theta + K\theta^2). \qquad \text{(II.12)}$$

To determine the interaction energy parameters J, K, and L in the MFA, the interaction potential U_{int} is calculated for a series of fully

occupied square lattices. This energy is then equated to the expectation value of the interaction energy, and related to the interaction constants in the Hamiltonian. For example, for θ=1:

$$U_{int}(M) = \begin{cases} -z\,(J+2L+K) = -zJ_{cc} & ; M=+1 \\ -z\,K = -z\,\tfrac{1}{4}(J_{cc}+J_{oo}+2J_{co}) & ; M=0 \\ -z\,(J-2L+K) = -zJ_{oo} & ; M=-1. \end{cases} \qquad \text{(II.13)}$$

This yield three equations and three unknowns from which one determines the interaction constants. Our simple expressions for U_{int} (described below) are evaluated only for fully occupied square lattices (superlattices) because of the restriction of adsorption to cation lattice sites. It is only at these sites that we have knowledge of both the binding energy and induced dipole moments.

Physically, it is plausible to expect submonolayer growth to occur as a series of increasing density phases of fully occupied square lattices. The repulsive nature of the CO-CO interactions should favor dilute adsorption, rather growth of islands of denser structural phases. The growth mode in the submonolayer region for CO on NaCl has been inferred from ir spectroscopy to follow the Langmuir model, with random adsorbate distribution over the substrate lattice.[49] A similar growth mode is expected for CO on MgO, but has not yet been measured.

The interaction potential U_{int} was taken as the sum of a dipole-dipole interaction U_{dipole}, a quadrupole-quadrupole interaction U_{quad}, and a dispersion (hard-core repulsion) interaction U_{disp}. U_{dipole} is the interaction energy for a central electric dipole with a lattice of

dipoles. For classical dipoles (in SI units), it has the following form:

$$U_{dipole} = \frac{p_1 p_2}{4\pi\epsilon_o}\left[\sum_{n=1}^{N}\frac{1}{r_n^3} + \left(\frac{2\pi}{a^3}\right)\left(\frac{\pi}{N}\right)^{\frac{1}{2}}\right], \qquad \text{(II.13)}$$

where p_1 and p_2 are the electric dipole moments for the interacting molecules, r_n is the dipole separation, a is the superlattice spacing, N is the number of dipoles treated exactly, and ϵ_o is the permittivity of free space. The first term is a pairwise sum of the interaction of a central dipole with the dipoles in the first 21 nearest neighbor shells (N = 128). We treat the interaction exactly for these pairs. The second term is an effective medium correction for the rest of an infinite lattice. It is derived by replacing the discrete dipoles outside the Nth nearest neighbor shell with a density of dipoles. The sum becomes an integral from r_{min} to infinity. r_{min} is determined by normalizing the dipole density so that the density of dipoles inside r_{min} times the area of the lattice inside r_{min} is equal to the number (N) of dipoles inside r_{min}. U_{dipole} is attractive if the dipoles are aligned in opposite directions, and repulsive if the two dipoles point in the same direction. Because CO adsorbed C-down or O-down has a different dipole moment (as quantified below), the interaction energy will be different for two CO molecules adsorbed C-down, for two molecules adsorbed O-down, and for one adsorbed C-down and one adsorbed O-down. This is apparent from the form of the interaction energy.

U_{quad} is the interaction energy of a central quadrupole with an

infinite lattice of quadrupoles. It is independent of orientation for linear quadrupoles restricted to parallel orientation, such as is the case for CO restricted to vertical adsorption. For classical quadrupoles, it has the following form:

$$U_{quad} = \frac{q_1 q_2}{4\pi\epsilon_o}\left[\sum_{n=1}^{N}\frac{1}{r_n^5} + \left(\frac{2\pi}{a^5}\right)\left(\frac{\pi}{N}\right)^{\frac{1}{2}}\right], \qquad \text{(II.14)}$$

where q_1 and q_2 are the electric quadrupole moments for the interacting molecules. As in the case of the dipoles, the first term is an exact treatment for the first 21 nearest neighbor shells, with an effective medium correction (the second term) for the rest of an infinite lattice. In this preliminary study, we treat the adsorbed CO as classical linear quadrupoles. It is assumed that the quadrupole moment is independent of dipole orientation, and use the value published for free CO. These assumptions may not be strictly true for the physical systems; however, the intent is to get an order of magnitude approximation of the quadrupole interaction energies in order to gauge at what separations these interactions become important. This information is important because quadrupole interactions tend to tilt the molecules, which can introduce more than two orientational states, and which is inconsistent with our simple model. Quadrupole interactions have a shorter range than dipole interactions, and become significant only at higher coverages where admolecule separation is reduced. (Note: the dipole–quadrupole interaction is identically zero for a linear quadrupole aligned parallel to a dipole, as is the case in our model.)

The repulsive dispersion energy, U_{disp}, arises from the finite extent of the CO molecules (see Chap. I, Sec. B.1). The form of this force is empirical; mathematically, it is expressed:

$$U_{disp} = B\, e^{-cr}, \tag{II.16}$$

where B (= 3.16 x 10^6 kcal mol^{-1}) and c (= 4.138 $Å^{-1}$) are empirical fitting parameters, determined by Ben-Ephraim *et al.*,[59] and r is the CO separation. We calculate this for a central CO interacting with its nearest neighbors only, because this force falls off rapidly; this does not introduce significant error.

U_{int} was evaluated in two ways. First, U_{int}, U_{dipole}, U_{quad}, and U_{disp} were calculated for CO coverages corresponding to CO separations from 0.02a to 10a in 0.02a increments (a = substrate lattice constant) for the three specific dipole configurations: a lattice with all molecules adsorbed C-down, a lattice with all molecules adsorbed O-down, and an antiferroelectric lattice. This is done to determine the dominant energy term for a wide range of CO coverages. We want to compare U_{dipole}, U_{quad}, and U_{disp} to determine at what CO coverage (to the resolution of the study) U_{quad} and U_{disp} become comparable to U_{dipole}. This determines the range of validity of the assumption of vertical adsorption. We also compare U_{int} to the binding energies. When U_{int} becomes greater than the binding energies, we no longer expect an adsorbed state. Second, U_{int} was calculated for several superlattice structures of decreasing coverage on both MgO and NaCl (see Table II.3). U_{cF} is the dipole interaction energy for the all C-down (M = +1) ferroelectric lattice, U_{oF} for the all O-down (M = -1)

TABLE II.3. CO-CO interaction energies for (a) CO on MgO and (b) CO on NaCl as a function of coverage, Θ. The commensurate superlattice structure corresponding to each coverage is listed in parentheses. U_{cF}, U_{oF}, and U_{AF} are the dipole interaction energies U_{dipole} of all C-down ferroelectric, all O-down ferroelectric, and antiferroelectric infinite lattices, respectively. U_{quad} is the quadrupole-quadrupole interaction energy for the CO molecules. U_{disp} is the dispersion (hard-core repulsion) energy between two neighboring CO molecules. The relation of the total interaction energy $U_{int} = U_{dipole} + U_{quad} + U_{disp}$ to the interaction energy parameters J_{cc}, J_{co}, and J_{oo} or J, K, and L is described in the text [see Eq. (II.12)].

(a)

Coverage Θ (ML)	U_{cF} (meV)	U_{AF} meV)	U_{oF} (meV)	U_{quad} (meV)	U_{disp} (meV)
1 (1 x 1)	74.9	63.1	43.5	95.1	474
0.5 ($\sqrt{2}$ x $\sqrt{2}$)	26.4	22.2	15.3	16.7	2.55
0.25 (2 x 2)	9.37	7.89	5.44	2.97	0.002
0.125 ($2\sqrt{2}$x$2\sqrt{2}$)	3.30	2.78	1.92	0.52	$< 10^{-5}$
0.111 (3 x 3)	2.77	2.33	1.61	0.39	$< 10^{-5}$
0.063 (4 x 4)	1.17	0.99	0.68	0.09	$< 10^{-5}$

(b)

Coverage Θ (ML)	U_{cF} (meV)	U_{AF} meV)	U_{oF} (meV)	U_{quad} (meV)	U_{disp} (meV)
1 (1 x 1)	12.8	8.02	2.56	19.6	4.47
0.5 ($\sqrt{2}$ x $\sqrt{2}$)	4.54	2.84	0.91	3.48	0.003
0.25 (2 x 2)	1.60	1.00	0.32	0.613	$< 10^{-6}$
0.125 ($2\sqrt{2}$x$2\sqrt{2}$)	0.57	0.36	0.11	0.108	$< 10^{-6}$
0.111 (3 x 3)	0.48	0.30	0.095	0.081	$< 10^{-6}$
0.063 (4 x 4)	0.20	0.13	0.040	0.019	$< 10^{-6}$

ferroelectric lattice, and U_{AF} for the antiferroelectric (M = 0) lattice. Note that there are an infinite number of lattice configurations where M=0. The mean field approximation for J>0 does not distinguish them.

All calculations were done for infinite lattices. For each lattice, a central molecule was allowed to interact exactly according to Eqs. (II.14), (II.15), and (II.16) with discrete molecules positioned on the first 21 nearest neighbor shells. At larger radii, an effective medium integral correction is used. In order to determine the approximate error introduced by this correction, we plot the exact dipole interaction energy, the integral correction to the dipole energy, and the total dipole energy as a function of the number of nearest neighbor shells treated exactly (nearest neighbor shell cutoff), for the ferroelectric 0-down latticefor $\theta = 1$ on MgO (see Fig. II.3). We find that by 42 nearest neighbor shells, the energy has virtually converged. At 21 nearest neighbors, the energy differs by about 3% from the value at 42 nearest neighbors. This relative error is the same for all dipole configurations, as the dipole moments can be factored out of the sum and correction term [see Eq. (II.14)]. The relative error for the quadrupole moment interaction energy, should be smaller still, as the quadrupole interaction falls off more rapidly than the dipole interaction energy.

Calculations for these three orientation configurations uniquely determine the three interaction energy parameters at a fixed coverage, as given in Eq. (II.13). For CO on NaCl, the induced dipole moments

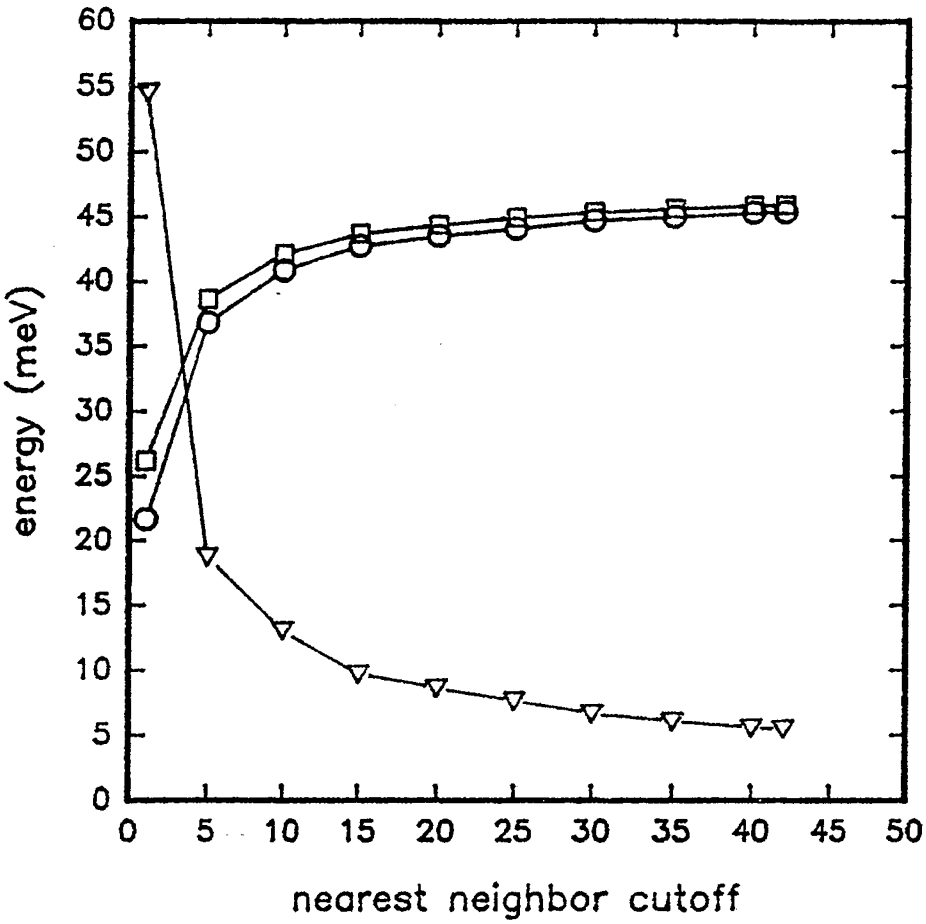

FIG.II.3. The interaction potential for U_{dip} (○), U_{corr} (▽), and U_{diptot} (□) as a function of nearest neighbor shell cutoff.

were calculated from the polarization contribution to the total binding energy of the CO molecule.[31] The energy of the polarization contribution is related to the dipole moment through:

$$E = \frac{p_{ind}^2}{\alpha}, \qquad \text{(II.17)}$$

where E is the contribution to the total binding energy due to CO polarization, and α is the polarizability of the CO molecule. From this equation, an induced dipole moment is calculated, and a total dipole moment (which depends on orientation) is determined by the linear superposition of the induced and natural dipole moment.

For CO on MgO, Pacchioni *et al.* calculated induced dipolemoments which depend on vertical orientation.[32] Again, a linear superposition of the induced dipole moment and the natural dipole moment determine the total dipole moment.

For both MgO and NaCl and for both vertical orientations, $p_{ind} > p_{nat}$; that is, the induced dipole is always greater than natural dipole, and the total dipole moment always points away from the crystal surface [see Fig. II.2(b)]. Also, we note that the total dipole moment for the C-down orientation is larger than p_{tot} for the O-down orientation for both substrates. This is because the induced dipole enhances the natural dipole in the C-down orientation. From the magnitudes and directions of the total dipole moments, we infer that all dipole interactions are repulsive such that $0>J_{cc}>J_{co}>J_{oo}$ for all orientations of the admolecules, and that an antiferroelectric or ferrielectric state is not energetically favored. Indeed, the dipole

interactions would be minimized by a ferroelectric state with all CO molecules adsorbed O-down.

3. Results of the interaction energy calculations

The results of the interaction energy calculations are presented in Figures II.4-II.9. Each figure is a portion of the energy versus CO coverage curves calculated for the three orientations. Figure II.4(a) compares the interaction energies to the binding energies for CO adsorbed to MgO in the C-down orientation, and Fig. II.4(b) details where the interaction energies become comparable to each other. Similarly, the O-down orientation and the antiferroelectric orientation on MgO are presented in Fig. II.5 and II.6. Figures II.7-II.9 are identical plots for CO on NaCl, for the C-down ferroelectric orientation, the O-down ferroelectric orientation, and the antiferroelectric orientation, respectively. All the plots have the same general trends, and expected behavior; i.e., the dipole energy is greater than the quadrupole and dispersion energies at large radius, and the quadrupole and dispersion energies dominate at smaller radius. All of the energies increase as the radius decreases.

Let us consider the dispersion energy. This energy is independent of dipole orientation, and therefore is the same curve for all three adsorbed lattice configurations considered. For CO adsorbed on MgO(100), U_{disp} becomes greater than the O-down binding energy at θ = 0.95 ML and greater than the C-down binding energy at θ = 1.01 [see Fig. II.4(a), II.5(a), or II.6(a)]. This implies that for CO on MgO,

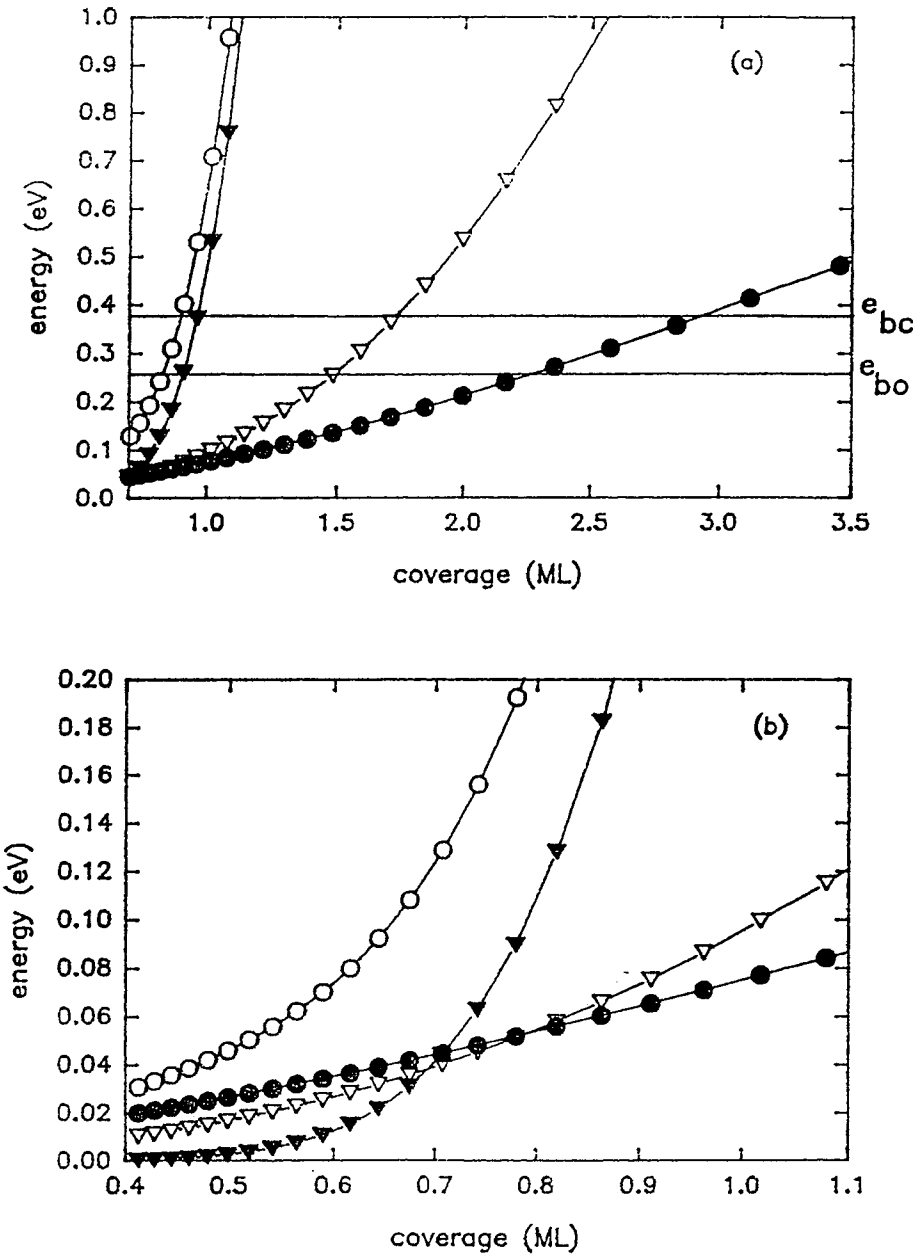

FIG. II.4. (a) Plot of interaction energies versus coverage for a lattice of CO molecules adsorbed all C-down on MgO in the range where the interaction energies [U_{tot} (O), U_{dipole} (●), U_{quad} (▽), and U_{disp} (▾)] become comparable to the binding energy. The horizontal lines indicate the binding energies of a C-down (e_{bc}) and an O-down (e_{bo}) molecule adsorbed vertically above a metal ion site. (b) Plot of the interaction energies [U_{tot} (O), U_{dipole} (●), U_{quad} (▽), and U_{disp} (▾)] in the coverage range where they become comparable to each other.

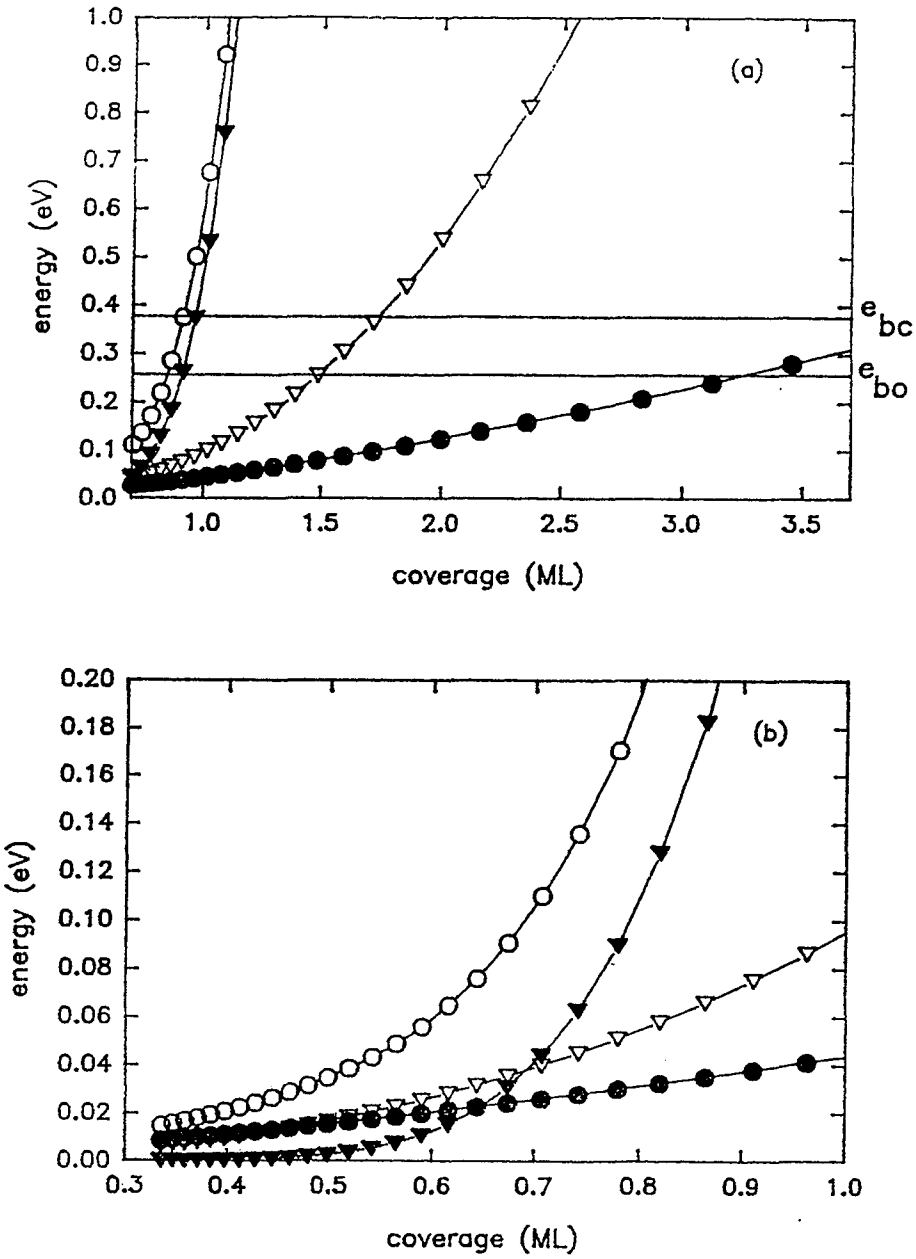

FIG. II.5. (a) Plot of interaction energies versus coverage for a lattice of CO molecules adsorbed all O-down on MgO in the range where the interaction energies [U_{tot} (O), U_{dipole} (●), U_{quad} (▽), and U_{disp} (▾)] become comparable to the binding energy. The horizontal lines indicate the binding energies of a C-down (e_{bc}) and an O-down (e_{bo}) molecule adsorbed vertically above a metal ion site. (b) Plot of the interaction energies [U_{tot} (O), U_{dipole} (●), U_{quad} (▽), and U_{disp} (▾)] in the coverage range where they become comparable to each other.

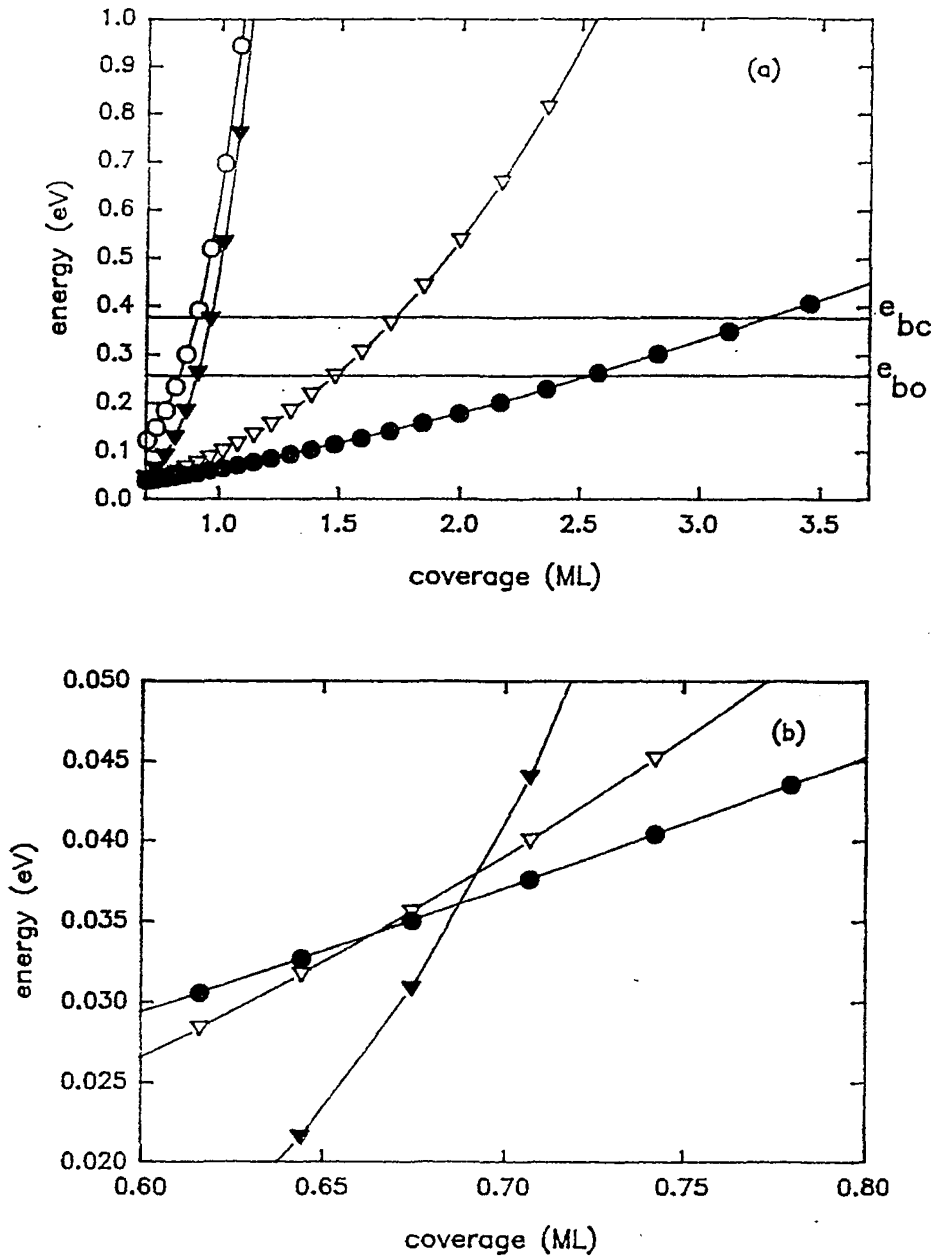

FIG. II.6. (a) Plot of interaction energies versus coverage for a lattice of CO molecules adsorbed alternating C-down and O-down on MgO in the range where the interaction energies [U_{tot} (O), U_{dipole} (●), U_{quad} (▽), and U_{disp} (▾)] become comparable to the binding energy. The horizontal lines indicate the binding energies of a C-down (e_{bc}) and an O-down (e_{bo}) molecule adsorbed vertically above a metal ion site. (b) Plot of the interaction energies [U_{tot} (O), U_{dipole} (●), U_{quad} (▽), and U_{disp} (▾)] in the coverage range where they become comparable to each other.

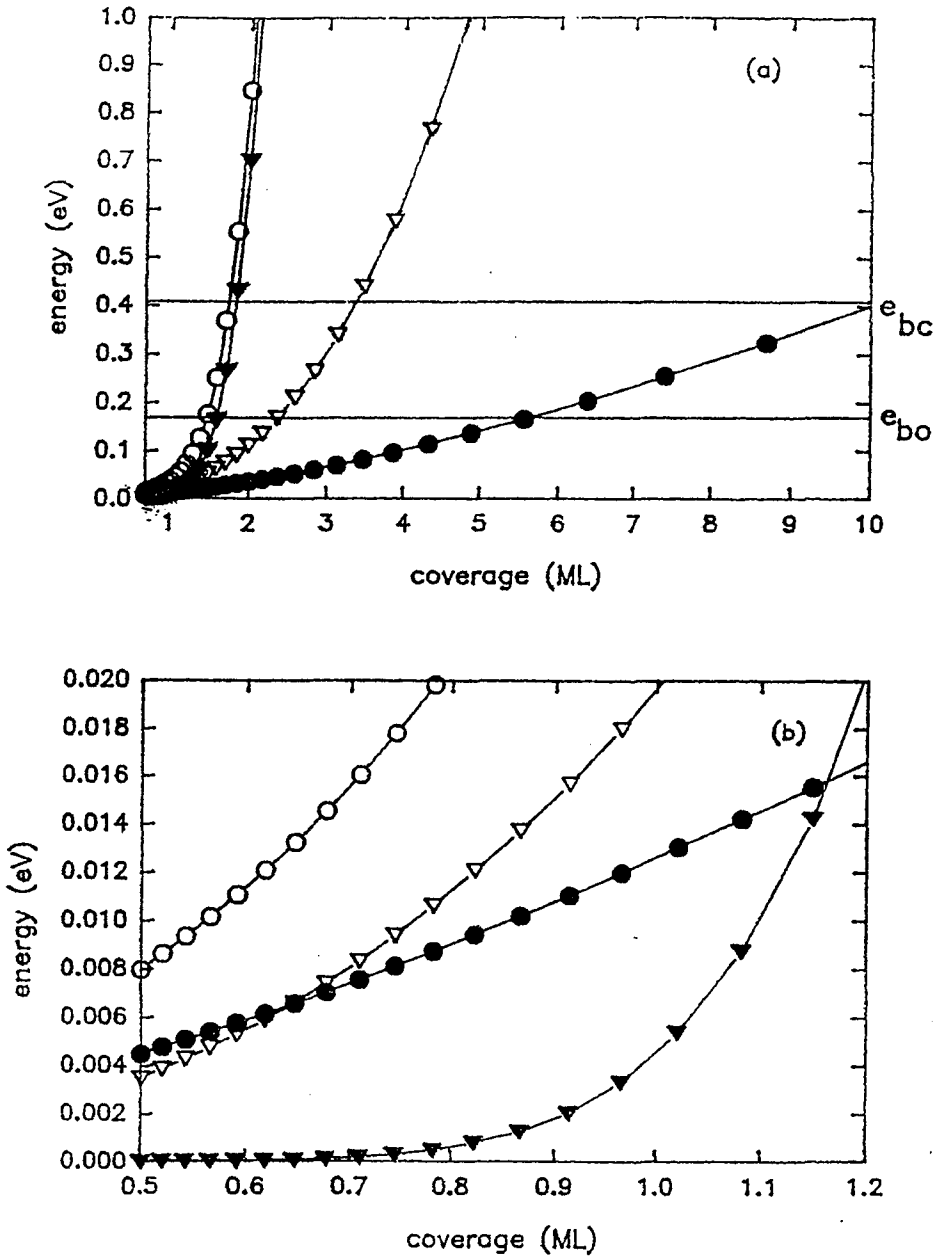

FIG. II.7. (a) Plot of interaction energies versus coverage for a lattice of CO molecules adsorbed all C-down on NaCl in the range where the interaction energies [U_{tot} (O), U_{dipole} (●), U_{quad} (v), and U_{disp} (▾)] become comparable to the binding energy. The horizontal lines indicate the binding energies of a C-down (e_{bc}) and an O-down (e_{bo}) molecule adsorbed vertically above a metal ion site. (b) Plot of the interaction energies [U_{tot} (O), U_{dipole} (●), U_{quad} (v), and U_{disp} (▾)] in the coverage range where they become comparable to each other.

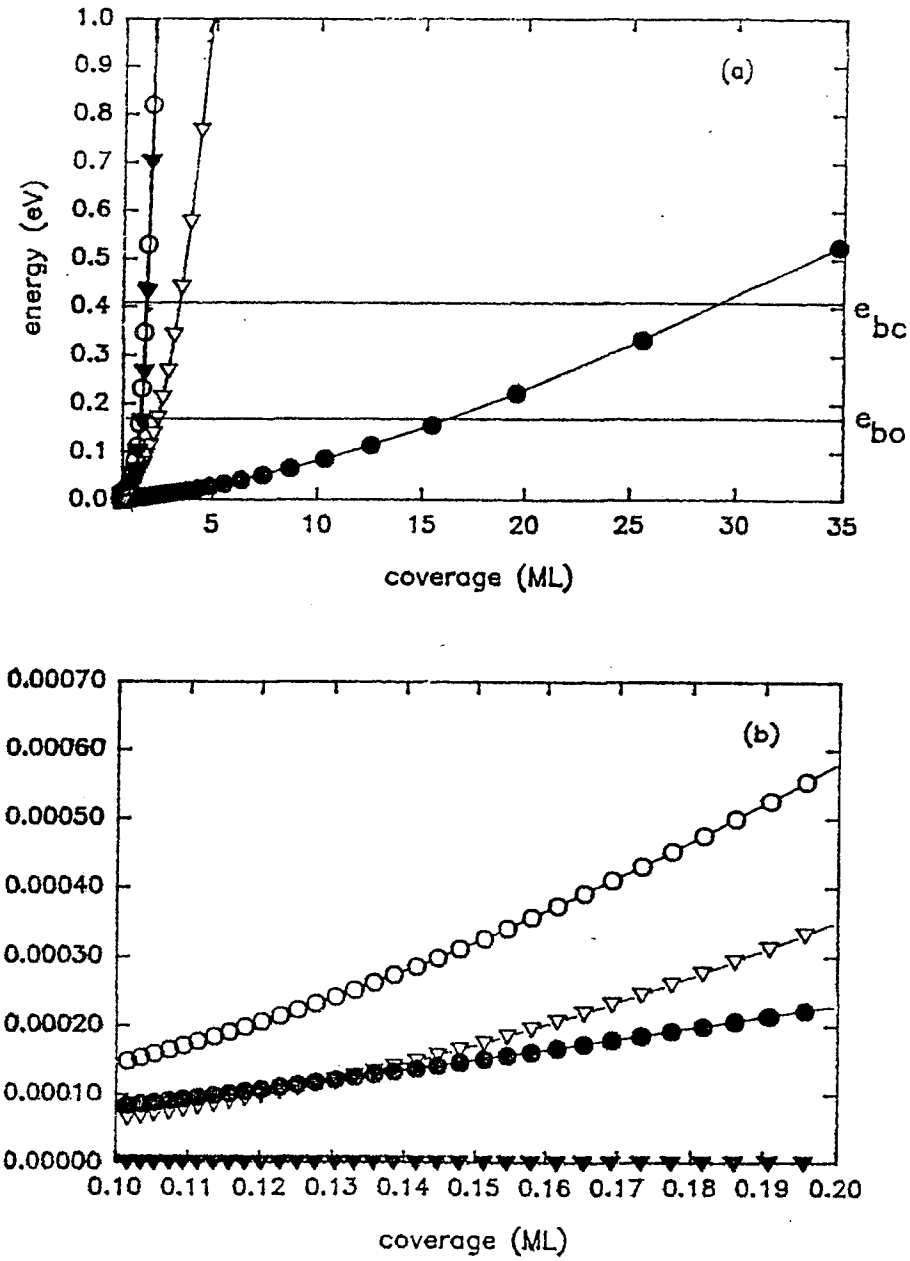

FIG. II.8. (a) Plot of interaction energies versus coverage for a lattice of CO molecules adsorbed all O-down on NaCl in the range where the interaction energies [U_{tot} (O), U_{dipole} (●), U_{quad} (▽), and U_{disp} (▾)] become comparable to the binding energy. The horizontal lines indicate the binding energies of a C-down (e_{bc}) and an O-down (e_{bo}) molecule adsorbed vertically above a metal ion site. (b) Plot of the interaction energies [U_{tot} (O), U_{dipole} (●), U_{quad} (▽), and U_{disp} (▾)] in the coverage range where they become comparable to each other.

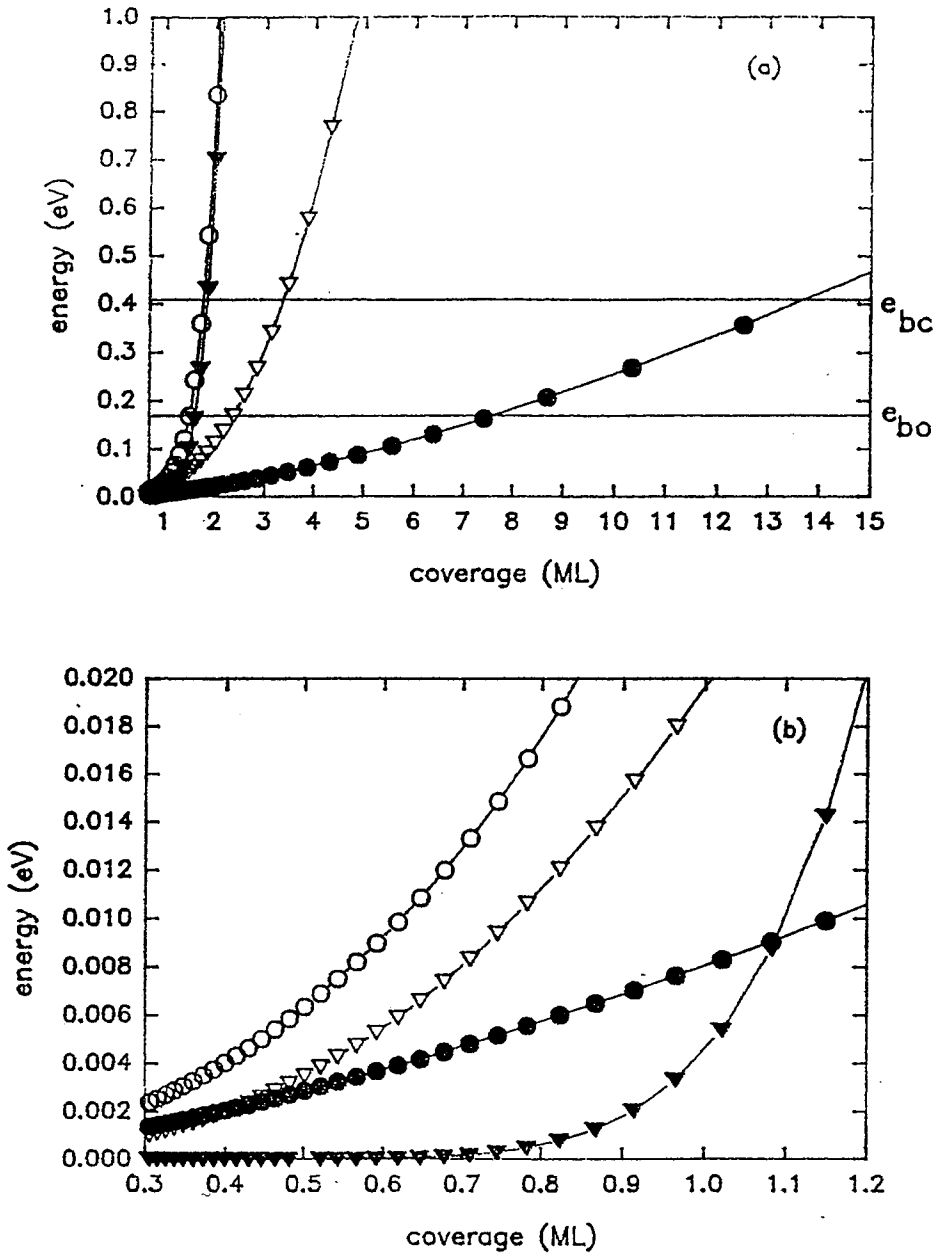

FIG. II.9. (a) Plot of interaction energies versus coverage for a lattice of CO molecules adsorbed alternating C-down and O-down on NaCl in the range where the interaction energies [U_{tot} (O), U_{dipole} (●), U_{quad} (▽), and U_{disp} (▾)] become comparable to the binding energy. The horizontal lines indicate the binding energies of a C-down (e_{bc}) and an O-down (e_{bo}) molecule adsorbed vertically above a metal ion site. (b) Plot of the interaction energies [U_{tot} (O), U_{dipole} (●), U_{quad} (▽), and U_{disp} (▾)] in the coverage range where they become comparable to each other.

the highest coverage commensurate structure energetically allowed is that with $\theta = 0.5$ ($\sqrt{2} \times \sqrt{2}$ commensurate structure).

The dipole interaction for CO on MgO for the C-down ferroelectric lattice, U_{cF}, is greater than U_{quad} for $\theta < 0.85$ [Fig. II.4(b)], U_{oF} is greater than U_{quad} for $\theta < 0.50$ [Fig. II.5(b)], and U_{AF} is greater than U_{quad} for $\theta < 0.73$ [Fig. II.6(b)]. Dipole interactions dominate for all coverages less than $\theta \approx 0.5$ ML. Also, U_{disp} becomes greater than U_{cF} at $\theta = 0.75$ [Fig. II.4(b)], greater than U_{oF} at $\theta = 0.69$ [Fig. II.5(b)], and greater than U_{AF} at $\theta = 0.73$ [Fig. II.6(b)]. Therefore, we conclude that our model is applicable to fully occupied, square-symmetry, commensurate CO monolayer superlattice structures on MgO (100) where $\theta \leq 0.5$ ML and where admolecules sit vertically above cations.

Similar conclusions are drawn for CO adsorbed on NaCl. The dispersion energy, U_{disp}, becomes greater than the O-down binding energy at $\theta = 1.59$ ML and greater than the C-down binding energy at $\theta = 1.78$ [see Fig. II.7(a), II.8(a), or II.9(a)]. This implies that for CO on NaCl, the highest coverage commensurate structures are energetically allowed; i.e., we can consider lattices up to $\theta = 1$ (1 x 1 commensurate structure). The dipole interaction for the C-down ferroelectric lattice, U_{cF}, is greater than U_{quad} for $\theta < 0.66$ [Fig. II.7(b)], U_{oF} is greater than U_{quad} for $\theta < 0.13$ [Fig. II.8(b)], and U_{AF} is greater than U_{quad} for $\theta < 0.41$ [Fig. II.9(b)]. Also, U_{disp} becomes greater than U_{cF} at $\theta = 1.18$ [Fig. II.7(b)], greater than U_{oF} at $\theta = 1.31$ [Fig. II.8(b)], and greater than U_{AF} at $\theta = 1.09$ [Fig. II.9(b)].

We conclude that our model is applicable to all fully occupied, square-symmetric, commensurate CO monolayer superlattice structures on NaCl(100) where admolecules sit above cations, although some tilting of the CO molecules due to quadrupole interactions may occur for coverages above 0.13 ML. However, theoretical studies[31,48] calculating the binding energy of CO on NaCl for different orientations above the cation have shown the perpendicular orientation to be by far the most energetically favored. Note that the binding energies (Table II.1) are one to two orders of magnitude larger than interaction energies (Table II.3). Therefore, we conclude that any small increase in interaction energy due to CO tilting would be offset by a decrease in the binding energy, and that the molecules will not tilt significantly. For the CO and NaCl system, perpendicular adsorption has been observed,[46,47] which is consistent with our analysis.

We also calculated the energies for specific lattices corresponding to fully occupied square-symmetric superlattices prescribed by adsorption above cation sites. These results are summarized and tabulated in Table II.3. We use these values to determine the interaction constants (J, K, L, H, and Δ) used in the Ising model calculations of the possible phase transitions, according to Eq. (II.10). The values of J, K, and L are plotted versus coverage, for MgO in Fig. II.10(a) and for NaCl in Fig. II.10(b). For CO on MgO, H = 59 meV, and Δ = 331 meV, for the upper limit. For the lower limit, at θ = 0.5 ML, H = 18 meV, and Δ = 161 meV. For all other coverages, H = 5 meV, and Δ = 189 meV. For CO on NaCl,

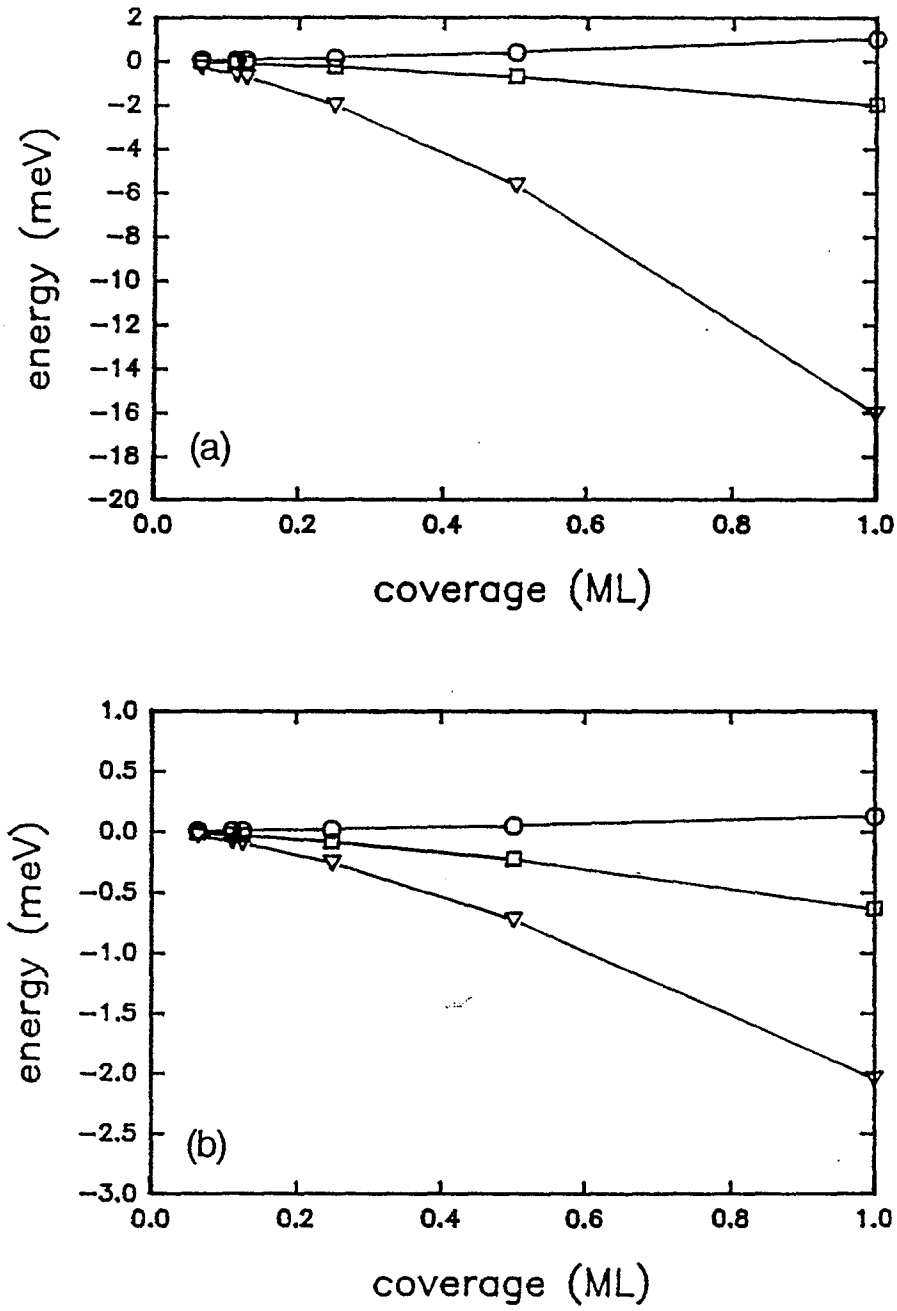

FIG. II.10. Interaction parameters [J (O), K (v), and L (□)] for (a) CO on MgO and (b) CO on NaCl.

H = 123 meV, and Δ = 294 meV.

4. Analysis of Spin-1 model

We now are ready to determine the spin ordering as a function of temperature. The coverage, Θ, is treated as a parameter, and Eq. (II.7) is solved for M as a function of T for fixed Θ. This effectively changes the ensemble we consider from the grand canonical ensemble to the canonical ensemble by fixing the number of particles adsorbed to the lattice. The chemical potential in Eq. (II.10) reduces formally to the orientation-dependent binding energies, ϵ_{bo} and ϵ_{bc}. By solving this equation for M as a function of temperature at a variety of coverages, we determine the thermodynamics and phase transitions of this system. J and L contain the information about the CO-CO interactions, and H contains the information about the CO-substrate interactions. For CO on MgO and NaCl, the magnitudes of the binding energy asymmetries are much greater than the adsorbate-adsorbate interaction energies. This implies that our systems are analogous to a magnetic system in a strong applied field. Therefore, there will still be a residual magnetization, or net dipole orientation, even at very high temperatures, and no abrupt phase transition.

5. Observable changes in dipole orientation

In order to consistently interpret our results, we define an observable change in dipole orientation as $|M| \geq 0.5$. This

corresponds to 75% of the CO molecules in one orientation and 25% in the other. Pacchioni *et al.* have calculated ir spectral shifts separated by 52 cm^{-1} (6.5 meV) for the two vertical orientations of CO adsorbed on MgO;[32] Dovesi *et al.* estimate this separation to be $\approx$ 20 cm^{-1}.[52] Given such large separations one expects small changes in M would be observable with standard ir spectroscopy. This may not be strictly true as dipole coupling interactions could affect the relative ir peak intensities or suppress the ir signal entirely for one or both orientations near $|M| \approx 0.5$.[60] Photoemission spectroscopy of adsorbed C or O core levels may provide an alternate method to monitor M; however, these may be difficult measurements due to the high energy resolution required. The contrast of C and O atoms for x-ray, or electron diffraction is not sufficient to readily distinguish the two vertical orientations of CO. Neutron diffraction may be a viable probe if one chooses to use CO with C and O isotopes which maximize the difference in neutron scattering cross section. In this way, it may be possible to distinguish neutron signals from different orientational configurations.

6. *Phase transitions for CO on MgO and CO on NaCl*

The results of the mean field approximation analysis for the spin-1 Ising model of CO on NaCl are shown in Fig. II.11(a). We find that the low temperature configuration is an ordered ferroelectric state with all molecules adsorbed C-down. The observable change in dipole orientation takes place at T $\approx$ 2500 K, well above both the

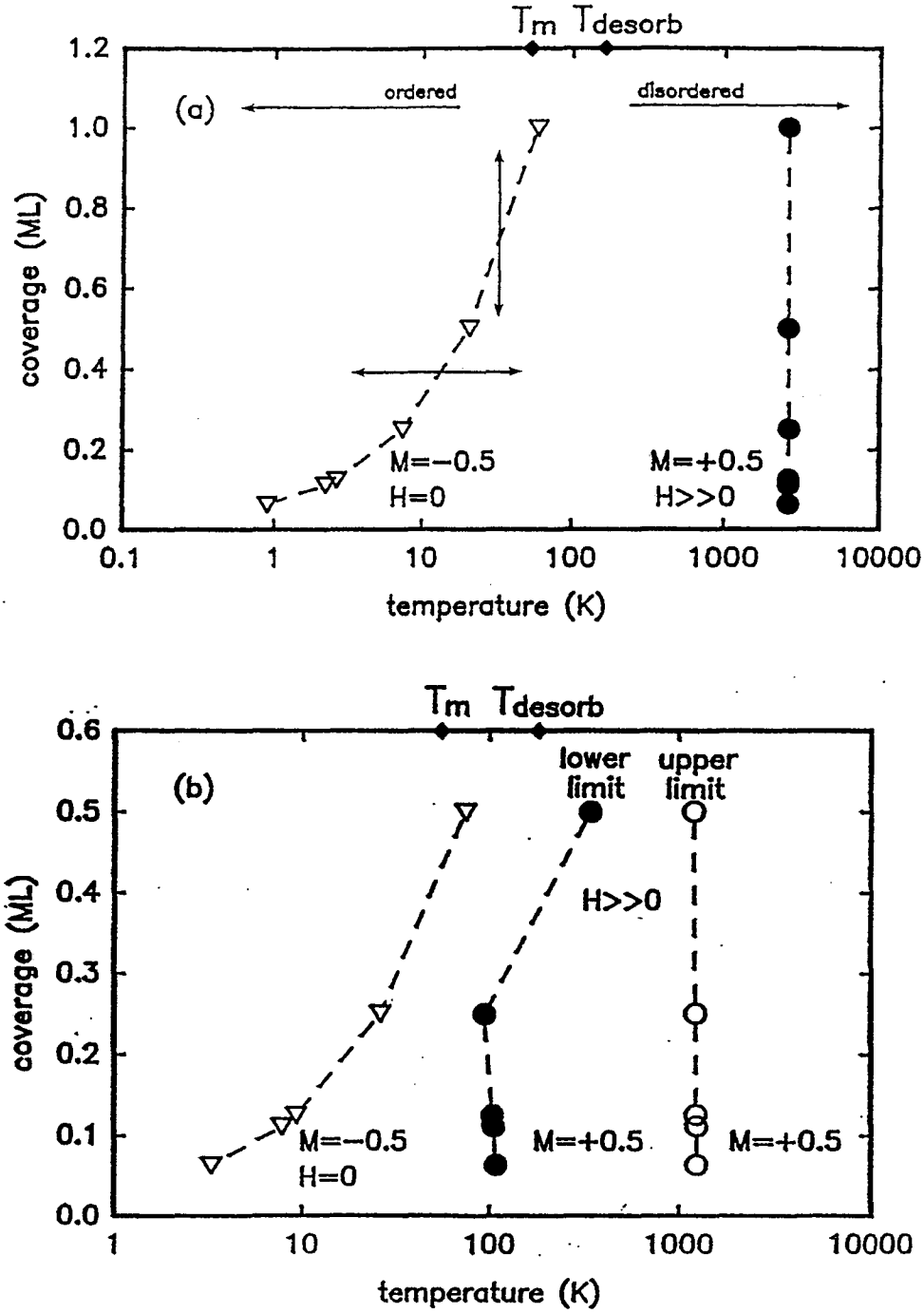

FIG. II.11. Phase transitions for CO on ionic crystals (a) CO on NaCl (100); (b) CO on MgO (100). Note the logarithmic temperature scale. T_m and T_{desorb} indicate the completed monolayer melting temperature and approximate film desorption temperature, respectively.

desorption temperature (T_{desorb} = 163 K)[31] and the 2D melting temperature (T_m = 53 K).[47] This clearly will not be observable.

Because of the large uncertainties in calculations of the difference of C-down and O-down binding energies, we also considered the limiting case where the binding energy is equal for both vertical orientations of the dipole, or equivalently the binding energies become negligible (i.e., H goes to 0). Here the low temperature configuration is ordered ferroelectric with all molecules adsorbed O-down ($M > -0.5$) and the high temperature configuration is disordered ($|M| < 0.5$). This observable change in dipole orientation at $\theta = 0.50$ ML is indicated by a horizontal arrow in Fig. II.11(a). The observable orientation change occurs at temperatures from 0.1 K at the lowest coverage ($\theta = 0.063$) to 60 K at the highest ($\theta = 0.50$), increasing with increasing coverage. These temperatures are below (approximately) T_m and much lower than T_{desorb}. The temperature dependence of the observable orientation change for constant coverage suggests that, if the difference in binding energy for both vertical orientations is small or vanishing, a coverage-dependent disordered-to-ordered ferroelectric orientation change may also occur [illustrated by a vertical arrow at constant T = 30 K in Fig. II.11(a)]. This would happen if CO adsorbs in random orientation at low coverage where interaction energies are small. Then, as the coverage increased, and the dipole interactions became more important, the dipole-dipole interactions could drive a phase transition to an ordered ferroelectric state.

Similar results for CO on MgO are presented in Fig. II.11(b). The upper limit of the difference in binding energy (see Table II.1) is shown as open circles; the lower limit is shown as closed circles. The low temperature configuration is a ferroelectric state with all C-down. The ordered ferroelectric-to-disordered orientational phase change temperature is approximately 1200 K for the upper limit of the difference in binding energies, and ranges from 350 K to 100 K for the lower limit. These temperature are well above the 2D melting temperature (T_m = 55 K)[61] and are above the desorption temperature (T_{desorb} = 180 K)[61] except for the lower binding energy cases where $\theta \leq$ 0.25 ML. Again, this transition is probably not observable. For the limiting case where H approaches zero, the low temperature configuration is a ferroelectric state with all molecules adsorbed O-down. The observable orientation change occurs at temperatures from 1 K to 44 K, increasing with increasing coverage. Again, these temperatures are less than or approximately T_m and much less than T_{desorb}, suggesting a coverage dependent disordered-to-ordered ferroelectric transition may also be observable for this limiting case.

E. Discussion of results: Comparison with experiment

There is very limited direct information on the structure or phase transitions of CO on MgO or NaCl which can be compared with our theoretical predictions. There is no direct evidence for ordered dipole phases or phase transitions for either system. Our results

suggest the asymmetric CO–substrate interactions will primarily determine the orientation of the admolecules. The observed ir spectral shift[61] for CO on MgO is consistent with the spectral shift calculated for the C–down orientation.[32] This would corroborate theoretical models which predict a stronger binding energy for the C–down orientation as the driving mechanism of the thermodynamics of submonolayer CO on MgO.

Recent studies of CO on NaCl using He diffraction,[47] at a coverage of $\theta = 1$ ML, for a temperature range of $30\ K < T < 53\ K$, found the CO structure is commensurate with the NaCl (100) surface. At $T < 30$ K, experimenters observed a doubling of the unit cell. This would be consistent with alternately tilted CO molecules or with antiferroelectrically ordered CO molecules. This tilting, however, has not been observed in ir polarization studies,[62] nor is there evidence of an antiferroeletric state. Further study is needed to clarify the discrepancy between the He diffraction and ir data.

The He diffraction studies at a coverage of $\theta = 1$ ML for CO on NaCl and LEED studies at $\theta > 0.5$ ML (see Sec. D.1) for CO on MgO suggest that the quadrupole interactions may influence the orientation of the CO molecules at these higher coverages. Lower coverage structural studies of these two systems seem warranted, to determine first if low-density square, commensurate superlattices exist, and to determine at what coverages the quadrupole interactions begin to affect the orientation of the CO admolecules. Also, studies to clarify whether tilting of the molecules occurs in the CO on NaCl

monolayer at low T should be undertaken. Such studies would be useful in quantifying the binding energies and molecular interaction energies determined by modeling studies and further address the applicability of our model.

Alternative phase transitions may occur or existing phase transitions may be shifted to experimentally observable temperatures as the relative strengths of the substrate-adsorbate [H in Eq. (II.7)] and adsorbate-adsorbate interactions (J and L) are varied. In the CO on NaCl and MgO, the binding energies for the two orientations are relatively large and differ greatly ($H \gg 0$), while the interaction energies are relatively small (J and L are small). For example, the disordered-to-ordered ferroelectric or antiferroelectric transitions could be moved to lower temperatures by decreasing the ratio H/zJ [see Eq. (II.7)]. This could be done by lowering the binding energies (e.g., by plating the substrate with a rare gas), or by increasing the interaction energies. This may be achieved if the substrate electric field is reduced (lowering p_{ind}) by choosing a different substrate, by investigating the second or higher adsorbed layer, or by studying substrates plated with a relatively inert buffer layer such as Ar or Xe. If a monolayer of Xe is used to pre-plate MgO or NaCl, a 30% reduction in the substrate interaction energy would occur (assuming the binding energy falls off exponentially).[48] This would mitigate dipole induction effects significantly, and reduce the binding energies for CO adsorption.

F. Other ordering mechanisms

CO adsorbs to graphite in a herringbone structure, primarily determined by the strong quadrupole interactions between the CO molecules (see Chap. I. Sec. B.4).[63] CO on graphite exhibits an additional low temperature end-to-end ordering phase transition that was originally attributed to dipole ordering.[64] Subsequent study has determined that steric (or shape asymmetry) interactions are responsible for this ordering.[13,14] In the herringbone arrangement, the CO molecules lie parallel to the plane of the graphite substrate, with their molecular axes almost perpendicular (between 80° and 90°).[12,63,65] In this configuration, electric dipole interactions are almost zero; indeed, classically, for perpendicular orientation, they are zero. Therefore, steric interactions can cause CO end-to-end ordering on graphite at low temperature.

We are interested in determining whether steric interactions can stabilize an antiferromagnetic low temperature state for CO on ionic crystals. For this to be true, the difference in the steric interaction energy for two aligned versus two antialigned molecules should be comparable or greater than the difference in CO binding energy for the two orientations. van der Pol *et al.* have calculated the interaction energy for a CO dimer (i.e., a pair of free CO molecules) as a function of orientation and distance.[66] From their calculations, we can estimate the maximum value of steric interaction energy for two interacting CO molecules. We take the final interaction potential calculated by van der Pol *et al.*, and remove

contributions from the electrostatic and dispersion interactions.[66] We consider only nearest neighbor interactions. The values of the interaction potential for the different dipole pairs are tabulated in Table II.4. To emphasize, these are maximum values of the steric interaction. We do not consider any higher multipoles than the quadrupole, while van der Pol *et al.* consider up to the 32-pole contribution.[66]

The steric interaction energies are compared to the dipole interaction energies and binding energies for CO on MgO and NaCl (Table II.4). For CO on MgO, the steric interaction energies are comparable to the dipole interaction energies for the electrostatic and dispersion interactions (see Table II.4), and are an order of magnitude less than the binding energies (see Table II.4). For CO on NaCl, steric interactions are again of the same order as the dipole interactions (see Table II.4), and are about ten times less than the binding energies. From these comparisons, we conclude that steric interaction may cause an antiferroelectric state to be slightly more favored, and cause the order-disorder transition temperature to be lower for the highest density case. However, it will not significantly alter the results of our study. This is in contrast to the CO on graphite system, where binding asymmetries do not exist, and steric interactions can then stabilize an electrically ordered state.[13,14] Indeed, the lowest potential energy configuration for a free CO dimer is perpendicular, according to van der Pol *et al.*[66]

TABLE II.4. Comparison of steric interactions to electrostatic interactions for CO on NaCl and MgO. θ is the CO coverage, and r is the corresponding CO separation. U_{stp} is the steric interaction between two parallel CO molecules, U_{sta} is the steric interaction between two antiparallel CO molecules, ΔU_{st} is the difference in steric interactions for the two orientations, ΔU_{di} is the difference in the dipole energy, and ΔU_{bi} is the difference in the binding energy [see Table II.2].

	θ (ML)	r (Å)	U_{stp} (meV)	U_{sta} (meV)	ΔU_{st} (meV)	ΔU_{di} (meV)	ΔU_{bi} (meV)
CO/ NaCl	1	3.99	-19.6	-21.9	1.54	10.2	246
CO/ MgO	0.5	4.12	-12.0	-13.6	2.29	11.3	36-117

G. Other physisorbed dipolar systems

Our simple spin model can be applied to other dipolar systems to test its generality and to look for different phases and transitions. An antiferroelectric state in a physisorbed system requires $p_{ind} < p_{nat}$ so that the two vertical orientations have opposed net dipoles, and alternating alignment is energetically favored. Two ways to realize such a system would be to adsorb molecules with a smaller polarizability, and hence a smaller induced dipole moment, or to adsorb molecules with a larger natural dipole moment. Of particular interest are molecules of the form CX_nY_{4-n}, where X,Y = H, F, Cl, Br, or I and n = 1, 2, 3, or 4 (see Fig. II.12). These exhibit a large natural dipole moment and small polarizability compared to CO (see Table II.5).[67] The adsorption of these molecules on graphite has been studied extensively. Antiferroelectrically ordered phases have been observed for CF_3H[17] and for CH_3Cl and CH_3Br[16] on graphite. Other electrically ordered phases have been observed for CF_3Cl on graphite.[18] For graphite coated with Xe, CH_3F is observed to have a ferroelectric phase not seen on bare graphite.[16] However, none of these adsorption systems on graphite has simple cubic symmetry because of the hexagonal symmetry of the graphite substrate. Thus, they do not lend themselves easily to application to our simple model. In principle, such dipolar adsorption on graphite could be modeled by an Ising model on a triangular lattice.

We consider the adsorption of the halogenated methanes on square symmetric substrates such as MgO or NaCl using the spin model we have

developed.[68] We focus on molecules of the form CH_3Y (see Fig. II.12), which have large dipole moments and small polarizabilities due to the large electronegativity of the halogens. Very few experimental studies of these system have been undertaken, and hence determination of the parameters for use in the application of a spin lattice model is difficult. However, we make educated guesses at the order of magnitude of the interaction energies to determine if interesting physics occurs.

Consider, for example, CH_3F. This halogenated methane has a much higher dipole moment than CO, and relatively low polarizability.[16,67] Studies of this molecule adsorbed to NaCl using ir determine the binding energy to be 0.259 eV, comparable to the binding energies of CO to NaCl and MgO.[69] In order to continue, two assumptions are made here. First, it is assumed that binding takes place over cation lattice sites. While this has not been experimentally determined for halogenated methanes, theoretical studies of methane on NaCl have determined methane to adsorb over cation lattice sites.[70] It then seems plausible to assume the same adsorption site for halogenated methanes. It is also assumed that adsorption occurs with the dipole moment perpendicular to the surface. While this assumption has no basis in the literature, it seems reasonable, since this configuration would minimize the interaction between the strong dipole moment of the adsorbate and the electric field of the substrate. Given these two assumptions, the Ising model can be applied to determine whether electrically order phases will

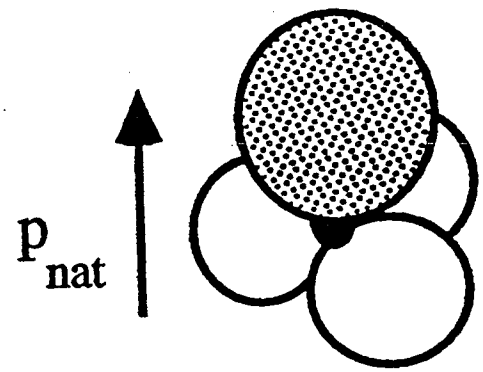

FIG. II.12. Schematic of a halogenated methane molecule. The shaded circle is the halogen molecule.

TABLE II.5. Physical parameters for the halogenated methanes on NaCl. The estimated values are marked with an asterisk.

	natural dipole mom. (D)	polariz-ability (Å^3)	Lennard-Jones parameters		binding energy (meV)	binding asymmetry		p_{ind}		p_{tot}	
			ε_{LJ} (K)	σ_{LJ} (Å)		ε_u (meV)	ε_d (meV)	up (D)	down (D)	up (D)	down (D)
CH_3F	1.855[a]	2.61[a]	279[c]	3.77[c]	259[d]	290*	228*	0.361*	-0.361*	2.216*	-1.494*
CH_3Cl	1.880[b]	4.55[a]	355[c]	4.11[c]	259*	313*	204*	0.629*	-0.629*	2.509*	-1.251*
CH_3Br	1.800[a]	5.59[a]	355*	4.11*	259*	326*	192*	0.773*	-0.773*	2.573*	-1.107*
CH_3I	1.62[b]	5.59*	355*	4.11*	259*	334*	184*	0.870*	-0.870*	2.490*	-1.010*

* estimated

[a] Ref. 16
[b] Ref. 67
[c] Ref. 71
[d] Ref. 69

occur. We make the same asumptions for the other halogenated methanes.

An induced dipole moment for CH_3F is calculated by ratioing the induced dipole moment of CO divided by its polarizability to that of CH_3F. This is equivalent to assuming that the substrate electric field experienced by the adsorbate is independent of the adsorbate. Again, this is not strictly true (induction effects and polarization of the surface will alter the field); however, to first approximation, this is valid. The calculated induced dipole moment of CH_3F is 0.233 D. Then the total dipole moment for the dipole down orientation is -1.62 D, and the dipole moment for the dipole up configuration is 2.09 D. The two dipole moments have different signs, which allows the possiblity of antiferroelectrically ordered phases. Similar results are found for the other halogenated methanes (see Table II.5).

Given these dipole moments, we calculate the interaction energy for a lattice of CH_3F adsorbed on NaCl in the three special configurations: all dipoles up (U_{uu}), all dipoles down (U_{dd}), and an antiferroelectric configuration (U_{ud}). To calculate the dispersion, we use the Lennard-Jones potential. It has the following form:

$$U_{ij}=4\epsilon\left(\left(\frac{\sigma}{r}\right)^{12}-\left(\frac{\sigma}{r}\right)^{6}\right), \qquad \text{(II.18)}$$

where ϵ and σ are interaction parameters (unique to a molecule) that determine the value of the interaction, and r in the molecule separation. The Lennard-Jones parameters (Table II.5) have been calculated for CH_3F and CH_3Cl.[71] We estimate the parameters for CH_3Br

and CH_3I to be similar to CH_3Cl. This probably underestimates the repulsive term, as CH_3Br and CH_3I are slightly larger the CH_3Cl. It also probably underestimates the attractive energy as CH_3Br has a larger polarizability then CH_3Cl. However, we are primarily interested in determining whether dipole interactions are comparable to binding interactions, and hence sufficient to drive an antiferromagnetic state. The dispersion is, to first order, independent of orientation.

Because the total dipole moments for the halogenated methanes adsorbed on NaCl have different signs, depending on orientation, we have the possibility of AFE ordered states. In this case, we use $\mathcal{H}_{AFE}$ [Eq. (II.4)] to describe the system. As in the FE case, we relate the interaction constants (J, K, and L) to the expectation value of the interaction part of the Hamiltonian. $\langle\mathcal{H}_{AFE}\rangle$ is equated to the calculated interaction energies U_{int} for the three special configurations: all dipoles on both sublattices up ($M_u = M_d = +1$), all dipoles down ($M_u = M_d = -1$), and the AFE state ($M_u = +1$, $M_d = -1$). That is, for $\Theta_u = \Theta_d = +1$:

$$U_{int}(M) = \begin{cases} -z\,(J + 2L + K) = -zJ_{uu} & ;\ M_u = M_d = +1 \\ -z\,(K - J) = -zJ_{ud} & ;\ M_u = +1,\ M_d = -1 \\ -z\,(J - 2L + K) = -zJ_{dd} & ;\ M_u = M_d = -1. \end{cases} \quad \text{(II.19)}$$

This is slightly different than the FE case. In the AFE case, the M=0 is uniquely determined to be the $M_u = +1$, $M_d = -1$ state, so that the interaction energy for the M=0 case has only one contribution, that from the interaction between up and down dipoles. In the FE case, the

M=0 state is not unique, and can be any random distribution of up and down dipoles so that the interaction energy for the M=0 state has contributions from all dipole configurations (see Sec. D.1).

Figures II.13–II.16 are plots of the interaction energies, U_{uu}, U_{dd}, and U_{ud}, and the binding energies ϵ_u and ϵ_d as a function of coverage for the halogenated methanes. For CH_3F (Fig. II.13), we see that for $\theta = 1$ the interaction energies are comparable to the binding energies. U_{ud} is negative, implying that the AFE state is energetically favorable. U_{uu} is greater than the binding energy, and hence will not be observed. As the coverage is decreased, the interaction energies become small compared to the binding energies. Very similar trends are observed for CH_3Cl, CH_3Br, and CH_3I (Fig. II.14–II.16).

We now calculate J, K, L, H, and Δ (the interaction parameters), for each halogenated methane at the same superlattice coverages as presented above. These results are presented in Figs. II.17–II.20. Note that J is negative for all adsorbates.

We make preliminary calculations of the phase diagram for CH_3F adsorbed on NaCl, by parametrically solving Eqs. II.9 (a) and (b) for M_u and M_d as a function of T for fixed θ.[68] In this system, we observe a low temperature, low coverage ($\theta \leq 0.25$) FE phase, with $M_u/\theta_u = M_d/\theta_d = +1$. This phase is driven by the binding asymmetry for up and down dipoles (up is energetically preferred). As the temperature is increased, M_u and M_d gradually tend to zero at low coverage. For $\theta \geq 0.5$, we observe a low temperature AFE phase ($M_u/\theta_u = +1$, $M_d/\theta_d = -1$).

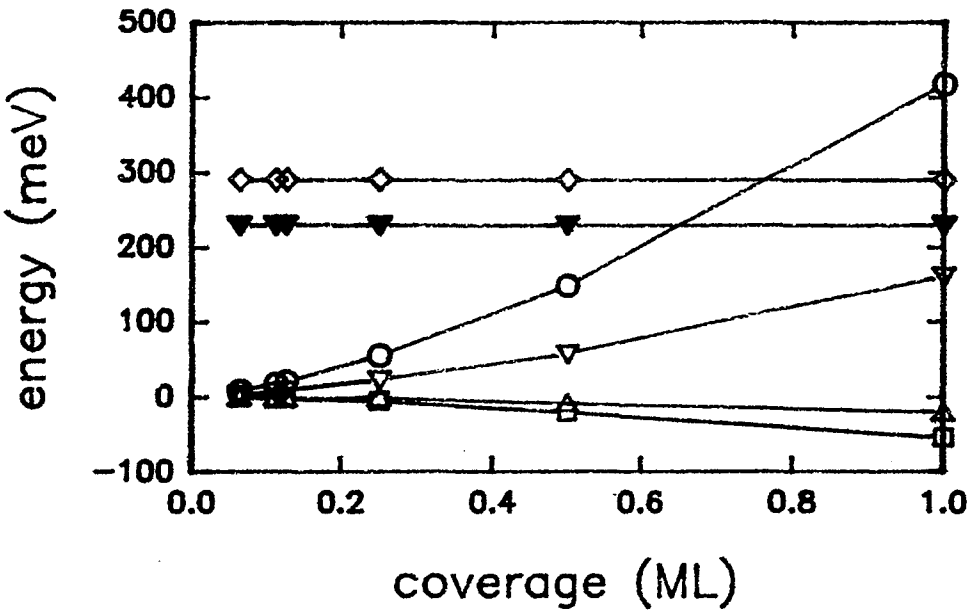

FIG. II.13. Interaction energies [U_{uu} (O), U_{dd} (▽), U_{ud} (□), U_{LJ} (△), ϵ_u (◇), and ϵ_d (▼)] for CH_3F.

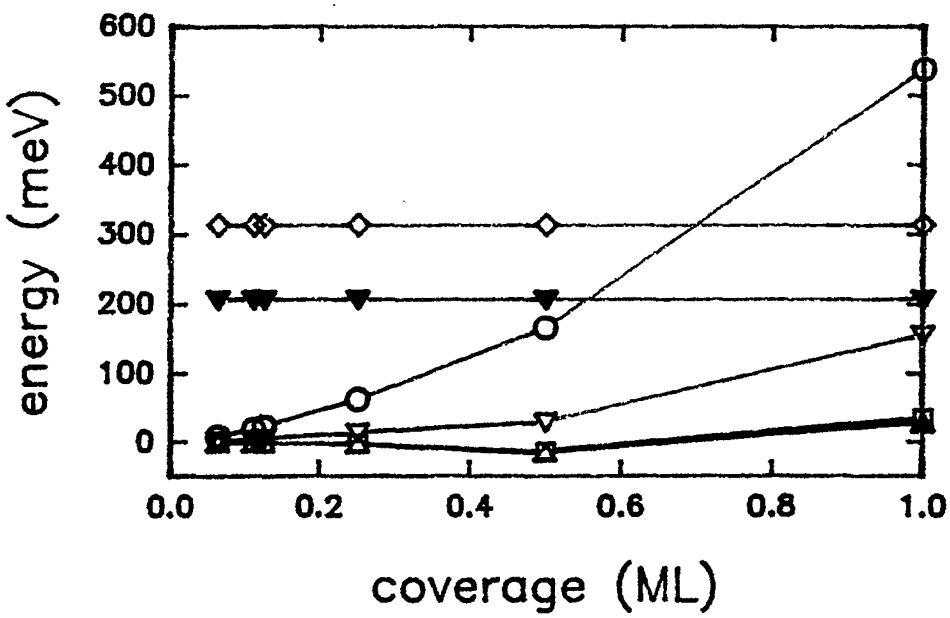

FIG. II.14. Interaction energies [U_{uu} (O), U_{dd} (∇), U_{ud} ($\square$), U_{LJ} (Δ), ϵ_u ($\diamond$), and ϵ_d ($\blacktriangledown$)] for CH_3Cl.

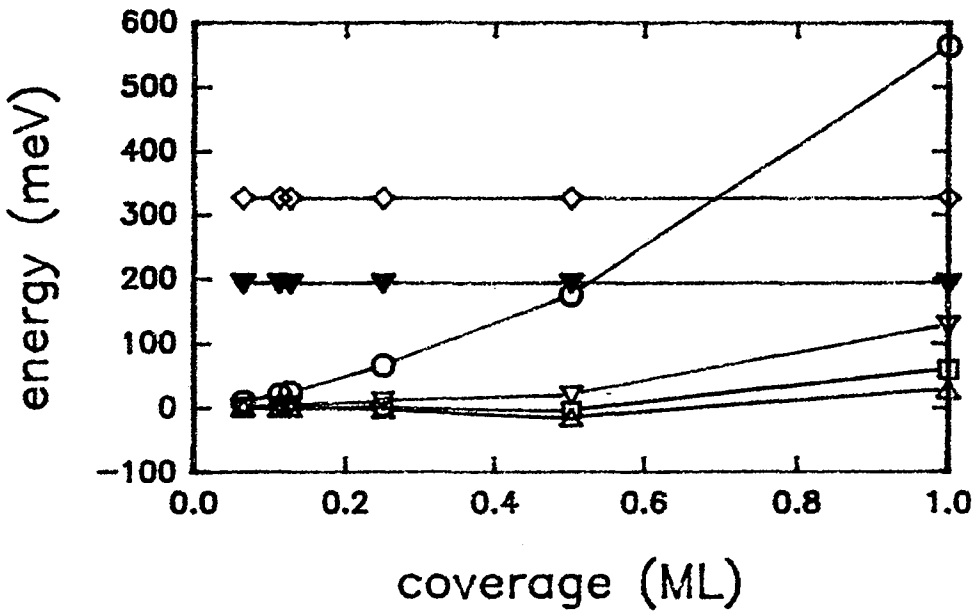

FIG. II.15. Interaction energies [U_{uu} (0), U_{dd} (▽), U_{ud} (□), U_{LJ} (△), ϵ_u (◇), and ϵ_d (▾)] for CH_3Br.

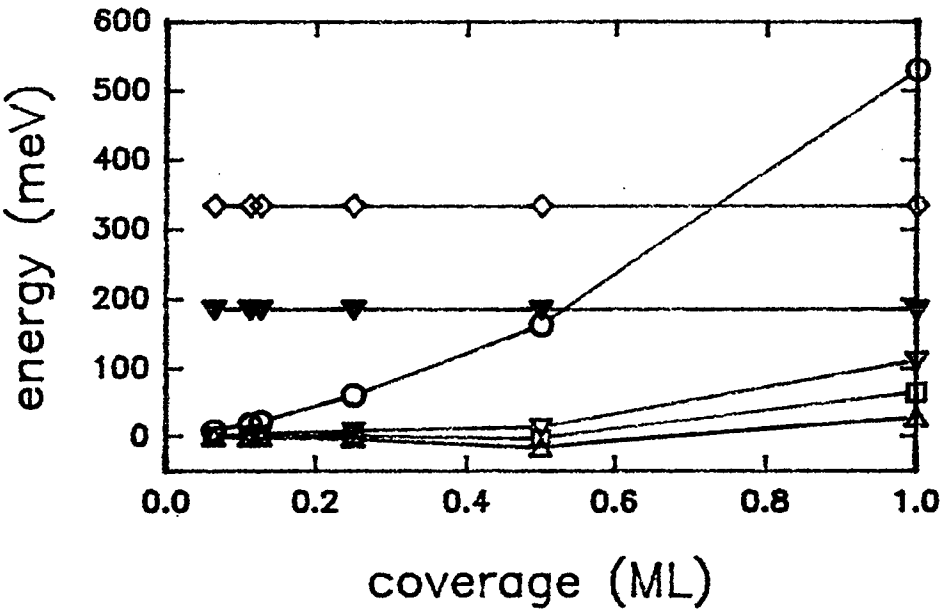

FIG. II.16. Interaction energies [U_{uu} (O), U_{dd} (∇), U_{ud} ($\square$), U_{LJ} ($\triangle$), ϵ_u ($\diamond$), and ϵ_d ($\blacktriangledown$)] for CH_3I.

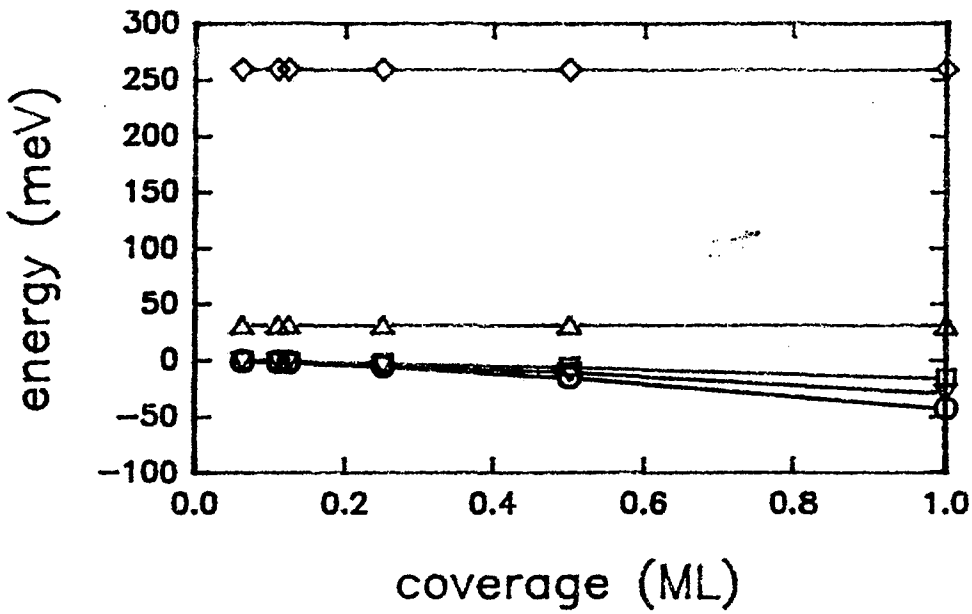

FIG. II.17. Interaction parameters [J (O), K (▽), L (□), H (△), and Δ (◇)] for CH_3F.

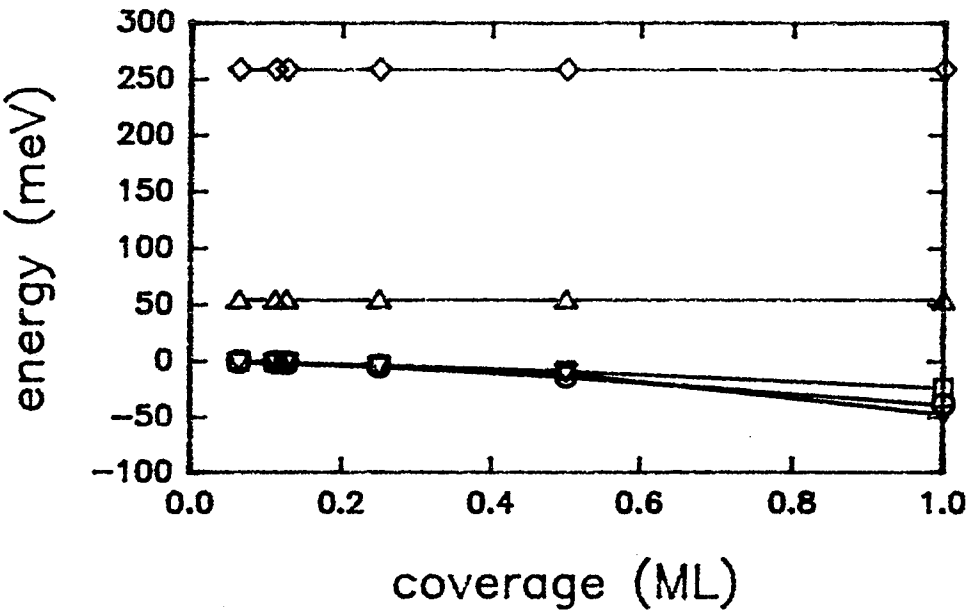

FIG. II.18. Interaction parameters [J (0), K (▽), L (□), H (△), and Δ (◇)] for CH_3Cl.

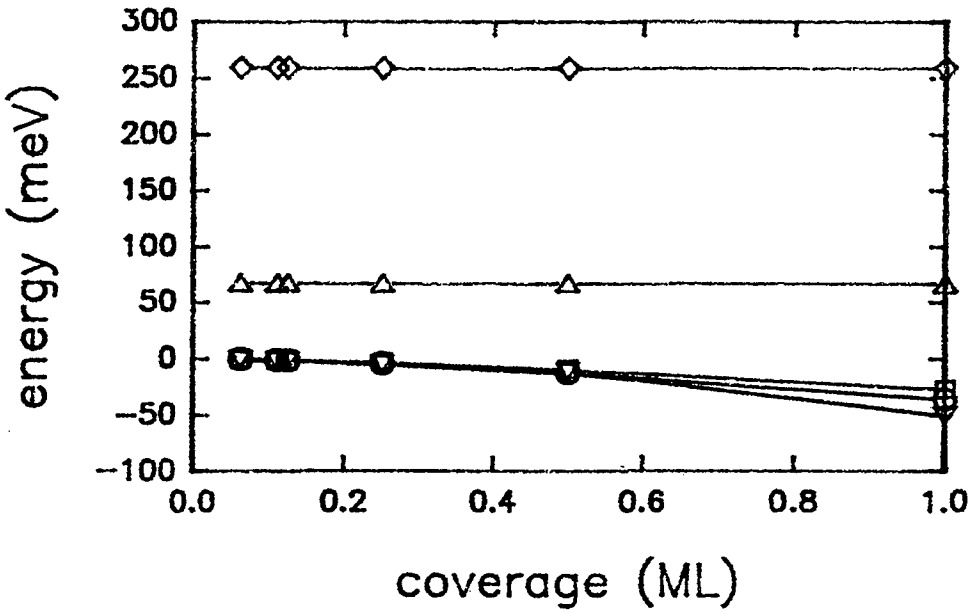

FIG. II.19. Interaction parameters [J (O), K (▽), L (□), H (△), and Δ (◇)] for CH_3Br.

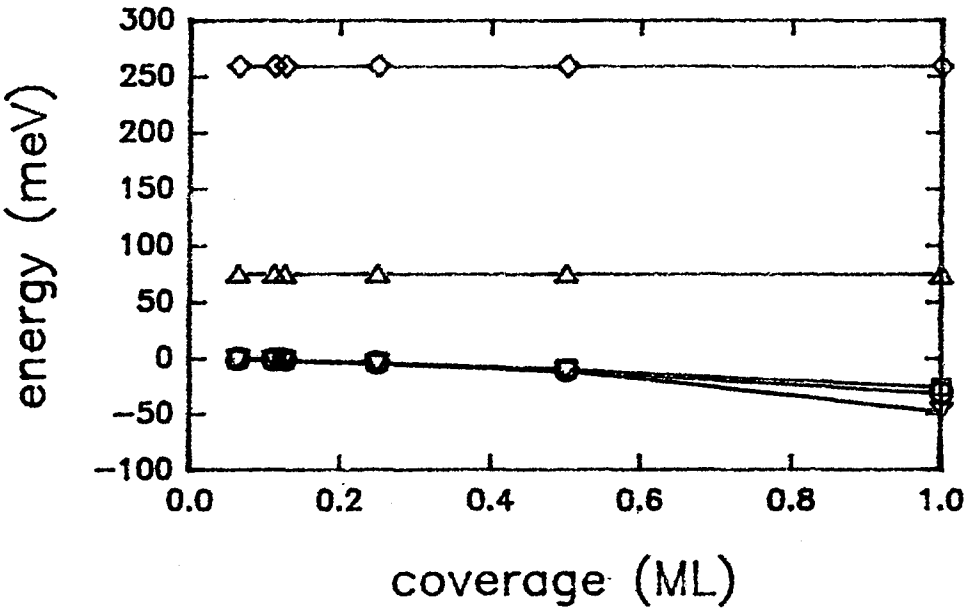

FIG. II.20. Interaction parameters [J (O), K (▽), L (□), H (△), and Δ (◇)] for CH_3I.

The interaction parameters are greatest at these high coverages, and are comparable to the difference in binding energies (see Fig. II.17 and 18). The affinity for antialignment of the dipoles is sufficient at these high coverages to stabilize an AFE state. For $\theta = 1$ at about 2000 K, $M_u = M_d$ and an AFE → FE phase transition occurs; the AFE → FE state for $\theta = 0.5$ occurs at 360 K. These FE states gradually decay to disordered states.

We therefore observe two phase transitions for CH_3F on NaCl. A low temperature FE → AFE phase transition occurs which is driven by increasing coverage for all $T < 2000$ K. This phase transition should be experimentally accessible. An AFE → FE phase transition at high coverage and temperature occurs between T =360 K to T = 2000 K, very much higher than the desorption temperature (T=180 K),[69] and will not be observable.

We expect similar results for the other halogenated methanes on NaCl. The interaction parameters (J, K, L, Δ, and H) are studied in order to make general statements about the phase behavior of CH_3Cl, CH_3Br, and CH_3I. For all the halogenated methanes (CH_3F, CH_3Cl, CH_3Br, and CH_3I), we see the binding energy difference, Δ, increases from CH_3F to CH_3I (see Table II.5). We also see that J decreases, and K and L increases, from CH_3F to CH_3I (see Fig. II.17 - 20). We then expect then that for CH_3Cl, CH_3Br, and CH_3I the FE state favored by binding asymmetry is more favored the for CH_3F. We predict that for CH_3Cl, CH_3Br, and CH_3I, the AFE → FE phase transition will shift to lower T, and the FE → AFE phase transition will shift to higher θ.

This is promising; if the AFE → FE phase transition does shift to lower T, it may become experimentally accessible in CH_3Cl, CH_3Br, or CH_3I adsorbed on NaCl.

These antiferroelectrically ordered states should be readily distinguishable using x-ray diffraction from other ordered states because the halogen and hydrogen ends of the halogenated methane molecule have a large difference in scattering cross section. For example, in CH_3F, the fluorine is approximately 9 times a better scatterer than H_3. This is most dramatic in CH_3I, where iodine scatters roughly 3000 times more than hydrogen. [Note: These estimates are not strictly true; the atomic form factor may lower the scattered intensity of either end.] One should also be able to detect phase transitions with techniques such as neutron scattering (if one chooses neutron isotopes with high contrast in scattering lengths), atomic scattering (by observing a change in the adsorbate unit cell), and ir spectroscopy (by observing different vibrational frequencies for the molecule adsorbed dipole up or down).

H. Conclusions

In this chapter, we formulated adsorbed dipolar molecule systems as a spin-1 Ising model. This is a comprehensive model that allows quantitative prediction of the phases and phase transitions for specific systems. The appropriate modified BEG Hamiltonians were devloped for FE and AFE ordered systems. Mean field equations for the average spin and coverage for the ferroelectric case were verified.

Mean field equations for the average spin and coverage on each sublattice for the antiferroelectric case were found. We explored these Hamiltonians in the region of interaction parameter space appropriate to the adsorption studies, a region which had not been studied previously. These results are quite general, and applicable not only to our adsorption studies. These mean field equations can be used to study other general spin-1 systems described by Hamiltonians $\mathcal{H}_{FE}$ or $\mathcal{H}_{AFE}$ including other symmetric interactions for adsorbed systems. The results of this study can be used to identify ordering phases in any spin-1 system with analogous interaction parameters.

The ferroelectric Hamiltonian [Eq. (II.3)] was used to predict new dielectric phases for CO on MgO and NaCl. Phase diagrams for these systems have not previously been predicted. Here, we showed that the binding asymmetries determined a low temperature phase (for all coverages) which is ferroelectric with all CO molecules adsorbed C-down. At high temperature, the average spin approaches zero, as entropy effects begin to dominate. If we assume no binding asymmetry, we find a low temperature phase which is also FE, but which is determined by the lower interaction energy of a raft of CO molecules all adsorbed O-down. Again, at high T, entropy effects destroy this ordering. Our predictions are consistent with the limited experimetal data available.

The antiferroelectric Hamiltonian [Eq. (II.4)] was applied (in a preliminary manner) to halogenated methanes, specifically to CH_3F; again, new dielectric phases were determined and phase diagrams

predicted. In the case of halogenated methanes on NaCl, the dipole moment, and hence the interaction energy, of the halogenated methanes is much larger. Additionally, the total dipole moments for the two orientations have different signs. Our analysis predicts that CH_3F on NaCl exhibits a low temperature, low coverage FE phase, determined by the binding asymmetry. However, for $\theta \geq 0.5$, the low temperature phase is AFE, as determined by dipole-dipole interactions. The AFE phase becomes FE at very high temperature. This system exhibits two phase transitions, a low temperature FE → AFE with increasing coverage, and a AFE → FE phase transition at high coverage driven by temperature.

Indeed, in all of the systems studied, the interaction asymmetries determined 2D dielectric phases. Follow-up studies, both experimental and theoretical, are needed to determine phases driven by asymmetries in other systems. Preliminary studies of the halogenated methanes show that these systems hold particular promise. There has been very little experimental or theoretical work on these systems. It seems that studies of these systems are warranted, in order to determine whether our theoretically predicted phases and phase transitions exist.

CHAPTER III

STRUCTURE OF CO ON MgO

A. Introduction

As evidenced by the Ising model study presented Chapter II, the understanding of the phase transitions of CO on MgO (100) and NaCl (100) would be greatly aided by detailed knowledge of the structure. For example, our Ising calculations are based on the assumption that fully commensurate CO adlattices on MgO and NaCl exist. These have not been directly observed for CO on MgO; however, the only structural studies done were for a limited coverage ($\theta > 0.5$) and temperature range using LEED.[57] Structural studies using He diffraction of CO on NaCl have observed a fully commensurate adlattice exists for the highest coverage system;[47] however, again, only one coverage ($\theta = 1$) and a limited temperature range were studied. No other direct structural information for either system exists.

There are many outstanding questions which could be addressed by structural studies. For example, a study of CO on MgO in the submonolayer regime would determine whether CO forms a sequence of increasing density adsorbate superlattices or exhibits island growth (see Sec. II.D.2). Structural studies done in thermodynamic equilibrium (as opposed to quasi-equilibrium for dynamic LEED measurements) would allow correlation of the structure and thermodynamic variables and explore the 2D phase diagram for the system. Structural studies would enhance our understanding of the

relative importance of adsorbate-adsorbate and adsorbate-substrate interactions, and provide necessary data for numerical simulations.

Indeed, we attempted a structural study of CO on MgO. MgO smoke samples were prepared and characterized in our laboratory. Powder x-ray diffraction patterns of CO on MgO were measured at the National Synchrotron Light Source at Brookhaven National Laboratory. The objectives of this study were to determine the structure of CO adsorbed on MgO as a function of coverage, and to study the structure of the completed 2D monolayer from low temperature through melting. In this way, we hoped to address the outstanding questions regarding the growth mode in the submonolayer regime, and to determine the 2D phase diagram over a wide range of temperatures and coverages.

This chapter describes our attempts to measure the structure of CO on MgO. It begins by describing the experimental design (Sec. B). Sample preparation (Sec. C) and charaterization (Sec. D) are then detailed. The results of our x-ray measurements are presented in Sec. E, as is a discussion of the possible reasons our experiments did not yield any structural information.

B. Experimental design

Synchrotron x-ray diffraction of CO adsorbed on well-characterized MgO smoke powdered substrates was chosen as an appropriate first probe of the system. X-ray diffraction is preferable to other structural probes for several reasons. X-ray studies of the adsorption of other gases on MgO have higher

resolution[72,73,74] than similar neutron diffraction studies,[75,76,77,78] and the contrast between carbon and oxygen is greater for x rays[73] than neutrons. Electron and atom scattering require ultra high vacuum conditions, which limit the accessible temperatures and coverages (higher temperatures and higher coverages have equilibrium vapor pressures outside the range of ultra high vacuum) and require single crystal surfaces which are difficult to prepare and keep clean.[79] Synchrotron radiation is very intense, which greatly reduces the time needed to collect data. This allows for the study of more coverages and temperatures in a given time frame.

Powdered samples are preferable for an initial study such as this for several reasons. First, powdered samples allow for standard theta-two theta x-ray diffraction, from which it is easy to determine to gross features of the adsorbed structure. It is possible to do x-ray diffraction from single crystal substrates,[80,81] but powdered samples are much easier to handle. For example, a chamber capable of single crystal x-ray diffraction of adsorbates on silver required the construction of a dedicated UHV at the cost of 0.5 M dollars, and more than a decade of people-years.[81] A sample holder designed for our CO on MgO studies cost about 20 thousand dollars and perhaps one-third person-year. Also, adsorbed films on powdered samples have an inherently higher scattering intensity because much more of the substrate surface area of the sample (and hence more adsorbed material) is exposed to the x-ray beam. A difficult, expensive single crystal x-ray diffraction study would seem warranted only if simple

powder x-ray and electron studies leave unresolved questions.

We chose to prepare MgO smoke over commercially available MgO powders. MgO smoke made under controlled conditions is a powder of small cubes with the (100) face of the MgO crystal structure exposed. When properly prepared, it is a very homogenous substrate and provides an excellent opportunity to how gasses interact with highly ionic substrates.[82] Commercially available MgO powders have the advantage of larger surface area (≈30 m^2/g) compared to MgO smoke (≈10 m^2/g); however, the heterogeneity of the surface causes adsorbed films to have small coherence lengths and hence broad x-ray peaks. Two-dimensional films on highly homogenous MgO smoke should have long coherence lengths and sharp, easily resolvable peaks.

C. Sample preparation

MgO smoke was prepared in our lab by burning magnesium tape in a controlled atmosphere, following the procedures outlined by Coulomb and Vilches.[82] The sample is prepared in a glove box, containing an anhydrous atmosphere consisting of 80% nitrogen and 20% oxygen. We first purge the glove box for 48 h with dry nitrogen evaporated from a liquid nitrogen dewar (> 99.99% purity). Using flowmeters, a nitrogen/oxygen mixture (both purities > 99.99%) is introduced, allowing several hours for the complete replacement of the nitrogen atmosphere by the mixture. The gas in the glove box is then circulated through a liquid nitrogen trap to further purify it and to remove water vapor.

We purchased 3.2 mm x 0.15 mm magnesium ribbon (99.8% pure) from Alfa Products. Strips approximately 10 cm long are placed inside the glove box, along with the suspension and collection apparatus, prior to purging of the glove box. One end of the suspended strips is electrically ignited by striking an arc to a graphite rod (spectroscopic purity) using approximately 25 VAC. The MgO smoke from the burning strips is collected on a clean stainless steel surface to minimize contamination from the collection process. The ash produced by the strip is discarded, as the MgO produced in the strip is of inferior quality. Using this procedure, we can produce approximately 1 gram of smoke in 4 to 6 h, using about 10 grams of Mg ribbon.

The smoke is harvested from the collection surface into a small quartz tube. This small tube is placed inside a large quartz tube, which is fitted with a vacuum-tight gas manifold and a pressure thermocouple gauge. The large quartz tube is transferred out of the glove box and placed inside a tube furnace (Thermco Pacesetter II). A liquid nitrogen trapped turbomolecular pump is used to evacuate the tube to approximately 10^{-5} Torr vacuum. The sample is baked at 1000°C for approximately 48 h. This differs slightly from the procedure outlined by Coulomb and Vilches,[82] who bake for only 20 h; however, Dash *et al.*[83] found longer bakeouts produce better quality substrates. Once the bakeout is complete, the quartz tube containing the sample is transferred back to the glove box. The sample is then placed in the its sample cell under a dry nitrogen environment.

Our x-ray sample cell design is based on a cell used by

Degenhardt *et al.*[74] It consists of two parts: a sample bakeout end [Fig III.1 (a)] and an x-ray diffraction end [Fig. III.1 (d)]. The bakeout end (a) consists of a small stainless steel chamber welded to a 1.33" conflat flange (b) capable of withstanding bakeout temperatures to 800°C. This is used to clean the MgO surface by mild bakeout from any adsorbed contaminants acquired in the transfer process. The x-ray end consists of a copper block with a 1.5 cm dia. by 4 mm wide sample cavity (d). Be windows are vacuum-sealed to the copper block with indium gaskets (e). A small stainless steel tube (f) connects the copper block to another 1.33" conflat flange (f). The two flanges are sealed with a copper gasket. A stainless capillary tube with a 1/16" Swagelock fitting is welded to the x-ray cell flange (g). This tube is used to dose the MgO sample with adsorption gases. The final step of sample preparation is a mild bakeout at 500°C, under approximately 10^{-5} Torr vacuum.

D. Sample Characterization

Once the sample is prepared, we determine its quality sample with several characterization techniques. Electron micrographs are taken of the smoke samples and on MgO powder commercially made by hydrolyzing MgOH (Alfa Puratonic MgO powder, 99.998% pure). These are shown in Fig. III.2. The Puratonic MgO [Fig. III.2(a)] has irregularly shaped particles, with many defects. The smoke [Fig. III.2(b)], however, has regularly shaped square particles, which are

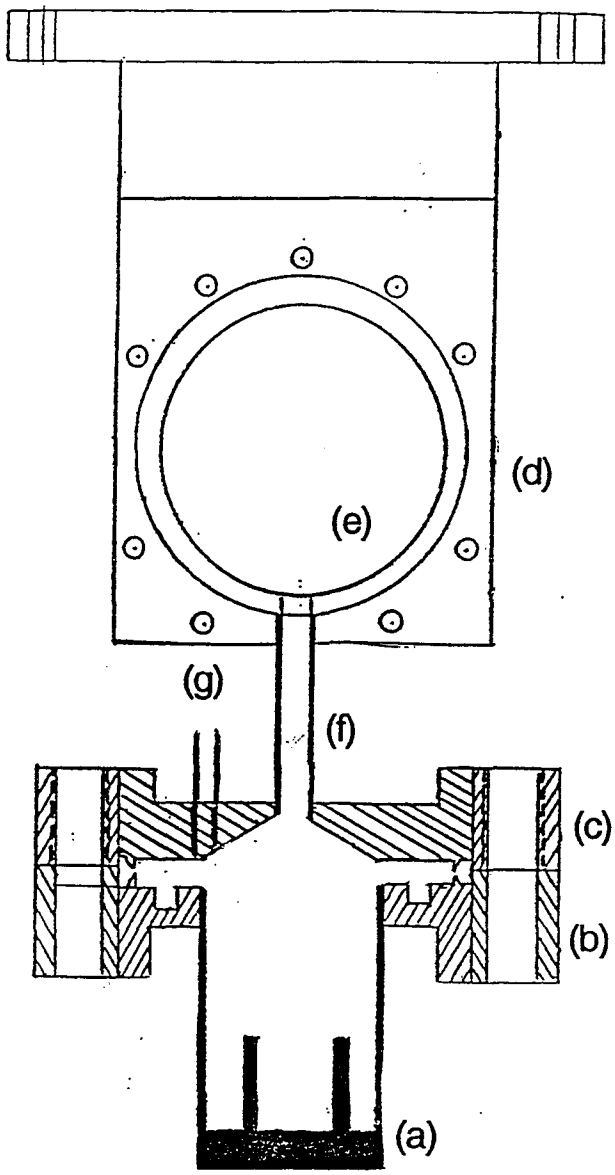

FIG. III.1. X-ray sample cell. The components are as follows: (a) bake out chamber; (b) and (c) 1.33" conflat flanges; (d) x-ray sample cavity; (e) Be windows; (f) stainless steel connecting tube; (g) gas dosing capillary tube.

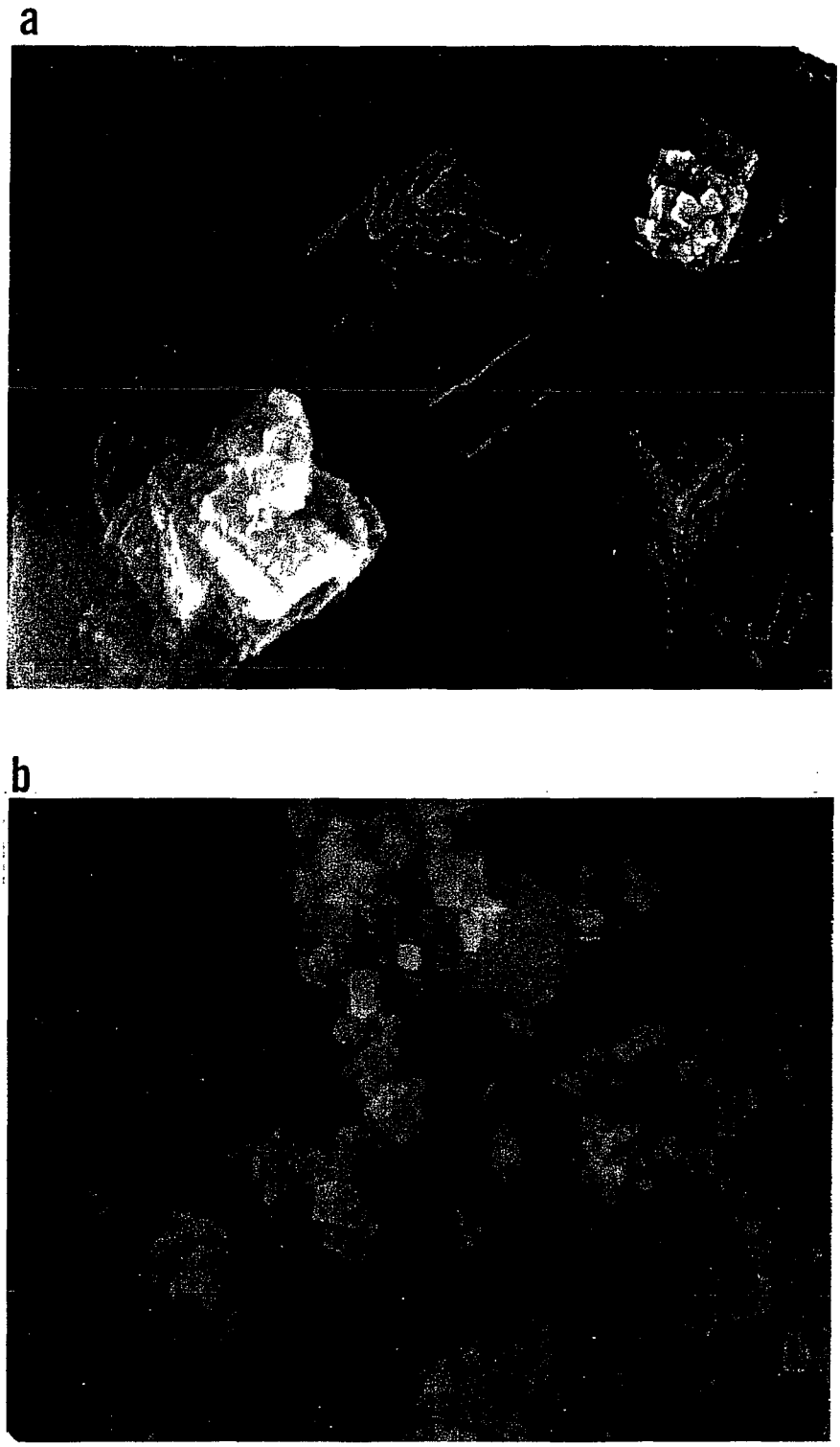

FIG. III.2. Electron micrographs of (a) Puratonic MgO powder and (b) MgO smoke.

generally smooth in appearance. The square shape (symmetry) is indicative of cubes with predominantly (100) surfaces exposed. The smoke particles are as small as 500 ± 30 Å on a side, and as large as 6700 ± 400 Å with most particles falling in the range 1500 ± 100 Å to 2500 ± 200 Å. This is in excellent agreement with other published particle size distributions.[82,84,85] For example, Jones *et al.* measured most smoke particles having side length below 2000 Å, with a few particles above 5000 Å.[84] Moodie and Warble measured particles as small as 400 Å, and as large as 4400 Å, with most particles around 2000 Å on side.[85] Unfortunately, our electron micrograph of MgO smoke has poor resolution and does not allow accurate particle size statistics (i.e., the percentage of particles in a given size range).

The sample is also characterized by performing a vapor pressure isotherm (vpi). The theory of the vpi is described in detail in Appendix B. Briefly, one takes a clean substrate surface and exposes it to a known quantity of gas. Gas will adsorb to the surface, reducing the amount of gas in the 3D vapor phase, until the system reaches an equilibrium vapor pressure. One measures the amount of gas left in the gas phase, and from this calculates the number of particles adsorbed. By plotting the number adsorbed versus the equilibrium vapor pressure, one can gain information about the adsorption characteristics of the adsorbate (see Fig. III.2). Analysis of the vpi can yield information about the substrate specific surface area, isothermal compressibility, isosteric heat of adsorption, and differential molar entropy (see App. B for details).

An isotherm of krypton on a clean, homogeneous, quality MgO substrates exhibits many distinctive characteristics.[82,83,86] First, the homogeneity of the substrate adsorption sites can be measured by the general shape of the curve (see Fig. III.3). The vpi of a homogeneous substrate has a small foot at low equilibrium pressure [Fig. III.2 (a)]. This is characteristic of the chemisorption which takes place on surface heterogeneities, and cube edges.[1] The pressure, and hence the chemical potential, is increased in the system, until a value is reached where physisorption begins (b). This is followed by an almost vertical rise in the vpi curve (c), characteristic of adsorption on many equivalent adsorption sites. The isotherm then bends over (becomes horizontal), when all of the equivalent adsorption sites are filled with Kr atoms (d). In addition, in the temperature range 66 K to 84 K, Kr undergoes a phase transition from a liquid to solid monolayer at slightly higher coverage (e).[86] This is evident in the isotherm as a small substep at $p/p_o = 0.34$, where p is the isotherm pressure, and p_o is the saturation vapor pressure for Kr at the isotherm temperature. Truly high quality isotherms on homogenous substrates will exhibit this substep. Multilayer adsorption of krypton on MgO is evident by a continuing series of steps at higher equilibrium vapor pressures (f and g).

We determine the quality of our MgO substrate by looking for the features described above in isotherms performed on our MgO smoke powders. Also, the substrate specific surface area of our sample is

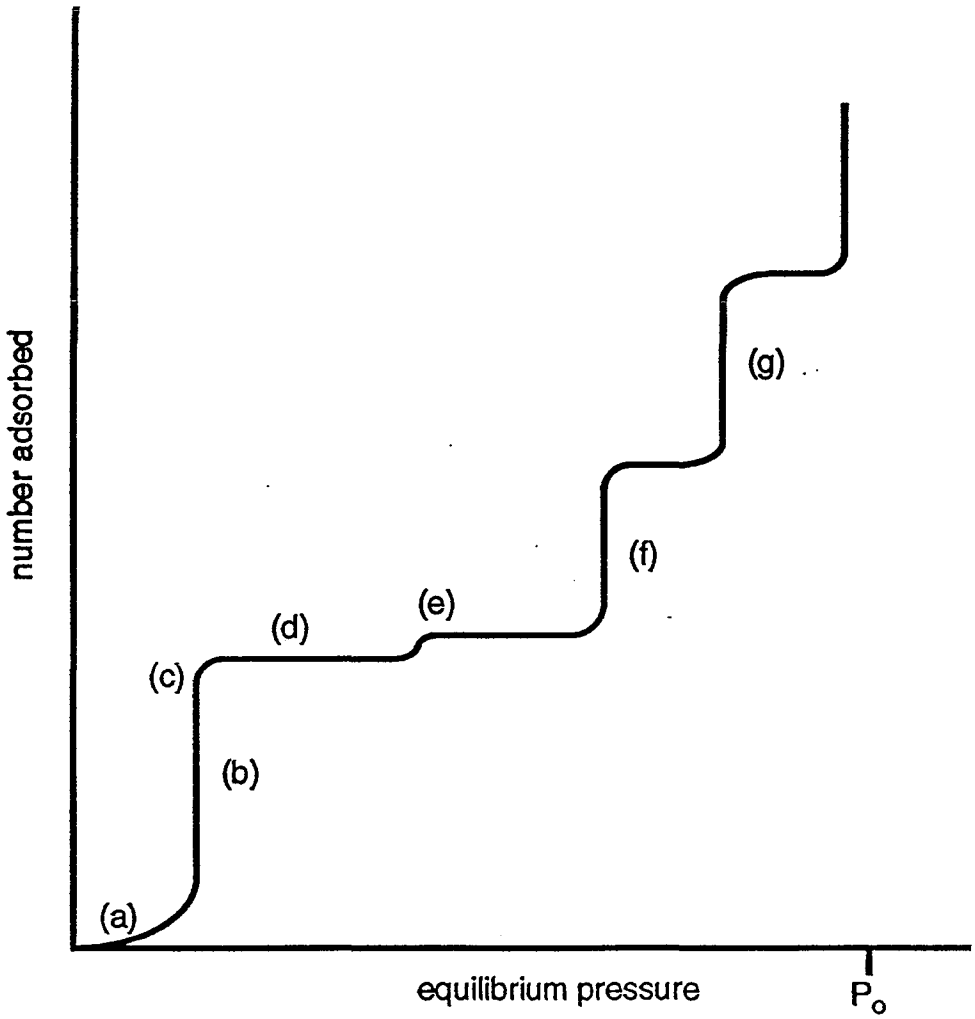

FIG. III.3. Schematic representation of a Kr on MgO isotherm. The labels are described in the text.

compared to that of quality MgO samples reported in the literature. The specific surface area is computed by measuring the number of Kr atoms adsorbed at monolayer coverage, and multiplying by the area per Kr atom.

Figure III.4 shows two vapor pressure isotherms done on MgO smokes made in our lab. For both isotherms, low temperature was achieved by immersing the sample cell in a liquid N_2 bath (T = 77.3 K at 760 Torr). Since our lab is approximately 1400 m above sea level, the ambient pressure is about 650 ± 50 Torr and the temperature of our liquid nitrogen bath is considerably lower (76 ± 0.5 K). We provide no further temperature control, and estimate the temperature stability due to atmospheric variatons to be 1.5 K. Figure III.4(a) is a vpi of Kr on MgO at 76 K plotted to show monolayer condensation. The vpi has many of the characteristics of a quality MgO substrate. It has a small foot, followed by an almost vertical region. The isotherm then bends over, after completion of the first layer. Our isotherms do not exhibit the small substep associated with the liquid-solid phase transition. We do observe an appreciable change in the derivative of the isotherm at approximately the correct pressure for the substep (P_{sub} = 0.3 ± 0.05 Torr; see Fig. III.4).

There are possible two reasons we do not observe the substep in the isotherm. First, the substep is most pronounced at 77.5 K, i.e., it has its sharpest rise at that temperature. At temperatures only one or two degrees away from 77.5 K, the step is significantly less pronounced.[86] We did not have adequate temperature control to ensure

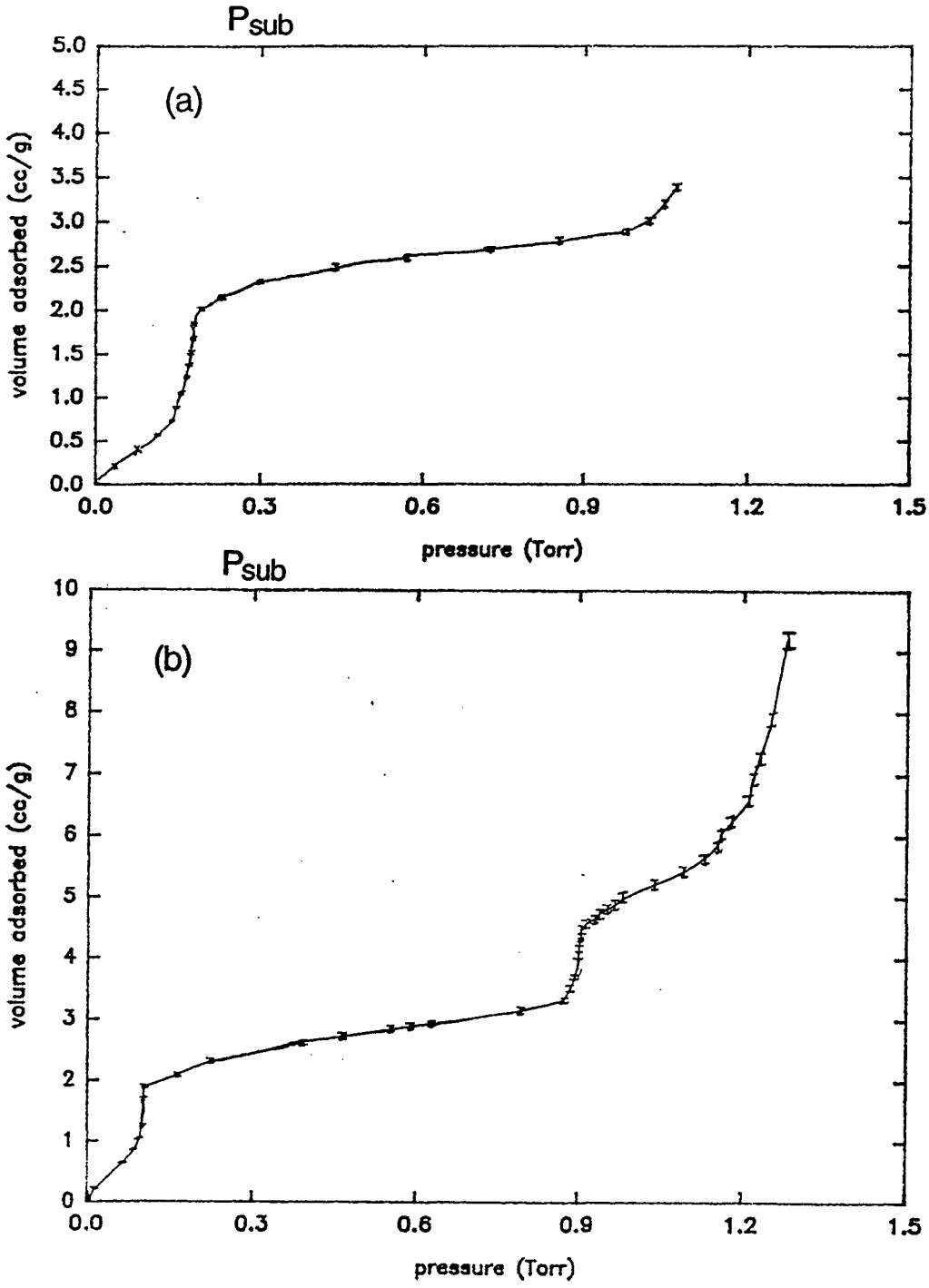

FIG. III.4. (a) Vapor pressure isotherm of Kr on MgO smoke (76 K) in the monolayer region. (b) Multilayer isotherm of Kr on MgO smoke (76 K). The numbers indicate layer formation. P_{sub} is the approximate pressure where the substep is expected.

that our vpi is performed at the optimum temperature. Indeed, our isotherms were done at 76 K, less than the optimum temperature of 77.5 K. The second reason is that our gas handling system may not have sufficient accuracy to distinguish the step. At its sharpest, the step corresponds to a 4% increase in the number adsorbed at the phase transition equilibrium pressure. At the equilibrium pressure of the step (approximately 0.3 ± 0.05 Torr at 76 K[86]), our system has 1 to 1.5% accuracy. If the rise is spread over several data points, we may not be able to distinguish a step from the gentle slope evident in this region in the vpi.

Figure III.4(b) is a multilayer isotherm of Kr on MgO, also at 76 K. This isotherm shows the multilayer characteristics of Kr on MgO. Up to four steps are clearly distinguishable before saturation vapor pressure (1.40 Torr) is reached.

One can determine the specific surface area of the MgO smoke samples. This is an important measure of the homogeneity of the substrate. The most homogeneous substrates have specific surface areas ranging from 5 to 15 m^2/g,[82,83,86,87,88] with most values close to 10 m^2/g. Less homogenous substrates have specific surface areas of 25 m^2/g and higher. Indeed, the sample used for the vpi of Fig. III.4(a) has a specific surface area of 8.88 ± 0.05 m^2/g, while the multilayer sample [Fig. III.4(b)] has a specific surface area of 9.42 ± 0.05 m^2/g.

From the isotherm shape, and the specific surface area of our sample, we conclude our samples are appropriate for use in the study

of gas adsorbed to regular ionic crystalline substrates. Our samples exhibit isotherms which have almost all of the features found in isotherms of Kr on other quality samples. While we did not see the substep, we believe this is due to experimental uncertainty, rather than lack of substrate quality. Indeed, most published isotherms do not exhibit the substep. Those which do are measured at the optimum temperature and greater system accuracy.[86] The measured specific surface areas of our samples compare favorably with those published in the literature. We conclude our smoke samples are clean and homogeneous, and therefore appropriate for the x-ray studies.

E. X-ray diffraction studies

We used the MATRIX PRT (X18A) beamline at the National Synchrotron Light Source at Brookhaven National Laboratory.[89] The beamline has all the necessary equipment to perform theta-two theta diffraction on powdered substrates for a range of temperatures and coverages. The beamline and diffractometer, as well as the powdered diffraction technique, are described in App. A. Briefly, a specially designed MgO sample holder (Fig. III.1) mounts inside a closed-cycle He cryostat. The cryostat fits at the center of a 50-cm diameter Huber circle in a four circle diffractometer. The cryostat allows for accurate sample temperature control between 10 K and 300 K (± 0.1 K). Both the sample cell and the cryostat are fitted with Be windows which allow a focussed beam (approximately 15 mm^2) to pass through the sample. We use a 1.55 Å wavelength beam, as set by a double crystal

monochromator. The scattered signal is resolved to approximately 0.02 $Å^{-1}$ by 20" Soller slits used in conjunction with a scintillation counter.

After completing the Kr isotherm [Fig. III.4(a)], a monolayer coverage of CO was dosed into the sample cell. The sample cell was sealed and transported to BNL. The cell was placed in its experimental position at the end of the cryostat, and the temperature was lowered. We then annealed our sample by raising the system temperature to 80 K, and lowering the temperature at a rate of 0.5 K/min to our scan temperature.

The sample characterized in Fig. III.4(a) was the sample we ultimately used in our diffraction studies at Brookhaven National Laboratory. As discussed above, we believe this substrate to be clean and atomically smooth. We were not able, however, to detect any scattering from CO adsorbed on this sample.

There could be several reason for this. If our sample was dirty, or highly heterogeneous, CO would not have a 2D crystal structure on the MgO substrate with a sufficiently long coherence length (leading to very broad peaks, see App. A). However, our vpis clearly indicate 2D layer formation. Other reasons may include the absence of CO in the scattering volume (due to, e.g., a cold spot in the sample cell), or the absence of MgO in the scattering volume. While it is not possible to entirely rule out the first, it is unlikely. The sample is mounted to the end of a temperature controlled coldfinger. There was no contact between the cell and any

cold surfaces inside the cryostat. Annealing of the sample should promote layer formation, i.e., if any bulk crystallites did form, raising the temperature and slowly lowering should allow CO to equilibrate on the MgO surface. The second can be ruled out by the observation of MgO bulk peaks in the x-ray diffraction scan. These peaks were routinely observed in our scans (see Fig. III.5).

The most likely reason we did not observe CO peaks is that the scattering intensity of CO is simply not strong enough to allow the detection of the 2D peaks. We can perform two important tests of this hypothesis. First, we can use the measured intensity of a much stronger scatter on MgO to determine what the scattering intensity of CO on MgO would be. We can also compute the time for a scan of CO on MgO based on the time per scan for a different scattering experiment. Both of these methods should give us an order of magnitude idea of how much time it would take to measure a CO peak.

Both estimation methods are based on the theoretical scattering intensity for an adsorbed film; for point scatterers, it is:

$$I \propto Z^2 N, \tag{III.1}$$

where Z is the number of electrons in the point scatterer, and N is the number of scatterers. The total number of scatterers in the adsorbate seem by the x-ray beam is given by:

$$N = \sigma h s \rho A_{uc} n, \tag{III.2}$$

where σ is the crossectional area of the beam, h is the substrate sample thickness, s is the specific surface ares of the substrate, ρ is the density of the substrate, A_{uc} is the area per molecule of the

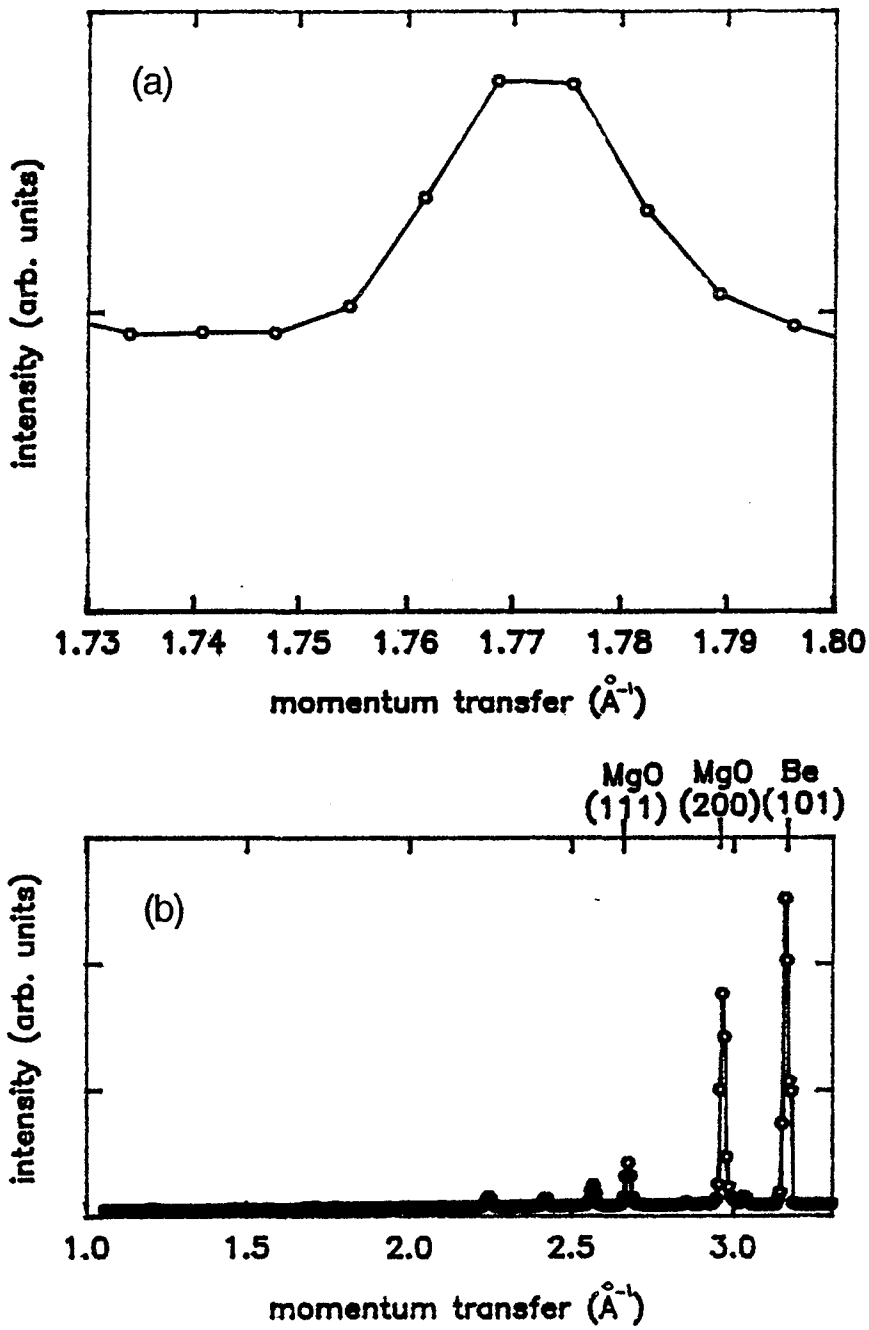

FIG. III.5. X-ray diffraction scans of 10 ML of Xe on MgO. (a) a detail of (b) showing the Xe bulk peak. (b) A scan over an extended momentum transfer range. MgO and Be peaks are indexed on the upper axis.

adsorbate, and n is the number of layers of the adsorbate. We can make comparisons of the time needed for data collection by equating the intensity of the peaks in an x-ray scan multiplied by the time for data collection for specific peaks, i.e.:

$$I_x t_x = I_y t_y. \tag{III.3}$$

First we calculate the time needed for an x-ray scan of CO on MgO by comparing to Xe on MgO, i.e.:

$$I_{CO} t_{CO} = I_{XE} t_{XE}. \tag{III.4}$$

We took a diffraction scan of ten layers of Xe on MgO in the same x-ray cell as used for CO on MgO, under the same experimental conditions (i.e., t, σ, s, and ρ are equal for both experiments). Therefore, only differences in the adsorbate such as Z and A_{uc} account for differences in scattered intensity. However, the x-ray beam intensity flucuates somewhat, and we include a scaling factor to account for this. This is estimated from the ratio of the intensities of the most intense MgO peak seen in the Xe and CO scans. The time for a CO scan is then:

$$t_{CO} = t_{Xe} \frac{Z_{Xe}^2}{Z_{CO}^2} \frac{A_{uc_{Xe}}}{A_{uc_{CO}}} \frac{I_{MgO(Xe)}}{I_{MgO(CO)}}, \tag{III.5}$$

where $I_{MgO(Xe)}$ ($I_{MgO(CO)}$) is the intensity of the MgO (200) peak in the Xe (CO) scan. The intensity is taken to be the number of counts in an angular range of 1.4° centered on the peak at 42.9° in two theta.

The most significant difference in the scattering intensity of CO and Xe is due to the difference in the number of electrons. If we approximate both CO and Xe as point scatterers, this alone would

increase the time to measure a CO scan fifteen-fold. Other factors in Eq. III.5 increase this to sixteen-fold, if the Xe peak in Fig III.5 is due to monolayer scattering, or to 160-fold, if the scattering is due to the full 10 layers we measure (and there is little desctructive interference of the x-ray beam bewteen layers). Data collection for the scan in Fig. III.5 took 6 h. A scan of CO on MgO which includes a CO peak with similar intensity would take 98 to 980 h for data collection. [Note: Our experimental runs typically had about 120 h of x-ray beam.]

A different way to determine whether it is possible to measure CO adsorbed on MgO is to compare the scattered intensity to that measured on a different adsorbate-substrate system. For hexane adsorbed on graphite, a diffraction scan took approximately 6.4 h for data collection. Again:

$$I_{hex}t_{hex} = I_{CO}t_{CO}. \qquad \text{(III.6)}$$

In this case, the substrate, adsorbate and sample cell were all different. Also, the synchrotron source and beamline underwent improvements which increased the photon flux at the sample by a factor of two, between the time the hexane on graphite and CO on MgO experiments were done.

Therefore, the estimated time for a CO scan is:

$$t_{CO}=\frac{t_{hex}}{2}\frac{z_{hex}^2}{z_{CO}^2}\frac{A_{uc_{hex}}}{A_{uc_{CO}}}\frac{\sigma_{hex}}{\sigma_{CO}}\frac{h_{hex}}{h_{CO}}\frac{s_{graph}}{s_{MgO}}\frac{\rho_{graph}}{\rho_{MgO}}, \qquad \text{(III.7)}$$

where the factor of 2 accounts for the beam improvements. This calculation determines that the time for a CO on MgO scan is 44 h.

While this is less 98 h, it is still on the edge of what is reasonably measurable.

One question we can ask is, why is there such a disparity in the time per scan predicted for both methods? We believe this is due to an uncertainty in the substrate density in the scattering region. Using different sample treatments, we have prepared MgO samples with densities from 0.06 g cm^{-3} to 0.39 g cm^{-3}. The sample used in the x-ray studies at BNL had a density of 0.16 g cm^{-3} in the heated region of the sample cell (determined by measuring the mass of the MgO in the known volume of the heated region). These different densities were prepared by different packing techniques. The lowest density sample was simply poured into a known volume, while the highest density sample received much tamping and pressing into the same known volume. The BNL sample received mild tamping and pressing while being loaded into the heated portion of the sample cell. We do not have any control, however, over the treatment the MgO receives once it is placed in its experimental position at BNL. We expect that it was rather well packed, due to the mechanical motion of the helium refrigerator to which it was attached. However, restricted MgO flow from the sample heating region to the x-ray region may have resulted in lower density. While we tested the sample flow to be unhindered, we have no way of monitoring this once the sample is sealed.

F. Conclusions

MgO smoke samples were prepared, and measurement determined

them to be appropriate for x-ray diffraction studies of CO on MgO. These studies did not prove fruitful, due to the unfortunate scattering characteristics of CO. The phase diagram of CO on MgO remains virtually unmapped, as the only structural measurements to date are the LEED experiments discussed above. This needs addressing, as a complete understanding of the submonolayer and monolayer behavior is essential to our understanding of the complicated asymmetric adsorbate-substrate interaction involved in this system.

Other structural techniques may prove to be more useful in the study of CO on MgO. Indeed, a group from Marseilles, France, intends to undertake powered neutron diffraction studies.[90] The relative scattering intensity of the CO can be manipulated and improved by using a particularly neutron active isotope of CO. Neutrons studies do not have the resolution that x-ray studies do, and this may be a hindrance to measuring diffraction scans and mapping out the 2D phase diagram. However, neutrons do not attenuate at larger momentum transfer, unlike x rays, due to the lack of an atomic form for neutrons. This allows measurement of more high index peaks that are used to analyze adsorbate orientation (see, e.g., Ref. 12). Other techniques, such as helium scattering, which has been successful in studying CO on NaCl,[47] should also be employed. This experiment is more difficult than powder diffraction experiments as it requires a single crystal substrate, and UHV conditions.

Other valuable information can be obtained from dynamic measurements. Polarization studies of CO on high quality MgO using ir

spectroscopy could determine whether CO adsorbs perpendicularly to the MgO surface (see, e.g., Ref. 62). Another important technique under development is metal light pipe spectroscopy. Using this method, one can directly correlate subtle changes in the ir spectrum with thermodynamic information.[91,92,93] This would be vital to correlating phase transitions with thermodynamic information like the equilibrium vapor pressure of the adsorbed species. Also, previous powder ir studies have used poor quality MgO substrates. Replacement of the poorer quality substrates with higher quality substrates should improve our understanding of the dynamics of the system. Hopefully, new phenomena measured as a function of temperature and coverage will be observed.

CHAPTER IV

MULTILAYER PHASE TRANSITIONS OF NITROGEN ON GRAPHITE

A. Introduction

Physisorbtion of a nonspherical molecule is the simplest method of introducing asymmetries into adsorption systems, as discussed in the introduction (see Chapter I, Sec. B.5). Shape asymmetries allow for orientational ordering phase transitions in the 2D (and 3D) systems, which cannot occur for the spherically symmetric molecules such as the rare gasses or methane. An interesting question arises: if an incomplete to complete wetting transition in the 2D system can be driven by the 3D melting transition, can we expect other 2D phase transitions to be actuated by other 3D phase transitions? In order to observe such a phenomenon, we must identify an adsorbate with 3D phase transitions other than condensation and melting in a temperature and pressure range where physisorption occurs. The 2D system should allow the possibilty of 2D phase transitions. For example, an assymmetric adsorbate which has an orientational 3D phase transition, and which is an incomplete wetting system on a substrate may exhibit a 2D phase transition (i.e., a wetting or layering transition), driven by the 3D phase transition (i.e., an orientational phase transition).

N_2 adsorbed on graphite is an ideal system for addressing this question. N_2 has an ellipsoidal shape, and hence lacks the spherical symmetry of a rare gas atom. Bulk (3D) nitrogen exhibits a phase transition from an α-phase to a ß-phase at $T_{\alpha-ß} = 35.5$ K. This phase

transition is due an orientational order-disorder transition. In α-phase nitrogen, the N_2 molecules sit at the sites of an fcc lattice, and are oriented, with their molecular axes perpendicular.[28] In ß-phase nitrogen, the structure tranforms to a hcp lattice, and each N_2 molecule rotates about its lattice position.[28] [Figures of the α- and ß-N_2 crystal structure are found in Ref. 28.] N_2 is observed to incompletely wet graphite at low temperature. Indeed, recent ellipsometry experiments observed the number of 2D layers to increase as the temperature of the system is increased, beginning at $T_{\alpha-ß}$.

For N_2 on graphite, the 2D layering transition observed in the ellipsometry experiments associated with the α-ß 3D phase transition appears to be one physical manifestation of a 3D phase transition driving a 2D phase transition in this system. Triple point wetting, which is inferred for this system in the ellipsometry study, is another. In our study of this system, we are interested in independently observing the layering transitions, and in providing insight into the structure of the bulk material and the 2D layers. This is important collaborative evidence because ellipsometry is sensitive only to film thickness and not structure.

We choose x-ray diffraction structural analysis of N_2 on graphite foam for several reasons. Exfoliated graphite foams have a large specific surface area. These substrates are produced by acid expansion of the c-axis of graphite. This produces a very low density substrate. Actual experimental substrates are produced by varying amounts of compression of the low density substrate. After

compression, the exfoliated graphite samples have densities varying from 0.1 to 1 g cm^{-3}. The samples have specific surface areas of about 25 m^2 g^{-1}. This translates into many adsorption sites, and allows measurements such as vapor pressure isotherms and heat capacity. The large specific surface area makes exfoliated graphite ideal for powder diffraction studies as well, because of the large number of adsorbed molecules available for sampling by the x-ray beam. Powder diffraction is chosen for the ease and thrift of the experiments. This has been discussed in conjunction with the CO structural studies presented in Chapter III (see Sec. B).

Exfoliated graphite samples, however, have a pore structure where capillary condensation of the adsorbed species can occur. This capillary condensation can complicate quantification of condensed gas conduct. Indeed, estimates of the amount of material in a 2D phase may be overestimated due to material absorbed in pores. Also, interpretation of temperature behavior of adsorbed species can be convoluted with temperature effects due to finite crystal size, and capillary condensation. This is especially important for layering, wetting, and roughening studies where adsorbed species behavior is studied as a function of temperature.

Layering transitions of N_2 were observed by ellipsometry on an highly oriented pyrolytic graphite (HOPG) substrate.[23] This substrate is equivalent to a single crystal substrate in many ways. It presents highly oriented graphite (002) planes as its adsorption surface. Ellipsometry is a technique that requires a single surface substrate.

It involves measuring the thickness of an adsorbed layer by montoring the phase shift of a laser beam focussed on the single surface substrate. Many other adsorption techniques (such as vapor pressure isotherms, heat capacity measurements, and powder diffraction studies) require substrates with a much higher surface area than that provided by single crystal substrates.

Powder x-ray diffraction scans of eight layers of N_2 on graphite are measured and interpreted. The results of these studies are put in context by preparing a multilayer N_2 on graphite phase diagram. The effects of using a porous graphite foam sample are carefully examined. We attempt to quantify the effects on the layering transitions we observe. Consideration for this is made in analysis, and the layering transitions are interpreted accordingly.

Chapter IV is organized in the following manner. First we review previous work on the structure of N_2 on graphite (Sec. B). The x-ray data are then described and interpreted to indicate layering layering transitions of multilayer N_2 on graphite (Sec. C and D). These data (and other measurements) are used to extend the multilayer phase diagram of N_2 on graphite to higher coverage and higher temperature regions than previously explored (Sec. E). Capillary effects in general physisorption systems are described and quantified, and are used to interpret the N_2 on graphite system studied here (Sec. F). We then discuss ways that one can measure the capillarity of a porous sample (Sec. G).

B. Review of structure of N_2 on graphite

Nitrogen on graphite is one of the most extensively studied physisorption systems (see Fig. IV.8). Its multilayer structure at low temperatures has been studied by neutron diffraction,[94] heat capacity measurements,[95] and by computer simulation.[96] Monolayer nitrogen is commensurate to the graphite substrate ($\sqrt{3} \times \sqrt{3}$) and has herringbone molecular orientations; the monolayer compresses $\approx$ 10% to form an incommensurate structure at higher coverage.[12,65,97] The bilayer structure is also compressed incommensurate. The two layers in the N_2 bilayer are commensurate with each other. The exact molecular orientations are still uncertain.[94] Nitrogen at low temperature has been found to incompletely wet graphite at still higher coverages.[20,94]

Higher temperature, higher coverage nitrogen films on an HOPG substrate exhibit interesting wetting and layering phenomena, as recently observed by ellipsometry isotherms.[23] Nitrogen on graphite is found to undergo a series of layering transitions, the first occurring at $T_{\alpha-\beta} = 34 \pm 0.5$ K (this transition temperature is depressed 1 K for small crystallites[95] compared to large bulk nitrogen samples, where $T_{\alpha-\beta} = 35$ K[28]).

In the ellipsometry isotherms, at temperatures below $T_{\alpha-\beta}$, a maximum of two to four film layers formed before bulk nucleation began (incomplete wetting), in agreement with neutron diffraction.[94] The bulk nitrogen condenses in an epitaxial alpha phase (α-N_2), which is optically smooth. Hence, the onset of bulk nucleation is inferred from stabilization of the equilibrium vapor pressure at the value

appropriate for the isotherm temperature. The existence of one to two amorphous layers above the ordered bilayer is inferred, to compensate for the lattice mismatch between the bilayer and the epitaxial α-N_2 crystal structures. This low temperture behavior agrees with neutron studies of this system.[94] For the adsorption isotherms, between two and four layers are observed before bulk nucleation. For desorption isotherms, only two 2D layers are observed. Therefore, significant hysteresis between adsorption and desorption ellipsometry isotherms is seen.[23]

At temperatures above $T_{\alpha-\beta}$, multilayer nitrogen on HOPG was observed with ellipsometry to undergo a series of layering transitions, beginning near $T_{\alpha-\beta}$ with subsequent layering transitions occurring as the temperature increased. At T = 35 K ± 0.5 K, five layers formed before bulk nucleation; subsequent layers formed at 38 K, 40 K, 44 K, 46 K, and 50 K. A maximum of ten layers of film was observed before bulk nucleation began. The bulk beta nitrogen (ß-N_2) was not epitaxial, and hence optically rough. There was little hysteresis observed in the isotherms above $T_{\alpha-\beta}$.[23]

Nitrogen on graphite does indeed have all the required elements to study the effect of 3D transitions on 2D phase transitions. We intend to address with structural measurements the layering transitions observed with the ellipsometry.

C. Experimental design

Standard x-ray diffraction in a transmission geometry was done

at the MATRIX PRT beam line (X18A) at the National Synchrotron Light Source at Brookhaven National Laboratory. The beamline and technique are described in detail in Appendix A. Briefly, a double crystal Si(111) monochromator set the wavelength to 1.550 Å. The x rays were focussed both horizontally and vertically using a bent, cylindrical, platinum-coated mirror. A resolution of 0.02 $Å^{-1}$ FWHM was achieved using Soller slits between the sample and a NaI scintillation detector. The sample is contained in a copper cell 1.2 cm thick fitted with Be windows. The cell was mounted on a closed cycle He refrigerator with a temperature stability of ± 0.1 K.

The sample is 0.68 ± 0.02 g of graphite foam with a density of 0.24 g/cm^3 and a specific surface area of 33.8 ± 0.1 m^2/g, as measured by a vapor pressure isotherm of N_2 on graphite at T = 76 K. Monolayer coverage (θ = 1 ML) was designated as the amount of nitrogen adsorbed at the foot of a substep in the isotherm resulting from a liquid-solid phase transition. This coverage unit corresponds to the amount of material needed to complete the commensurate $\sqrt{3}$ x $\sqrt{3}$ solid monolayer, and is the same as that used in Refs. 23 and 94. The definition of a coverage unit (θ = 1 ML) allows us to make consistent comparisons of amounts of nitrogen. For example, the amount of N_2 in bulk form can be designated 4 ML, meaning the amount of N_2 in bulk is equivalent to the amount of N_2 needed to form four $\sqrt{3}$ x $\sqrt{3}$ monolayers. The sample cell is filled with θ = 8.00 ± 0.05 ML of nitrogen at 60 K, and sealed. The film is then annealed at 80 K for approximately 1 h, and the temperature slowly lowered to 32 K at a rate of 0.5 K per min.

A sample coverage of 8.0 ML was selected because Volkmann and Knorr predicted three distinct layering transitions should be observed above $T_{\alpha-\beta}$ and before complete disappearance of the bulk peaks.[23] This coverage was also studied by neutron diffraction at lower temperature.[94]

A diffraction scan below $T_{\alpha-\beta}$ confirmed that a 2D compressed incommensurate film coexisted with α-N_2 [Fig. IV.1(a)]. The position of the N_2 (20) peak agrees with that measured by previous scattering experiments,[93] and the peak has the asymmetric shape expected for 2D peaks (discussed in App. A). Diffraction scans were taken at approximately 2 K intervals up through the ß-N_2 triple point temperature (T_{tp} = 63 K). The temperature of the sample was then monotonically decreased in approximately 2 K increments to 30 K, well below $T_{\alpha-\beta}$. The scans typically took 1 h each to complete, depending on x-ray beam conditions.

D. Results and analysis

1. Normalization and peak selection

After measuring diffraction scans at many temperatures, we look for evidence of layering transitions. In our diffraction scans we see peaks which correspond to the three structurally ordered phases of nitrogen possible in our experimental temperature range. Very strong evidence of layering is peak intensity changes as the temperature is varied. In our experiments, we expect to see 3D peak intensities decrease with increasing temperature, and for the 2D peak intensities

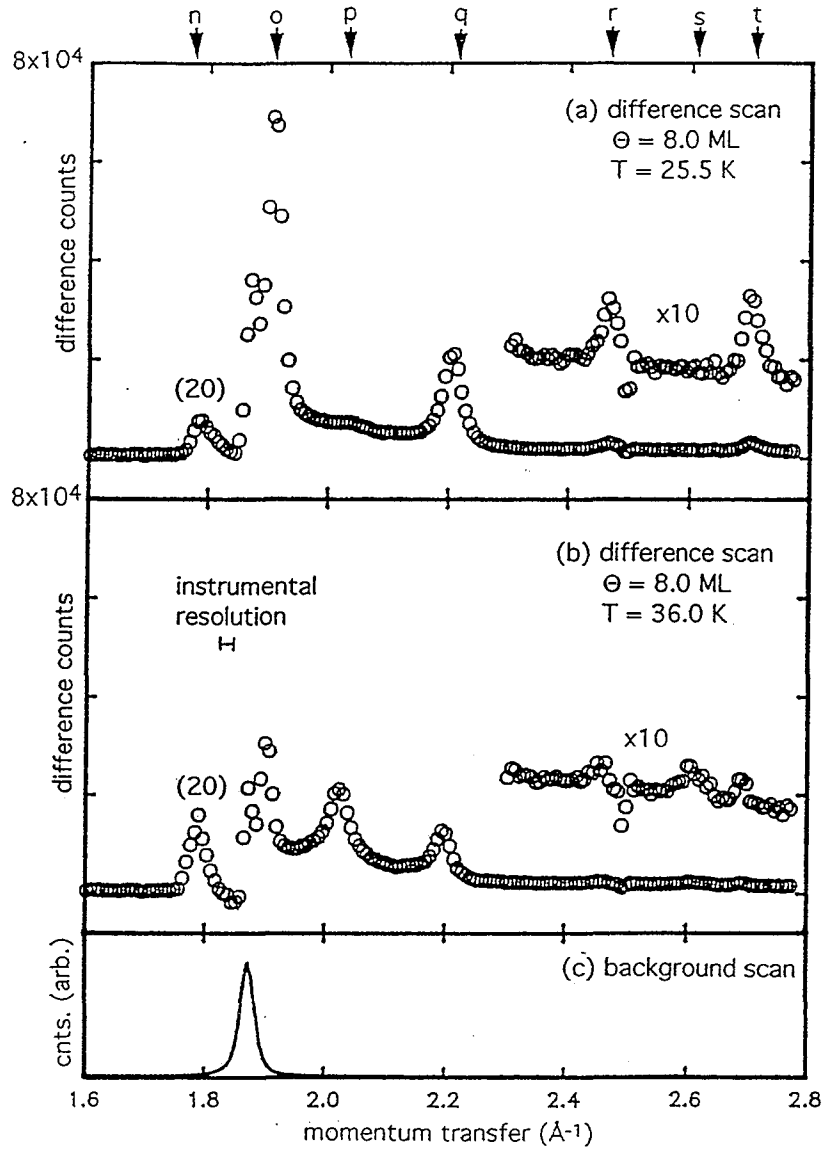

FIG. IV.1. (a) Typical diffraction scan of 8.0 ML nitrogen physisorbed on graphite foam at 25.5 K after subtraction of a scaled substrate background. The compressed monolayer N_2 (20) peak is labeled at q = 1.78 $Å^{-1}$. All the possible bulk diffraction peaks which occur in the measured momentum transfer range are indexed as follows: n = ß-N_2 (100), o = α-N_2 (111), p = ß-N_2 (101), q = α-N_2 (200), r= α-N_2 (201) & (210), s = ß-N_2 (102), and t = α-N_2 (211). The high momentum transfer scattering is presented on an expanded vertical scale. (b) Typical diffraction scan of 8.0 ML nitrogen physisorbed on graphite foam at 36 K after subtraction of a scaled substrate background. The high momentum transfer scattering is presented on an expanded vertical scale. (c) Diffraction pattern of bare graphite foam. The peak corresponds to the graphite (002) peak.

to increase or remain the same, depending on the structure of the 2D layers grown. We also want to quantify the amount of material in each phase, to make direct comparisons to ellipsometry experiments.

In order to monitor the relative amounts of the different species of nitrogen present in our sample cell, we assume that the intensities of the diffraction peaks for a given phase are proportional to the relative amount of nitrogen in the cell existing in that phase. This method was used successfully in previous studies.[24,25,94,98] Specifically, layering transitions for iron pentacarbonyl[25] and ethylene[24] were inferred from a decrease in bulk phase Bragg peak intensity.

Figure IV.1 shows typical diffraction scans over an extended momentum transfer range both above and below $T_{\alpha-\beta}$ after background scattering is subtracted. The background scattering of bare graphite [Fig. IV.1(c)] is removed from the nitrogen diffraction patterns by point-by-point subtraction of a scaled background scan. Background scans are taken at three temperatures (T = 25 K, 35 K, and 55 K) to minimized temperature dependent errors in subtraction. Each adsorption scan is matched with the background scan closest in temperature. The background scan is then normalized in two ways. First, it is scaled to the same counting time as each adsorption scan. After normalization for counting time, simple subtraction of the background scan leads to large negative intensity peaks in the positions of the graphite peaks. Secondly, it is scaled to account for absorption of the x rays by the nitrogen. Based on the amount of

nitrogen in the cell and the tabulated absorption coefficients, we estimate the graphite peaks are attenuated by 15% by nitrogen absorption.[99] When this normalization is used in the subtraction of the background scans from the adsorption scans, the subtraction leads to more reasonable residuals instead of large negative peaks.

There are several peaks evident in each subtracted scan. We chose one peak to monitor in detail from each solid crystalline phase of nitrogen, based on its proximity to other peaks and its intensity. For α-N_2, we can identify the α-N_2 (111), the α-N_2 (200), the α-N_2 (201) & (210), and the α-N_2 (211) in Figures IV.1(a) and IV.1(b). We chose to monitor α-N_2 (200) because it is well separated from all appreciable peaks, and it is more intense than the α-N_2 (211). The α(200) peak does overlap a very weak (21) film peak; however, the (21) intensity is nearly zero above the 2D orientational disordering transitions at 28 K and 30 K, as observed in a previous x-ray diffraction monolayer study.[65,94] The ß-N_2 (100), (101), and (102) peaks are evident. We chose the ß-N_2 (101) because it is clear of other peaks and it is the most intense of the three peaks. Other bulk peaks seen are used to corroborate trends in the monitored peaks. There is only one monolayer film peak which is intense enough to monitor in x-ray diffraction scans, the (20) peak at q = 1.79 $Å^{-1}$.[65] Unfortunately, the (20) peak coincides with the ß-N_2 (100) peak and is adjacent to the graphite (002) peak. Thus, accurate determination of the relative amount of film in coexistence with ß-N_2 is difficult; this is discussed further below.

2. X-ray diffraction data

In order to probe as many temperatures as possible in our limited synchrotron x-ray beam time, most of our scans are taken over a limited range in two-theta. This range was chosen to include the N_2 (20) peak, the ß-N_2 (101), and the α-N_2 (200). The range extended from $2\theta = 24.5°$ to 30° ($q = 1.72 - 2.10$ Å^{-1}) and $2\theta = 31°$ to 33° ($q = 2.17 - 2.30$ Å^{-1}). The angular resolution (or step size) varied from 0.1° to 0.05°. We use smaller step sizes in the angular regions where nitrogen peaks are expected.

Figure IV.2 is a plot of the x-ray scans taken for T = 30 to T = 64 as T was monotonically increased. Note that 2θ is converted to momentum transfer [$q = (4\pi/\lambda)\sin\theta$, where λ is the wavelength of the x rays, and θ is the position of the diffraction peak; see App. A]. Data is excluded in the momentum transfer range $q = 1.84$ Å^{-1} to $q = 1.90$ Å^{-1} for the large graphite (002) peak at $q = 1.87$ Å^{-1}. This is the same range used by Mochrie *et al.* in a similar study of ethylene on graphite.[24] Imperfect subtraction of the background leads to erratic behavior of the data in this region. This is correlated to the temperature dependence of the graphite (002) peak position. We attempt to minimize this by taking background scans at several temperatures. We require background scans at each temperature to further reduce this effect; this would make the experiment prohibitively long.

Peaks associated with the N_2 (20) film peak, the ß-N_2 (101), and the α-N_2 (200) are observed (Fig. IV.2). The intensity seen at

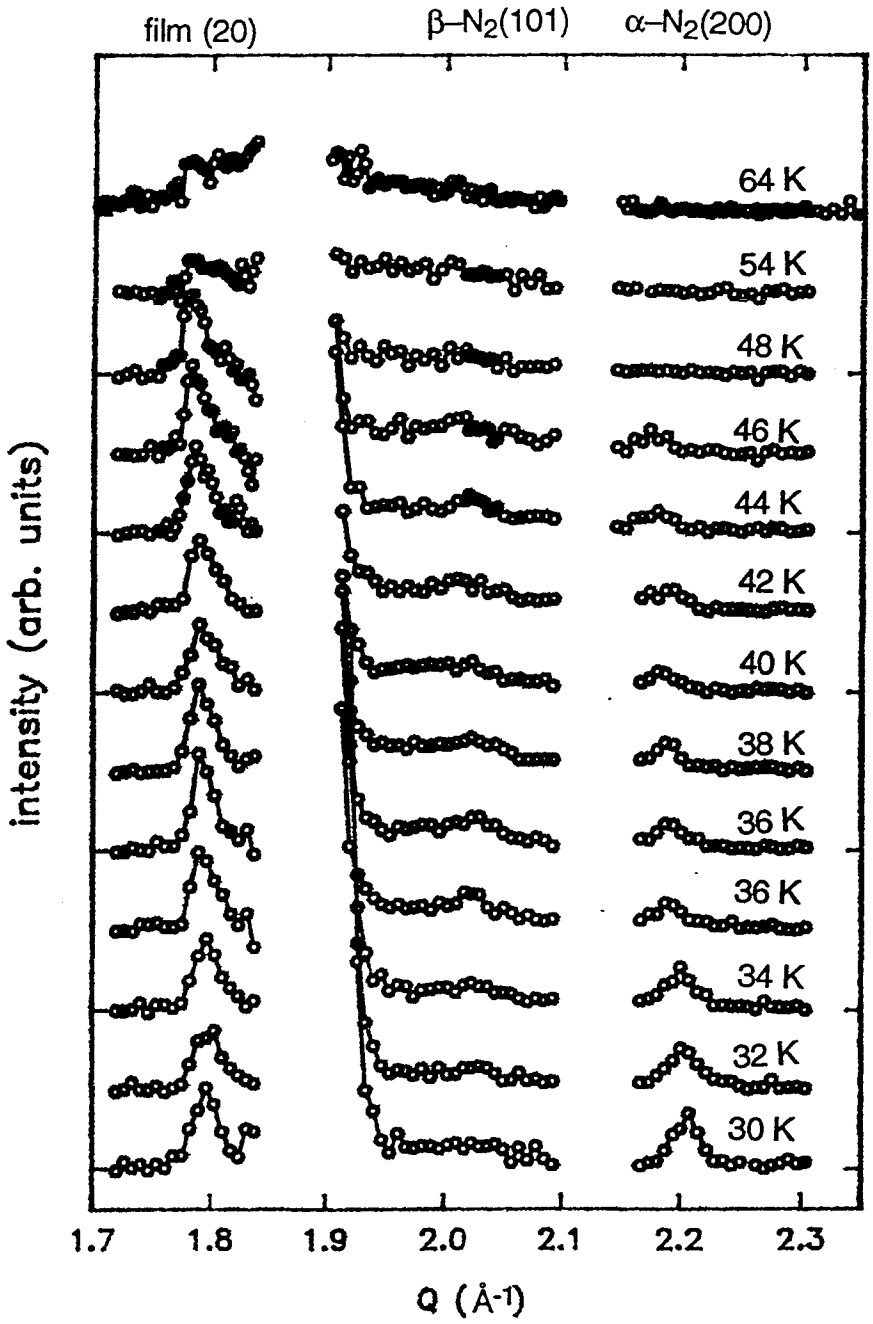

FIG. IV.2. Diffraction scans taken for T = 30 K to T = 64 K, when the temperature was monotonically increased. Diffraction peaks for the film (20), ß-N_2 (101), and α-N_2 (200) are indexed on the upper axis.

$q \approx 1.93$ Å^{-1} is associated with scattering from the strong α-N_2 (111) peak. Fig. IV.3 is a detail of Fig. IV.2, which more clearly shows behavior of the ß-N_2 (101), and the α-N_2 (200) peaks. Fig. IV.4 is a plot of the x-ray scans taken when T was monotonically decreased.

General trends can be identified in these scans. For the scans where the temperature is monotonically increased (Fig. IV.2), one sees a relatively constant film peak. The alpha peak is most intense in the low temperature scans, but disappears at higher temperature(Fig. IV.3). The beta peak first appears at temperatures above $T_{\alpha-ß}$, but also disappears at higher temperature (Fig. IV.3). For the scans where the temperature is monotonically decreased (Fig. IV.4), a gradual increase in the intensity of both the the N_2 (20) peak and the ß-N_2 (101) as the temperature drops to $T_{\alpha-ß}$ is observed. As the temperature drops below $T_{\alpha-ß}$, the beta phase peak drops in intensity and then disappears, as the alpha phase peak increases in intensity (Fig. IV.4). The film peak drops in intensity, but remains evident (Fig. IV.4). More quantitative conclusions follow after careful analysis of the integrated peak intensities.

3. Quantitative analysis

We monitor the integrated peak intensity for the selected peaks as a function of temperature. We sum the number of counts for each peak over the width of the peak. For the (20) peak, centered at 1.79 Å^{-1}, we sum over $q = 1.76$ Å^{-1} to 1.82 Å^{-1}. For the ß-N_2 (101) peak, we sum over $q = 1.98$ Å^{-1} to $q = 2.05$ Å^{-1} for the peak centered at 2.02 Å^{-1}

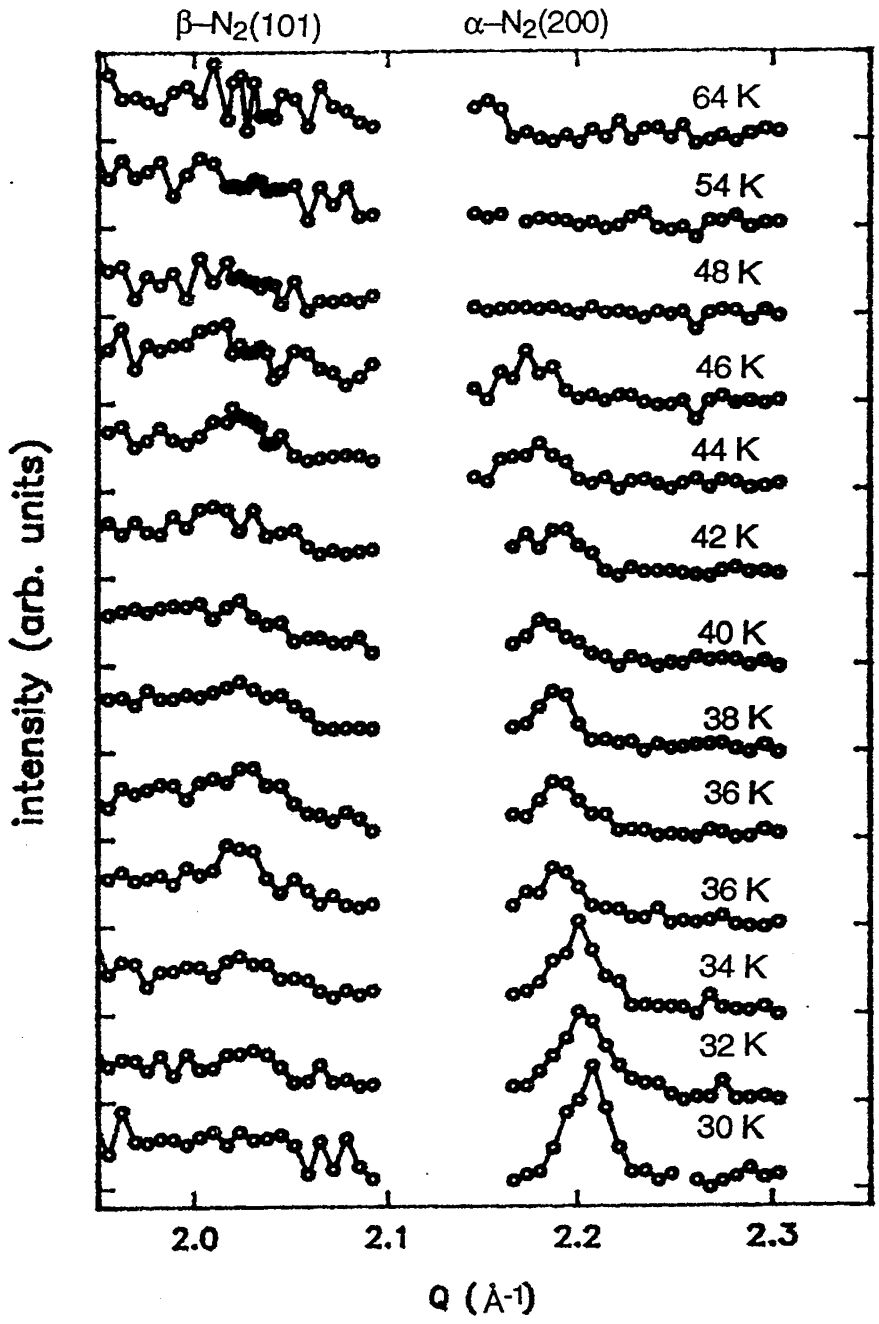

FIG. IV.3. Diffraction scans taken for T = 30 K to T = 64 K, when the temperature was monotonically increased. This is a high momentum transfer detail of Fig. 4.2. Diffraction peaks for ß-N_2 (101), and α-N_2 (200) are indexed on the upper axis.

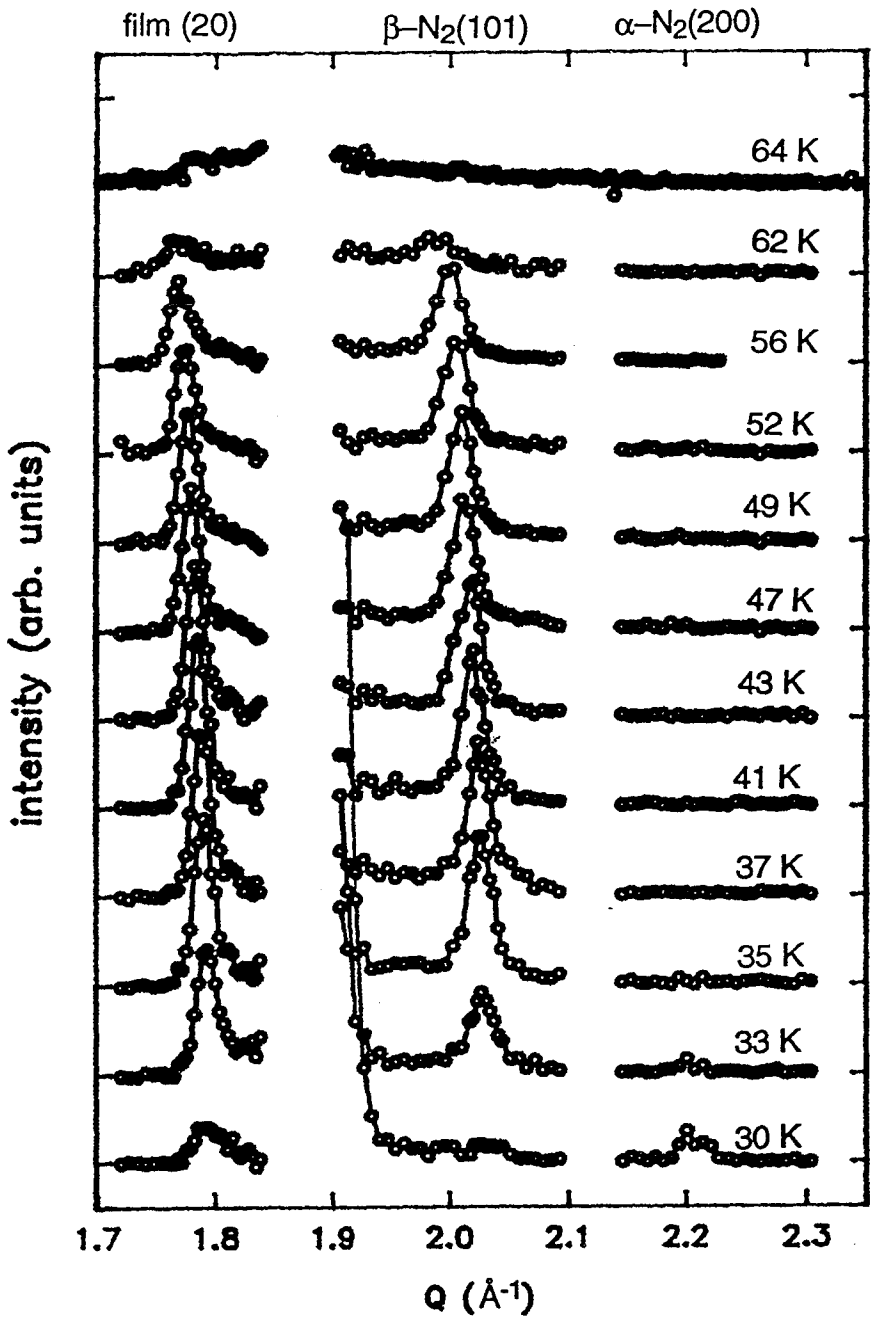

FIG. IV.4. Diffraction scans taken for T = 30 K to T = 64 K, when the temperature was monotonically decreased. Diffraction peaks for the film (20), ß-N_2 (101), and α-N_2 (200) are indexed on the upper axis.

and for the α-N_2 (200) peak we sum over q = 2.17 $Å^{-1}$ to q = 2.25 $Å^{-1}$ for the peak centered at 2.21 $Å^{-1}$. From this summed intensity we subtract out intensity associated with isotropic background scattering. This is calculated by taking the average of the number of counts in the background at the high and low momemtum transfer ends of each peak, and multiplying by the number of points in each peak. The remaining counts we call the integrated intensity.

A statistical error for each peak is calculated using the following method. The total error is given by:

$$\Delta I_{tot} = \sqrt{\Delta I_{peak}^2 + \Delta I_b^2 + \Delta I_{ib}^2}, \qquad \text{(IV.1)}$$

where $\Delta I_{peak} = \sqrt{I_{peak}}$ is the error in the peak intensity, $\Delta I_b = \sqrt{I_b}$ is the error in the background scan in the region of the peak, and ΔI_{ib} is the error in the isotropic background. The error in the peak intensity is the square root of the peak intensity times any normalization constants used for each scan. The error in the background is the square root of the sum of the background counts over the region that contains the peak times normalization constants. The isotropic background results after subtraction of the background from the adsorbed species scans. Hence, the error in the isotropic background is estimated to be the same as the error for the subtracted scan. The total error is then:

$$\Delta I_{tot} = \sqrt{2(mI_{peak} + nI_b)}, \qquad \text{(IV.2)}$$

where I_{peak} is the integrated peak intensity of the nitrogen peak, I_b is the intensity of the background in the peak region, and m and n are

normalization constants.

After quantitative analysis of the peak intensities (and associated errors), we plot the peak intensies versus temperature for the three monitored peaks. Figure IV.5 is a plot of the peak intensities as the temperature was monotonically increased. The intensity and width of the film peak [Fig. IV.5(c)] remains constant within error in the temperature range between 22 K and 48 K. At 54 K the peak has broadened 50% but the integrated intensity has remained approximately constant. By 64 K (just above T_{tp}), the (20) film has broadened to where it cannot be clearly distinguished from the background. This high temperature behavior of the (20) peak could be attributed to a loss of long range order in the monolayer or to film melting. A similar decrease in peak height and increase in width was observed previously for incommensurate compressed nitrogen films above 50 K for coverages $0.5 \leq \theta \leq 1.2$ ML and was attributed to a gradual decrease in long range order of the film.[65,96] Film melting for $0.5 \leq \theta \leq 1.2$ ML occurred in the range 60 K to 85 K, increasing with increasing coverage.[12,65,94] No structural information is available for melting at higher coverages.

Statistical uncertainty in the film peak is shown by the smaller error bars in Fig. IV.5(c). We estimate the systematic error due to contamination of the (20) peak by the ß (100) as the increase in the error bars in Fig. IV.5(c). This is based on the peak intensity of the measured ß (101) peak, and the theoretical relative intensities of these two peaks for an isotropic powder.[100] (Note: The relative

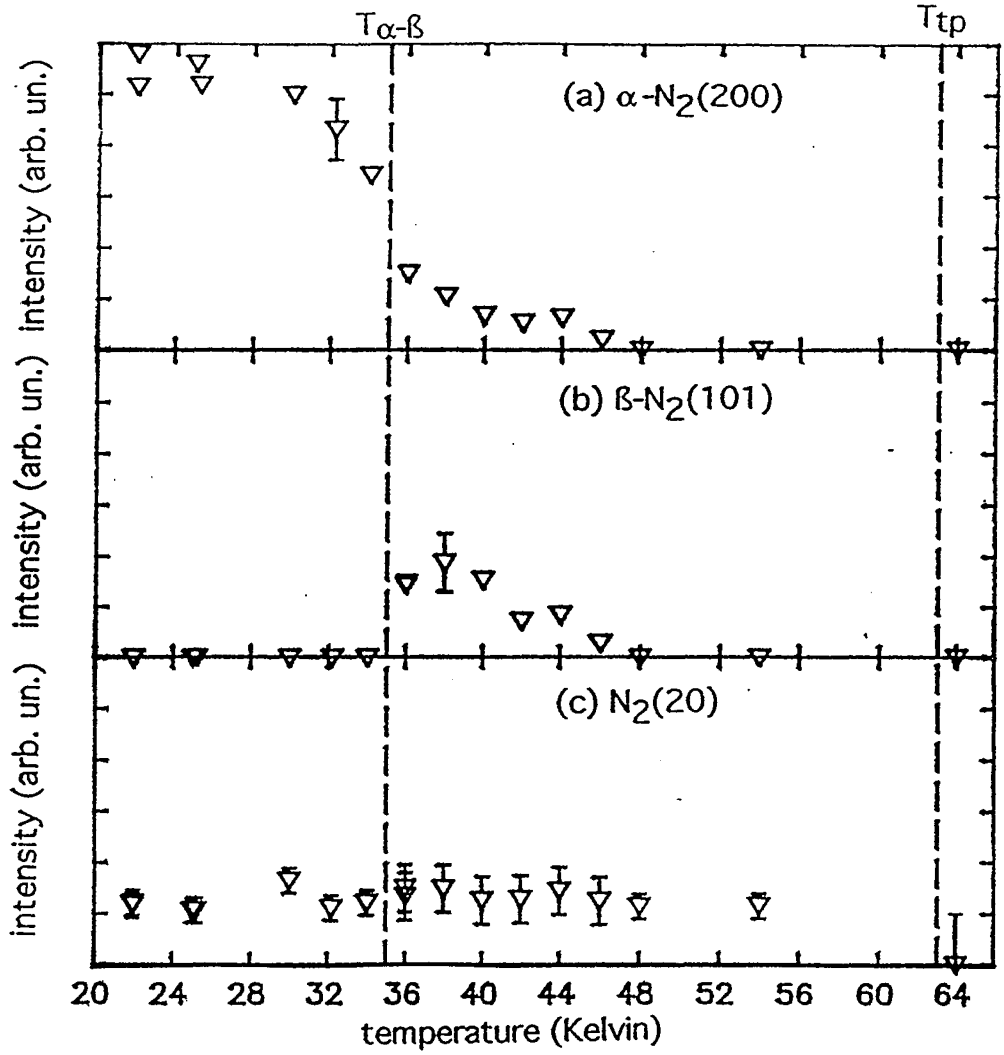

FIG. IV.5. Peak intensity as a function of increasing temperature: (a) α-N_2 (200) peak; (b) ß-N_2 (101) peak; (c) N_2 (20) film peak.

intensity of the two bulk peaks measured here may not exactly follow from those for an isotropic powder. Graphite foam samples can have some orientation, due to compression, and this may affect the relative peak intensities.) This additional uncertainty is small because the amount of ß-N_2 is always small in these scans, as discussed below.

The α-N_2 (200) peak intensity as a function of increasing temperature is plotted in Fig. IV.5(a). At temperatures below $T_{\alpha-ß}$ (22 K to 32 K) this peak is most intense and is constant within error. At 36 K (above $T_{\alpha-ß}$), the intensity drops by approximately half, and continues to drop monotonically as the temperature increases. At 48 K, the intensity of this peak has fallen to zero. This same behavior is also seen in the α-N_2 (211) peak; it is difficult to quantify, however, due to poorer statistics. We conclude all α-N_2 disappears by 48 K.

In Fig. IV.5(b) the intensity of the ß-N_2 (101) peak is plotted as a function of temperature. Below $T_{\alpha-ß}$, there is no evidence for ß nitrogen. As the temperature is increased above $T_{\alpha-ß}$, there is an abrupt increase in ß-N_2 peak intensity. The intensity then decreases monotonically as the temperature is increased. At 48 K, the intensity of this peak has dropped to zero. Thus all ß-N_2 disappears by 48 K.

Figure IV.6(a) shows the intensity of the α-N_2 (200) peak as the temperature was monotonically decreased from 64 K to 30 K. There is no α-N_2 present above $T_{\alpha-ß}$. The first evidence of this phase is at T = 33 K. At T = 30 K, this amount has increased substantially. This corresponds to the bulk nitrogen undergoing the α-ß phase transition.

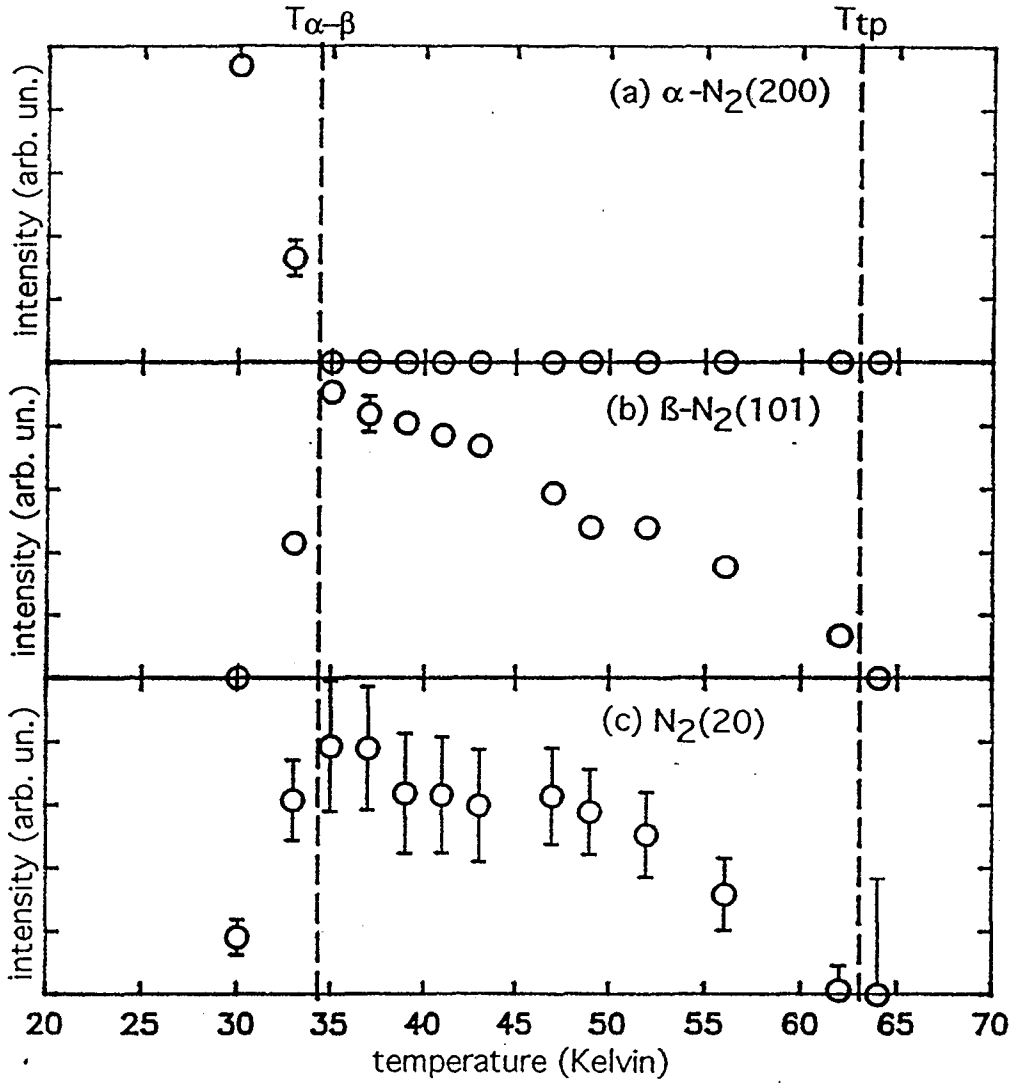

FIG. IV.6. Peak intensity as a function of decreasing temperature: (a) α-N_2 (200) peak; (b) ß-N_2 (101) peak; (c) N_2 (20) film peak.

Figure IV.6(b) is a plot of the ß-N_2 (101) peak intensity. For all scans between T_{tp} and $T_{\alpha-ß}$, ß-N_2 is observed. This contrasts to the situation where the temperature was monotonically increased; there all of the bulk material is gone above 48 K. As the temperature is decreased, the amount of bulk beta nitrogen increases, until $T_{\alpha-ß}$. Below $T_{\alpha-ß}$, the amount of beta nitrogen drops drastically, which corresponds to bulk material undergoing the α-ß phase transition. The ß-N_2 (101) also shifts to higher momentum transfer as the temperature decreases. This shift corresponds to an average linear coefficient ofthermal expansion of 2.2×10^{-3} Å/°C, in good agreement with previously published values.[28]

Comparison of Figs. IV.6(b) and IV.6(c) shows that the film peak intensity plot has similar temperature behavior to the ß-N_2 peak for montonically decreasing T. We first see evidence of a weak film peak at T = 62 K. The intensity of the film peak grows in the same manner as the ß-N_2. This continues until $T_{\alpha-ß}$, where the behavior for these two peak intensity plots diverges. At T = 33 K, the intensity of the film peak drops by less than that of the ß-N_2. At T = 30 K, the film peak has dropped intensity once again, but is still evident, while the ß-N_2 is absent. We interpret this data to imply that the intensity of the film peak has a large contribution from the ß-N_2 (100) peak. The estimated systematic error in the film peak due to ß-N_2 (100) contamination is shown by the larger error bars in Fig. IV.6(c). They were estimated in the same manner as discussed above in relation to Fig. IV.5(c). The error bars demonstrate contamination of the film

peak is more significant for decreasing temperatures.

4. Discussion of layering behavior

In order to compare our data more directly with Volkmann and Knorr's ellipsometry results,[23] we have plotted the total amounts of crystalline 3D solid (triangles) and 2D solid (circles) as a function of temperature in units of coverage (ML) in Fig. IV.7. This plot is constructed by following the phase diagram found in Ref. 94. From 23 K (the melting temperature of the second layer in the bilayer) to $T_{\alpha-\beta}$, there is one compressed monolayer of nitrogen (θ = 1.1 ML), 2.6 ML of 2D fluid or amorphous layers, and the remaining material (4.3 ML) existing as bulk α nitrogen. We then convert our intensity data to units of coverage by making the assumption that at 30 K the intensity of the film peak corresponds to 1.1 ML, and the intensity of the α-N_2 (200) peak corresponds to 4.3 ML of α-N_2. We do not expect any sharp diffraction peaks from the fluid or amorphous component. At 36 K (above $T_{\alpha-\beta}$) we expect to see 1.1 ML of 2D crystalline solidlayers, 4 ML of fluid or amorphous layers, and the remaining material in bulk. To normalize the amount of ß-N_2 at 36 K, we assume the difference between the total bulk (2.9 ML) and the amount of α-N_2 (1.5 ML) equals the amount of ß-N_2 (1.4 ML).[23] The stepwise line in Fig. IV.7 shows the amount of crystalline 3D solid as a function of temperature predicted for the layering behavior observed by Volkmann and Knorr.[23]

Figure IV.7 shows that the amount of crystalline 3D solid in our cell is constant (within error) below 32 K, begins decreasing around

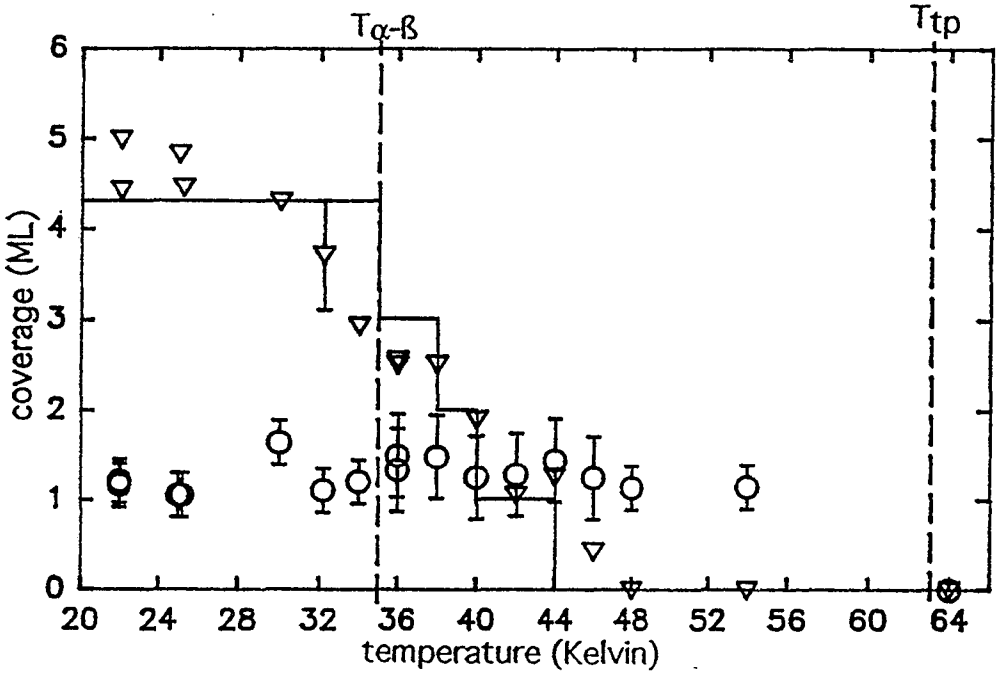

FIG. IV.7. Total amount of 2D (O) and 3D (v) crystalline solid. Normalization to obtain coverage units is described in the text. The stepwise curve is based on the prediction of layering transitions by Volkmann and Knorr, as discussed in the text.[23]

$T_{\alpha-\beta}$, and disappears entirely by 48 K (15 K below the ß-N_2 triple point at 63 K). A comparison of these results to those of Volkmann and Knorr [stepwise line in Fig. IV.7] shows that our data are consistent with the temperature range of their predicted layering transitions. However, our data are as consistent with a linear decrease in the amount of ordered 3D solid over this temperature range as they are with the predicted stepwise behavior. Therefore, we cannot confirm the predicted discrete layering transition temperatures. A linear trend in our data does not preclude layering. There could be several reasons for not observing stepwise behavior. First, the uncertainty in our data may prohibit observing steps [see Fig. IV.7]. The uncertainty in the number of layers is ± 0.6 ML, and therefore we may not be able to measure discrete layer changes as such. Further, due to the structural differences in the foam and HOPG substrates, pore size distributions and capillary effects may cause the layering transitions to occur over a finite temperature range instead of at a discrete temperature measured for HOPG substrates (this is discussed further below). The layering transitions also may not be abrupt because the film layers formed may not be complete, i.e., a complete layer may not form before the next layer begins to nucleate.

There is no corresponding increase in the amount of translationally ordered film evident in Fig. IV.7. Incomplete, amorphous layers above a crystalline monolayer have been observed previously at lower coverages.[12,65,94] From this, we infer that the bulk solid nitrogen is probably layering into a 2D amorphous solid or

fluid that does not contribute to the crystalline film peak intensity. However, one must be cautious when estimating the number of crystalline film layers from peak intensity; destructive interference between layers produces a very limited increase in the (20) integrated peak intensity from the nitrogen monolayer to the bilayer.[12,94] More definitive determination of the structure of the 2D layers would require lineshape analysis of well-defined 2D peaks. This necessitates long count rates and angular ranges, which would have prohibited the study of many temperatures. Given the scarcity of synchrotron x-ray beam time, we felt elucidation of the existence of layering was more important than the detailed structure of the 2D layers.

There are a number of possible alternate explanations for the disappearance of the bulk peaks, other than layering. These can be categorized as phenomena due to 1) migration of nitrogen from the scattering volume, 2) orientation effects causing the 3D bulk peaks to become unobservable, or 3) transitions to other 3D phases. For completeness, we discuss each of these alternatives below.

Nitrogen could migrate out of the x-ray scattering volume due to, for example, a spot on the cell walls or in the fill line which is at a lower temperature than the sample (a cold spot). Significant migration can be ruled out by monitoring the large (15%) attenuation of the graphite (002) peak due to x-ray absorption by the nitrogen in the cell. No marked changes were observed over the entire temperature range of our experiment. However, instabilities in the x-ray

intensity of the synchrotron source prohibit ruling out some small migration. Further, two scans at 36 K (immediately above $T_{\alpha-\beta}$) taken one hour apart show no change (< 2%) in any of the monitored bulk peaks [see Fig. IV.2]. Thus, we rule out large-scale nitrogen migration as the cause of the disappearance of the bulk peaks.

Specific peaks can change intensity, or disappear, due to changes of orientation of the crystallites. However, such orientational effects are minimized for powdered substrates. Also, for ß-nitrogen, randomly oriented bulk crystallites were observed in the ellipsometry experiments.[23] Further, we observe several peaks for both α and ß phases [α (200) and (211), and ß (100) and (101)] which exhibit the same temperature dependence of the intensity. This behavior clearly rules out orientational effects as an explanation of the disappearance of the bulk peaks in Fig. IV.5.

If the nitrogen remains in the scattering volume and is not in the α or ß phase above 48 K, there must be a transition to another 2D phase or to a 3D phase. Only the α and ß 3D solid phases exist below 4 kbar (nitrogen exhibits a γ phase at high pressure).[28,100] At the saturation vapor pressure of 3D liquid at our highest temperature, desorption of nitrogen into a 3D gas phase can contribute at most ≈0.1 ML in the sample cell dead volume. Transition to an equilibrium 3D liquid phase cannot occur below T_{tp} for increasing T. However, two effects associated with porous substrates, finite bulk particle size effects and capillary condensation in the substrate pores, are known to suppress the 3D melting temperature, leading to supercooled

metastable liquids.

Small 3D crystallites may exhibit large supercooling effects and have lower melting points than the large bulk samples. The change in the melting temperature, δT, is given by $\delta T/T_M = 2\sigma_{SL}/rL$, where T_M is the large sample melting temperature, σ_{SL} is the interfacial energy between the solid and liquid, r is the radius of a spherical particle, and L is the latent heat of fusion per volume.[101] This is similar to the temperature shift of $T_{\alpha-\beta}$ in small crystallites mentioned above. Chung and Dash have measured a 1.7 K depression in T_M attributed to finite size effects for multilayer nitrogen films adsorbed on Grafoil, with an estimated particle radius of 60 Å.[101] Based on diffraction peak widths (see App. A) for our data with increasing temperature, we estimate coherence lengths of 40-100 Å for the ß phase and >300 Å (resolution limited) for the α phase. These crystallite sizes correspond to temperature shifts of $\approx$ 0.3 K to 3 K. These estimates are much lower than the temperature shifts observed in our sample ($\approx$ 15 K).

The melting temperature can also be depressed by capillary condensation of the adsorbate material in a porous medium. The temperature shifts due to this effect are calculated from $\delta T/T_M = 2\sigma_{SL}\cos\theta/rL$, where θ is the contact angle between liquid-solid interface, and the pore wall.[102] We can estimate an upper bound on the temperature depression as $\delta T \leq 3$ K using $T_M = T_{tp}$, L=24.19 MJ m^{-3},[28] $r \geq 20$ Å (one-half of the smallest measured coherence length), and approximating $\cos\theta \approx 1$ and σ_{SL} as one tenth of the liquid-vapor

interfacial energy (σ_{LV} = 10.5 mJ-m^{-2})[103] as did Chung and Dash.[101] Again, this estimate is very much lower than the observed transition temperature in our substrate. Indeed, a δT of 15 K would correspond to a pore size of $\approx$ 4 Å. This is unreasonably small (it is about the size of a single N_2 molecule).

Therefore, finite size effects or capillary condensation cannot reasonably explain the decrease in crystalline bulk intensity for temperatures $\approx$15 K to $\approx$28 K below T_{tp} (we treat these effects in further detail in Sec. F). We conclude that our data indicate the layering of the bulk material into 2D liquid or amorphous material.

5. Discussion of hysteresis

Comparison of Figs. IV.5 and IV.6 shows that there is significantly different behavior in the system where the temperature was monotonically increased and where the temperature was monotonically decreased. As the temperature is decreased from above T_{tp}, one sees a bulk nucleation at temperatures just below T_{tp}. This bulk remains evident at all lower temperatures. In the series of scans where the temperature was monotonically increased, the bulk material was evident at low temperatures, but disappears by T = 48 K.

This hysteresis implies that growth mode is important in this system, as has been found for studies of bulk nitrogen crystal growth near $T_{\alpha-\beta}$.[28] Indeed, it is found that single crystal ß-phase nitrogen will shatter as it passes through the α-ß phase transition. Single crystal α-phase nitrogen can be produced if nitrogen is allowed to

nucleate at temperatures below $T_{\alpha-\beta}$. The shattering of the single crystal ß sample probably results because the α-ß phase transition is of the martensitic type, involving a change in stacking from AB (cubic) to ABC (hexagonal). Temperature-dependent hysteresis is not observed in the ellipsometry experiments because the coverage was varied while the temperature was held constant.[23]

We see an α-ß coexistence for increasing T over a 14 K temperature range which is not seen in the ellipsometry experiments. We attribute the coexistence to a difference in experimental technique. In the ellipsometry experiment, the temperature was fixed, and the coverage was varied. Therefore, bulk nitrogen would condense in the phase which was appropriate to the fixed temperature. We fixed the coverage (approximately), and varied the temperature from below $T_{\alpha-\beta}$ to above. This mode of experiment may allow a metastable state to exist, where the bulk nitrogen does not fully undergo the α-ß transition. Such coexistence is not surprising because the α-ß transition is a martensitic type, as discussed above. Bulk nitrogen samples also show hysteresis through the α-ß transition, which is not well understood.[28] Some measurements imply that 10 h or more are needed to completely make the α-ß transition for large bulk samples.[28] We measured scans exhibiting coexsistence over an 8 h time period, consistent with earlier measurements.

E. Phase diagram of nitrogen on graphite

We interpret our data for the scans where the temperature was

monotonically increased to be indicative of layering transitions, beginning near $T_{\alpha-\beta}$ and completing at $\leq$ 48 K, as evidenced by the disappearance of the bulk peaks. Also, we do not see an increase in the amount of translationally ordered 2D film. This suggests that any two-dimensional layers grown are disordered or fluid layers.

In order to consistently compare our results to previous multilayer N_2 on graphite studies, our results, the results of Volkmann and Knorr,[23] and other previous work[12,65,94,95,97] are integrated into a new, proposed multilayer phase diagram (Fig. IV.8). The proposed phase diagram extends the one found in Ref. 94 from coverages above 5 ML to 10 ML, and from temperatures above 38 K to 70 K. It is largely synthesized from the combined results of the previous studies cited. Our results prove to be consistent with previous work, as discussed below.

It is proposed that above 24 K, one ordered layer and amorphous or fluid film coexist;[12,94] above 3.7 ML, these may coexist with epitaxial bulk solid.[23,94] At coverages greater than 3.7 ML and temperatures ranging from just below $T_{\alpha-\beta}$ and above, the nitrogen on graphite system undergoes a series of layering transitions.[23] At temperatures just below $T_{\alpha-\beta}$, there is one compressed monolayer of nitrogen solid, several amorphous or liquid film layers, and α-N_2 condensate.[93,94] As the temperature is increased above $T_{\alpha-\beta}$, the number of film layers increases to five.[23] As the temperature is increased further, the system undergoes further layering transitions until all the nitrogen in the system exists as a compressed crystalline 2D solid

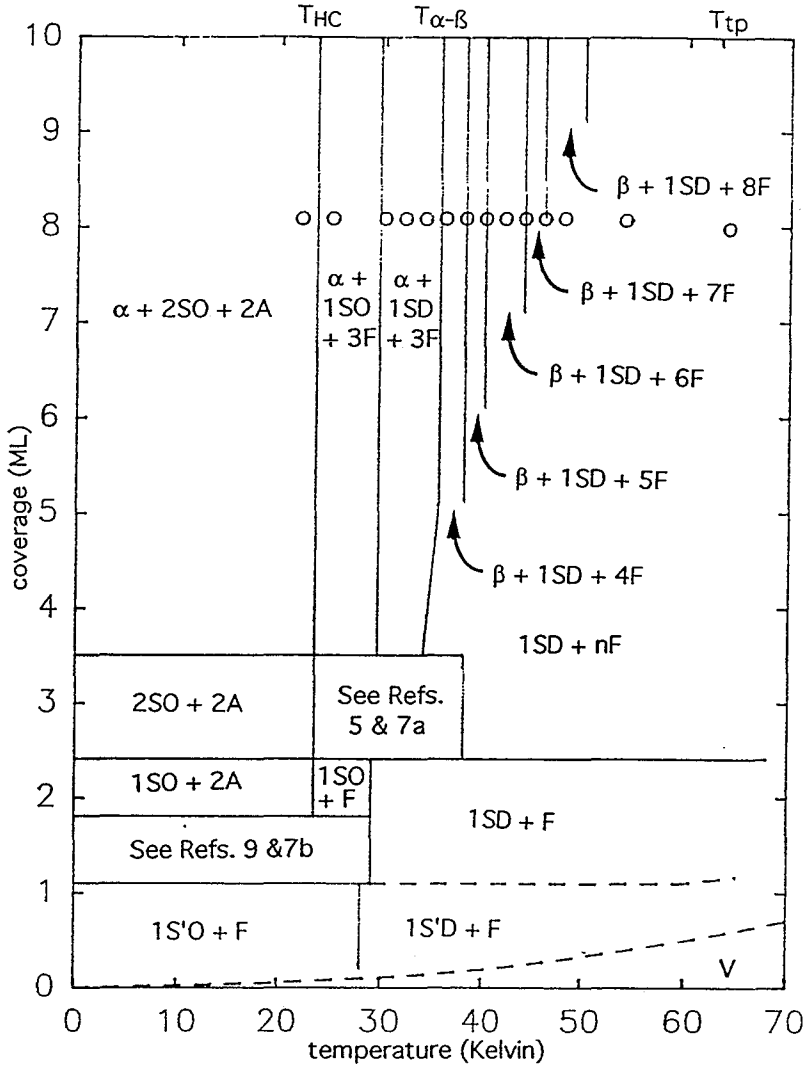

FIG. IV.8. Proposed phase diagram of nitrogen physisorbed on the graphite basal plane summarizing this and previous work.[12,23,63,94,95] The notation follows Wang *et al.*[94] 1S, 1S', and 2S denote the fully compressed monolayer solid (TI) phase, expanded monolayer solid phase, and bilayer solid phase, respectively. α, ß, A, and F denote the α-N_2 bulk phase, ß-N_2 bulk phase, amorphous or disordered 2D film, and 2D fluid, respectively. The numerical prefix indicates the number of completed or partially completed layers of that phase. O and D indicate orientationally ordered and disordered phases, respectively. The circles (O) correspond to our diffraction scans. The reader is referred to other articles for details of the complicated phase diagrams proposed for low temperature monolayer formation,[12,95] and melting of the second layer.[94,95] T_{HC} (indexed on the upper axis) is the temperature at which a peak in heat capacity scans[95] is observed; the origin of this peak is in dispute.[94,95] $T_{\alpha-\beta}$ and T_{tp} are the bulk α-ß transtition, and triple point temperatures, respectively.

film monolayer and as 2D amorphous or liquid film layers.[23] This solid monolayer begins to lose long-range order in the 50 K to 65 K range, from submonolayer coverage up to at least 8 ML.[12,65,94,96] From submonolayer coverage to ≈1.2 ML melting of the solid monolayer increases from ≈60 K to 85 K.[12,65,97] Above 1.2 ML the melting temperature of the film has not been determined.

This phase diagram shows a very complex behavior. Incomplete wetting below $T_{\alpha-\beta}$ is not expected for this system; the lattice constants for the 2D layer and for the 3D α-N_2 (111) cleavage plane differed by ~1%,[23] leading to very little frustration between the 2D layer and the 3D bulk phase. However, neutron studies showed that the 2D layer is slightly distorted from the hexagonal symmetry of the α-N_2 (111) plane.[94] This leads to a discontinuity in growth. Epitaxial α-N_2 nucleates, as measured in the ellipsometry studies. One or two layers of amorphous material would allow for lattice mismatch, and promote subsequent epitaxial growth. Orientational effects may also play a part here. The N_2 monolayer has herringbone orientational ordering,[12] while the α-N_2 (111) cleavage planes are pinwheel in orientation.[28] The amorphous material would allow for this difference also.

The high temperature behavior (above $T_{\alpha-\beta}$) of N_2 is even more difficult to motivate. Above $T_{\alpha-\beta}$, bulk nitrogen becomes an orientationally disordered hcp crystal. There does not appear to be any reason then that nitrogen should not be behave similarly to the rare gasses, which are thought to wet graphite.[10] One possible

explanation, offered by Volkmann and Knorr, is that perhaps some direction other than the [001] is preferred for crystal growth.[23] Then bulk growth would proceed in facets in this preferred direction rather than the [001] direction. This would prohibit N_2 from completely wetting the graphite substrate.

The asymmetry of the N_2 molecule leads to interesting phenomena, such as the layering transition driven by the bulk α-ß phase transition. Layering transitions driven by bulk structural transitions (other than triple point wetting) would not be expected for spherically symmetric rare gas systems. This experimental evidence should provide clues important to computer simulations of this system, and add to our fundamental understanding of multilayer systems.

Future work might include study of multilayers of other symmetric molecules. Natural systems include O_2 on graphite or CO on graphite. Oxygen is also an ellipsoid like N_2, and it has three low temperature structural phase transitions, α phase below 23.9 K, ß phase between 23.9 and 43.8 K, and a γ phase between 43.8 K and 54.36 K [$T_{tp}(O_2)$].[10] This system exhibits a 2D rich phase diagram. For low temperatures [below $T_{\alpha-\beta}(O_2)$], the system is incompletely wet with up to six solid layers forming. As the temperature is increased, the system undergoes layer melting. The transition temperatures for this system do not seem tied to the bulk transitions, in contrast to N_2 on graphite.[10]

CO adsorbed on graphite is another potentially interesting

system. CO is isoelectric to N_2, and has similar bulk crystal structure in both the α and ß phase as N_2. CO also exhibits a structural α-ß phase transition. CO adsorbed to graphite has the same low temperature 2D crystal structure as N_2; additionally, at very low T (5 K) the CO monolayer is seen to dipole order (discussed in Sec. II.G). At low temperature, the system is seen to incompletely wet graphite, with only one layer forming. Layering transitions occur for this system. Irregular variations of the layering critical temperatures are measured by adsorption isotherms, with $T_{2,c}$ = 59.7 K, $T_{3,c}$ = 58.7 K, and $T_{4,c} = T_{5,c}$ = 65 K.[10] None of these seems tied to $T_{\alpha ß}(CO)$ = 61.6 K.[10] Understanding of this system would definitely benefit with structural measurements of multilayer structural behavior, particularly the irregular variations in the layering transition temperatures.

Comparison of our N_2 results to the multilayer transitions of O_2 and CO raises several questions. All three systems exhibit 3D structural phase transitions, but only N_2 is observed to have 2D phase transitions associated with its 3D phase change. Neither O_2 or N_2 has a dipole moment, while CO does (see Chap. 1, Sec. C.1); all three have quadrupole moments ($q(O_2) = 1.3 \times 10^{-40}$ C m^2; $q(N_2) = 4.7 \times 10^{-40}$ C m^2; $q(CO) = 8.3 \times 10^{-40}$ C m^2); oxygen is paramagnetic. It is possible that the additional steric interactions for CO and the paramagnetic properties for O_2 cause the more complicated layering behavior and cause the 2D systems to be unaffected by the 3D orientational ordering phase.

Let us briefly revisit triple point wetting. For this wetting transition the loss of translational symmetry alleviates strain between the 2D layers and the 3D crystal structure. For layering transitions which are tied to bulk orientational order-disorder transitions to occur, we may look for a similar loss of 3D symmetry to favor layer growth. It is not apparent from this or previous studies what particular aspect of the α-ß nitrogen transition facilitates layer growth (see discussion above). Detailed comparison of this system to both CO and O_2 on graphite may elucidate this point. Certainly observation of a system which exhibits a similar 2D phase transition driven by a 3D orientational phase transition would be helpful.

This is interesting data for the theoretician; a careful study of the relative importance of the intermolecular forces (i.e., the van der Waals forces) as well as electric and magnetic forces could lead to better understanding of crystal structure and phase transitons in 2D multilayers. In particular, examination of such forces as asymmetric steric, electric, and dispersion forces would be elucidating.

F. Capillary effects in multilayer adsorption systems

As detailed above (see Sec. A), one potentially important difference between our powder diffraction studies and the ellipsometry experiments is the substrate. Exfoliated graphite substrates have a pore structure which may affect high coverage studies, such as

multilayer adsorption work. This is particularly important in studies where accurate temperature measurement is desired, such as layering transition, surface roughening, or surface melting studies. As discussed briefly above (Sec. D.4), capillary condensation in the porous substrate can cloud interpretation of the temperature behavior of adsorbed systems. Indeed, careful analysis of possible effects of capillary behavior in the N_2 on graphite system is warranted, due to the pore structure of our graphite substrate.

In this section, we intend to quantify these very general statements. We begin by describing how capillarity arises, and detailing the effects on adsorbed species. We then apply our knowledge to the N_2 on graphite system, quantifying the possible effects it has on interpretation of our layering data.

1. Capillary condensation in porous samples

Pore structure can be found in most powdered substrates. Pores arise in the interstices of the substrate particles.[1] For example, for a substrate which is made up of spherical particles, pores exist in the space between the packed spheres. For exfoliated graphite samples, the pore structure exists in the space between the graphite flakes.

The pores are classified in the following way: Micropores are those with a radius of ~20 Å; mesopores have radii of 20 Å to ~200 Å, and macropores have a radius greater than 200 Å. These ranges are rather broad; however, they are determined more by their effect on

adsorption than by size.[1] Micropores cause very restricted motion and have very complicated thermodynamic effects.[1] We do not consider here any systems which have been observed to have micropores. Graphite foam samples generally fall into the category of mesopores, with pores sizes of about 40 Å to 60 Å.[104]

A qualitative picture of adsorption on porous material is shown in Figure IV.9. Consider an adsorption-desorption isotherm. We start with a clean substrate and begin adsorbing gas [Fig. IV.9(a)]. Initially, the gas will adsorb on the free surfaces and inside the pore in the same manner [Fig. IV.9(b)]. Eventually enough material will adsorb to block the pore [Fig. IV.9(c) & (d)]. We then begin to desorb gas. Initially, gas will desorb from the meniscus of the material in the pore [Fig. IV.9(e)], and eventually the meniscus will break, bringing us back to our original state [Fig. IV.9(a)]. For adsorption and desorption, different thermodynamic paths are followed.[105] The point at which the hysteresis loop opens up is where capillary condensation begins. At this point, the smallest pores will be blocked on adsorption, and the largest pores will empty on the desorption branch.

The adsorption branch of the isotherm generally occurs at a higher pressure. A simple thermodynamic picture proves this. The free energy of the system is a function of the total surface tension in the system, as well as of temperature, pressure, and chemical potential. For the adsorption branch, where the material is adsorbed to the pore walls, the surface area of the adsorbate is greater than

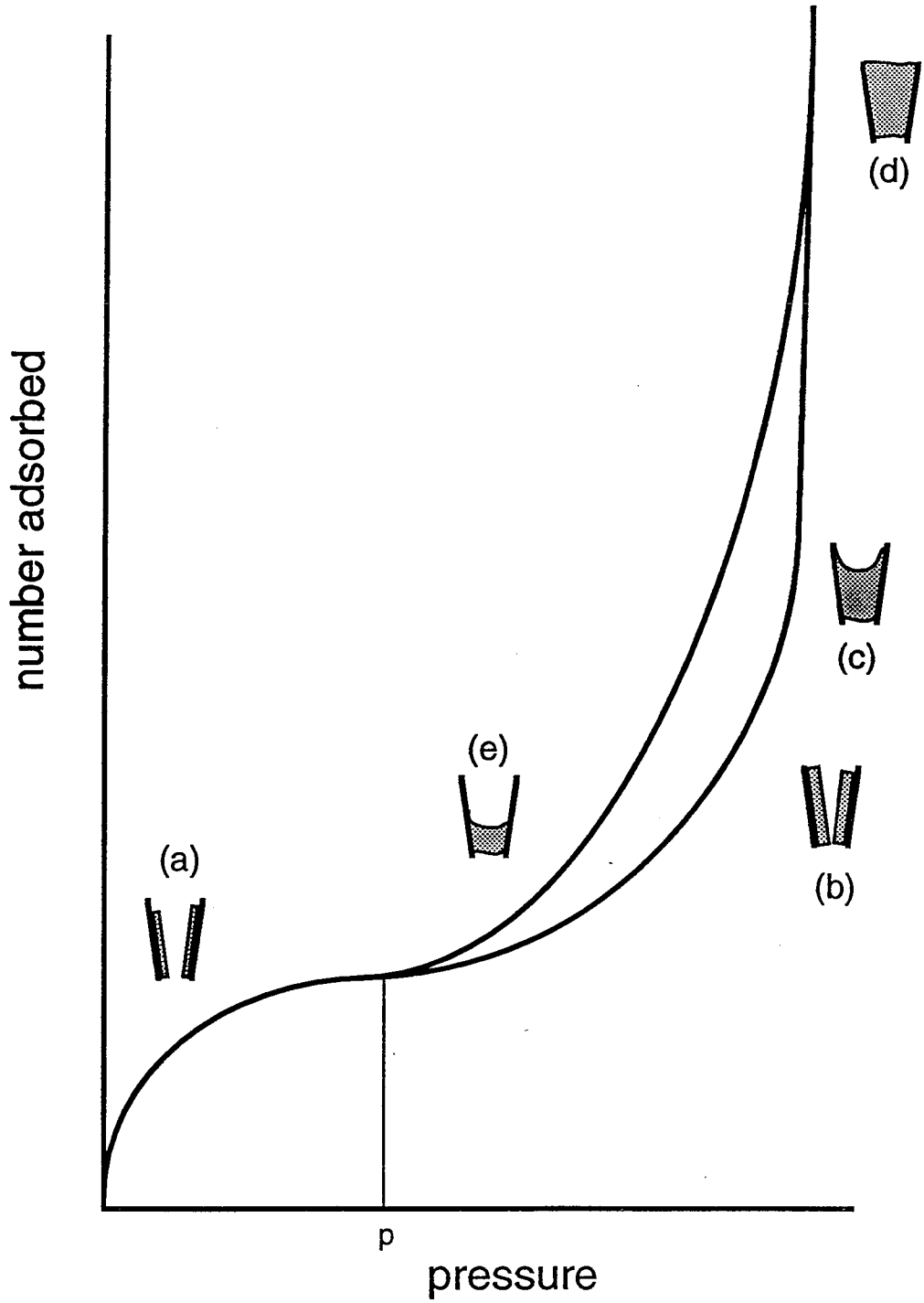

FIG. IV.9. Schematic representation of a multilayer adsorption and desorption isotherm. Labels are described in the text.

that for the desorption branch, where the material is condensed in the meniscus. This increased surface area leads to a higher surface energy, and to a higher pressure. Because the desorption branch has a lower pressure, it is thought to be the true equilibrium path.

By considering the effect of the surface tensions in the system, one can prove that for a substrate with pores of radius r condensation in the pore will occur at a lower pressure than the saturation vapor pressure for the adsorbate. The pressure is given by:

$$\ln\left(\frac{p}{p_o}\right) = \frac{-2V\gamma_{LV}\cos(\phi)}{rRT}, \qquad \text{(IV.3)}$$

where p is the pressure at which the condensation takes place, p_o is the adsorbate saturation vapor pressure at the isotherm temperature, V is the molar volume of the adsorbate, γ_{LV} is the liquid-vapor surface tension, ϕ is the contact angle between the liquid and the pore wall, and R is the gas constant. [See Gregg and Sing (Ref. 1) for development.]

For a porous substrate, a hysteresis loop will be evident in an adsorption-desorption isotherm.[1,105] This occurs because on the adsorption branch, the vapor pressure will be higher for the same number of particles adsorbed than on the desorption branch. This can lead to an overestimation of the amount of material adsorbed in layers. The measured number of particles or amount adsorbed on the adsorption branch corresponds to material adsorbed both in layers and capillary condensed.

We can also use an adsorption-desorption isotherm to measure the

pore size distribution of a porous sample. Eq. (IV.3) is solved for the radius. We assume that at pressure p measured in the desorption branch of the isotherm pores of radius r empty. The radius r is calculated from Eq. (IV.3), using p, as well as the other physical parameters for the system (e.g., the temperature, the molar volume, etc.). The calculated radius must be corrected, however, for the thickness of the material still adsorbed to the pore wall [compare Fig. IV.9 (a) and (e)]. This is estimated by comparing the isotherm on the porous material to an isotherm of the same material which does not exhibit a hysteresis loop (for a complete development, see Ref. 1, Chapter 3). For example, a multilayer isotherm of exfoliated graphite exhibits a hysteresis loop, while an isotherm on carbon black has no hysteresis loop. Comparison of the two yields information about how much material is layered and how much is capillary condensed.[1,104]

Alternatively, consider what happens in a system exhibiting capillary condensation when the pressure is held constant and the temperature is allowed to vary. In this case, the transition temperature for a phase change of the adsorbed species can be shifted for material adsorbed in pores. This temperature shift is given by:

$$\delta T = T_o - T = \frac{2VT_o}{h_f}(\gamma_{sw} - \gamma_{lw}), \qquad \text{(IV.4)}$$

where T_o is the bulk transition temperature, T is the transition temperature of the capillary condensed material, h_f is the heat of fusion, γ_{sw} is the solid-substrate interfacial energy, and γ_{lw} is the liquid-substrate interfacial energy.[1] In studies like our layering

experiments, we are primarily interested in temperature shifts of transitions such as these.

Indeed, transition temperature shifts have been measured experimentally for several similar systems. Lysek *et al.* found shifts of 3-4 K for the melting transition of supercooled bulk methane capillary condensed on graphite foam.[106] The melting temperature of nitrogen on a Vycor substrate ($r \approx 20$ Å) was depressed by 3-5 K.[107] Tell and Maris found $\delta T \approx 2$ K for the melting transitions of H_2, D_2, and Ne capillary condensed on Vycor substrates (≈27 Å average pore radius) as the temperature was raised from well below T_{tp}; by contrast, $\delta T \approx 4$ K due to supercooling from above T_{tp} for the same systems.[108] In a study of supercooled oxygen, Awschalom *et al.* found freezing point temperature depressions of 3 K for 188 Å pores to 10 K for 22 Å pores. Indeed, for application to our layering studies, we vary the temperature for an fixed amount of material, and so it is temperature shifts of this type are the most likely capillary effects.

2. Capillary effects in multilayer N_2 on graphite

We now understand how capillary effects can alter the multilayer characteristics of adsorption systems on porous substrates. We intend to quantify these effects, and to determine if capillary effects are significant to the interpretation of the layering transitions we observed.

A recent study by Morishige *et al.* probed the effects of capillary condensation on the adsorption of Kr, Xe, and N_2 on

different graphite substrates. The experiments measured adsorption and desorption isotherms and x-ray diffraction scans for the adsorbates on two graphite samples.[104] The first sample was a lightly compressed exfoliated graphite sample with a density of 0.12 g cm^{-3}. The second sample was a Grafoil sample with a density of approximately 1 g cm^{-3}. Our graphite foam sample has a density of 0.24 g cm^{-3}, and is expected then to behave more similarly to the lightly compressed sample used by Morishige *et al.*

Kr adsorption isotherms measured by Morishige *et al.* showed that the lower density sample had sharper layer adsorption steps.[104] Four layers were observed for the lower density sample, where only three were measured for Grafoil. They inferred that the low density sample was more homogeneous, with fewer pores, than the Grafoil sample. Multilayer Xe isotherms in adsorption and desorption mode exhibited hysteresis loops for both samples which closed at just over 1 layer. X-ray diffraction scans of Xe on both samples exhibited bulk material at 3 layers (incomplete wetting) for both samples at 107 K, while an x-ray diffraction scan of Xe on the lower density graphite exhibited bulk material at 2 layers at 32 K. This would not be expected for Xe on a single crystal substrate, as Xe completely wets graphite.[10]

Adsorption and desorption isotherms of N_2 (at 77 K) were used by Morishige *et al.* to quantify the amount of material capillary condensed for both substrates. Hysteresis loops were measured for both substrates. The hysteresis loop for the lower density sample was smaller. In order to quantify the amount of material capillary

condensed, Morishige *et al.* compared the amount of material adsorbed to their samples to the amount of nitrogen adsorbed in an isotherm measured on carbon black, which does not exhibit a hysteresis loop. From this analysis, they conclude that the amount of nitrogen capillary condensed at the highest coverage they measured (7 ML) was 15% of the total adsorbed amount for the lightly compressed sample and 43% for the Grafoil sample. From these isotherms, Morishige *et al.* calculated a pore size distribution for the low density sample of 40 to 60 Å using the method described in the previous section.[104]

This multilayer N_2 isotherm work is very important to understanding what we observe in our x-ray measurements. Comparing the density of our sample to those studied by Morishige, we conclude our sample is most like the low density sample. Our sample therefore most likely has a pore size distribution of 40 to 60 Å, corresponding to a δT of 1 to 1.5 K, for phase transition temperature shifts. We also conclude that at 8 ML at 77 K, 15% to 20% of the material adsorbed to our foam sample would be capillary condensed liquid.

Let us assume 15% to 20% of our nitrogen at $T < 63$ K was capillary condensed bulk solid. This would correspond to 1.2 to 1.6 ML of bulk material still existing above 48 K until approximately 1-1.5 K below the nitrogen triple point temperature, where melting of this capillary condensed solid would occur. One possible reason that we do not observe any bulk peaks at temperatures higher than 48 K may be due to experimental resolution. The error in coverage for the bulk peaks is 0.6 ML; our smallest resolvable bulk peak corresponds to 0.3 ML.

Bulk nitrogen peaks which correspond to 1.2 to 1.6 ML should be resolvable. Possibly, the bulk nitrogen exists in either α- or ß-phase, as we observe coexistence over a large temperature range. Assuming equal parts α- and ß-N_2, peaks corresponding to 0.6 to 0.8 ML may be expected for each phase. These amounts are comparable to our error in coverage, but larger than our smallest measured peak, and should be measurable. We conclude we do not have 15%-20% of our material capillary condensed as solid. We cannot rule having about 3% or less of our total nitrogen capillary condensed as solid, as this corresponds to the smallest resolvable peak in this study.

This conclusion is consistent with the measured coherence lengths for the bulk N_2 phases. For increasing T scans, the coherence lengths of the α and ß peaks are >300 Å (resolution limited) and 40-100 Å, respectively, and for decreasing T both the α and ß peaks have coherence lengths >300 Å. The pore size distributions typical for graphite foams are estimated to be 40-60 Å.[104] This suggests that the α- and ß-N_2 observed is not all capillary condensed solid.

It may be possible that different sample preparation causes different capillary behavior, leading to considerably less than 15% of the nitrogen capillary condensed in our samples. While our graphite sample is a compressed exfoliated graphite similar to the one studied by Morishige *et al.*, it may have been prepared in such a way as to minimize capillarity. For example, Morshige *et al.* baked their samples at moderate temperatures (350°C for 12 h), while we baked ours at considerably higher temperatures (1000°C for 48 h). Normally,

graphitization takes place at a considerably higher temperature (1300-1500°C);[109] however, amorphous carbon undergoes structural changes in the temperature range of 500-950°C.[109,110] Perhaps some structural annealing mechanism in porous substrates is actuated in this temperature range. This analysis is, of course, pure speculation, and experimentation would be needed to prove this.

As discussed above (see Sec. IV.C) capillary condensation could reasonably cause a temperature depression of the melting T of bulk nitrogen on the order of 1-1.5 K, for a sample with a pore size distribution like those studied here. Temperature depressions of 15 K would require bulk patricle size or pore size of approximately 4 Å, which is much smaller than the pore size observed on similar samples (in fact, it is very close to the size of a single nitrogen molecule). We conclude that we are not measuring melting temperature depression due to capillary condensation of bulk material.

Recall the temperature hysteresis we observed in our x-ray experiments (see Sec. IV.C). The nature of this hysteresis tends to rule out capillary effects as the reason for the disappearance of our bulk peaks in the increasing temperature scans. The temperature depression of a transition when cooling is generally considerably more than the depression in transition temperature when warming for all similar types of transitions affected by capillary condensation,[107,108] in contradiction to our results. If capillary condensation were responsible for the disappearance of the peaks, we would then not expect bulk peaks to appear on the decreasing T scans until a

temperature lower than 48 K, where our increasing T bulk peaks disappear. Additional structural studies of multilayer films on HOPG would be useful in clarifying whether our use of a foam substrate affected this hysteresis.

Let us carefully consider the thermodynamic implications of our results. The thermodynamics of liquid films on porous substrates are well understood; indeed, Eqs. (IV.3) and (IV.4) are used to describe isothermal adsorption and 3D liquid-solid transitions, respectively, in porous substrates. The thermodynamic behavior of solid films is not as clearly understood. One reason for this is because solid surface tensions are not known[10] and this complicates comparison of theory to experiment. This is true even for simple spherically symmetric rare gas adsorbates. While there is evidence for solid capillary material in some systems (e.g., Xe on graphite)[104] there is no comprehensive theory which predicts under what conditions this solid capillary condensed material will be observed.

Recall that thermodynamically, at a given pressure, temperature, and volume, the Gibbs free energy function is always minimized by the existing phases. For example, if a bulk sample at some pressure, temperature, and volume is liquid, we can infer that the free energy of the liquid is less than that of the solid (or gas) under the same conditions. From this property of the Gibbs free energy, we can infer information about the relative free energies of several systems important to our studies here. For example, for liquid adsorbate layers on porous substrates, the free energy of the system is lowered

if liquid condenses in the pores rather than on free surfaces. From this, Eq. (IV.3) is derived. For bulk material capillary condensed just below T_{tp} the minimum free energy of the system is maintained if the capillary condensed material melts at a slightly depressed temperature compared to the bulk melting temperature. Layering in a 2D system occurs when the free energy of n+1 layers is lower than the free energy of n layers plus bulk material.

If we apply the rule that the free energy is always a minimum, we can infer that our experiments indicate that for N_2 on graphite, below T_{tp}, the free energy of n+1 ML 2D adsorbed layers is less than the free energy of n ML 2D layers plus 1 ML 3D solid or 3D capillary condensed solid material. Capillary condensation of 3D bulk solid does not perclude layering; indeed, as is evident from experiment, layering does occur. Currently, this result is not in conflict with any physical theory. The thermodynamics of capillary condensed solid material need careful consideration. Theoretical work on a description of systems such as N_2 on graphite, as well as experimental determination of surface forces, is necessary.

We do expect that capillary effects smear out the discrete layering transitions observed by ellipsometry isotherms. Indeed, according to the above analysis, shifts in the transition temperature with a range of about 1-1.5 K is expected for phase transitions on this sample. Figure IV.10 is a plot of the total amount (α plus ß) of bulk solid expected according to the previous ellipsometry studies (solid line)[23] and the total bulk measured in our experiments (∇).

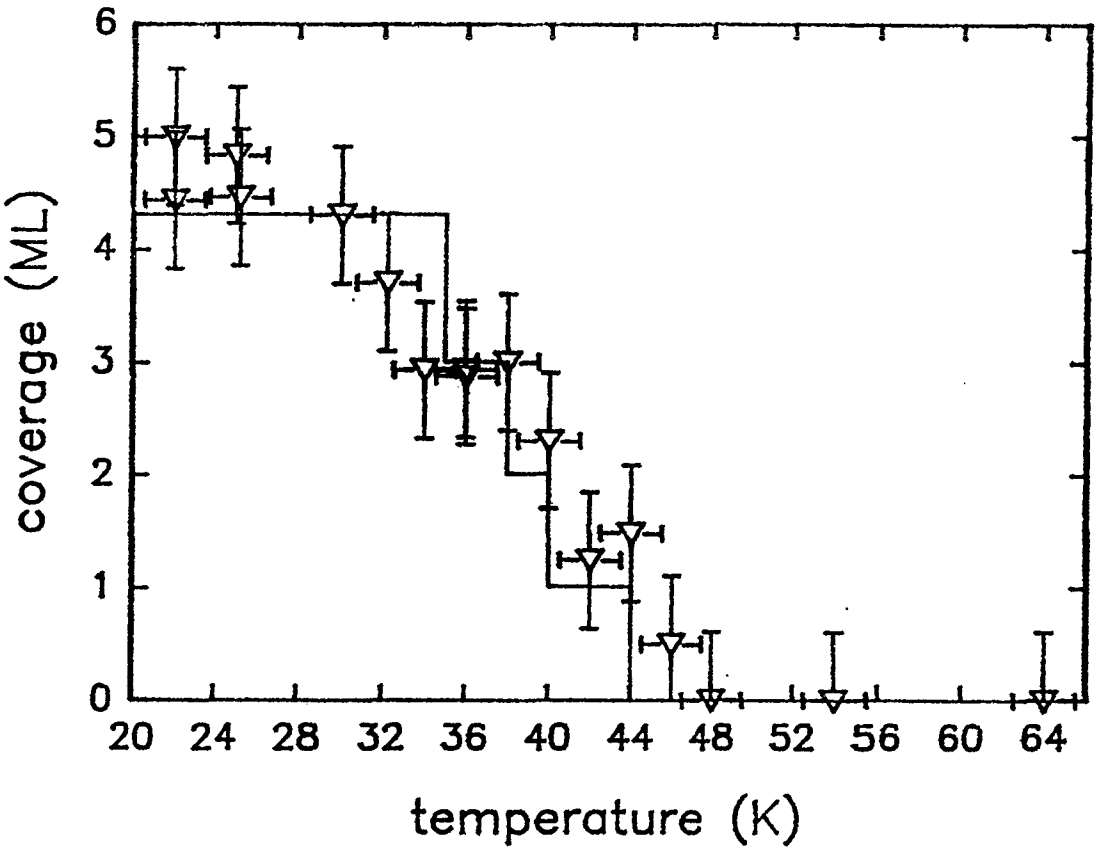

FIG. IV.10. Amount of 3D solid (v) as a function of increasing temperature. Normalization to obtain coverage units is described in the text (see Sec. D.4). The stepwise curve is based on the prediction of layering transitions by Volkmann and Knorr, as discussed in the text (see Sec. D.4).[23]

Error bars in temperature are included representing the a worst case temperature shift of approximately 1.5 K due to capillary condensation. When the data are compared in this way, it is clear that our data are consistent with the ellipsometry data. Almost every point falls on the predicted transition curve within error. However, as stated above, we cannot definitively confirm discrete layering transition temperatures.

The primary effect of capillary condensation in this system seems to be smearing out of the discrete layering transitions observed on a HOPG substrate. We believe layering is responsible for the gradual decrease of the bulk peaks in our diffraction scans, and that capillary effects broadened the transitions so that we do not observe discrete layering transition temperatures. Again, structural measurements of N_2 on HOPG would clarify what effects, if any, the pore structure of the substrate has on the inherrent structural properties of these layering transition. For example, we see α-ß coexistence and temperature hysteresis; structural measurements on HOPG would clarify if a porous substrate had any affect on these.

G. Measurement of capillarity

It is clear from the above analysis that it is important to carefully consider the effects of porosity on experiments where capillary condensation may be important, such as our multilayer N_2 studies on graphite foam. In our studies, our analysis determined capillary condensation smeared out the layering transition

temperatures, but did not disallow the layering to occur. This analysis used two important data derived from vpis: the pore size distribution, and the amount of material capillary condensed. As discussed in detail in Sec. F.1, the pore size distribution is directly related to shifts in phase transition temperatures. The amount of capillary condensed material determines the relative importance of capillary effects. For example, if we determined 10% of our material was capillary condensed, then we can estimate how this would affect diffraction data, as done in Sec. F.

As described above, the adsorption-desorption isotherm is an important tool in the measurement of pore size distribution, and the amount of material capillary condensed. The existence of a hysteresis loop indicates that capillary condensation occurs in a sample. From measuring the pressure on the desorption branch, we can calculate the pore size distribution (see Sec. F.1). Also, by comparing an isotherm that exhibits capillary condensation to one that does not, we can estimate the amount of material adsorbed in layers to the amount capillary condensed (see Sec. F.1).

There are other important questions that could be addressed by detailed vapor pressure isotherm studies. For example, analysis of our multilayer N_2 on graphite work raised speculation that the porosity of the sample may be affected by sample preparation (Sec. F.2). Isotherms of N_2 on samples prepared differently (e.g., baked at moderate temperatures versus high temperatures) would be ideal to address this. If the gas handling system used in isotherm studies has

variable sample temperature, studies of capillary effects versus system temperature are possible. Referring to Eq. (IV.3), we see $\ln p/p_o$ varies as $1/T$, provided $\gamma\cos\phi$ (the product of the liquid-vapor interfacial energy and the cosine of the contact angle) are constant. If isotherms are done at several temperatures, we can plot $\ln p/p_o$ versus $1/T$, for the pressure where the hysteresis loop in the isotherm opens up. If this plot is nonlinear, we can infer information about $\gamma\cos\phi$. Since this is an important term in the free energy of the adsorbed system, we can gain fundamental insight into the thermodynamic behavior of capillary condensed systems.

Indeed, in order to extend our N_2 on graphite study, we are building a gas handling system capable of multilayer adsorption studies. It is described in detail in App. B. Briefly, the system has a sample temperature range of 30 to 300 K with an accuracy of $\pm$ 0.1 K. It can measure pressures from 0 Torr $\pm$ 0.05% to 1500 Torr $\pm$ 0.1%. For N_2 on graphite, we can accurately perform isotherms on systems with temperatures bwtween T = 55 K ($p_o \approx$ 10 Torr) and 82 K ($p_o \approx$ 1500 Torr). We can easily measure hysteresis in adsorption-desorption isotherms, to determine pore size distributions and amount capillary condensed in our samples. By measuring isotherms on differently prepared samples, we can address whether baking affects capillarity.

One very important feature of this experimentally accessible temperature range for our gas handling system is that it spans the N_2 triple point temperature. This allows us to do isotherms above and

below T_{tp}, and compare them. We argue that we do not observe significant amounts of capillary condensed material below T_{tp}; this would be evident in an isotherm as a very small hysteresis loop, and hence independently verified. An isotherm above T_{tp} would address whether this lack of capillary condensation below T_{tp} was thermodynamic, i.e., due to lower free energy for film layers versus capillary condensed solid, or due to a lack of pore structure, i.e., because our sample does not exhibit capillary condensation at any temperature. This would be important corroborative evidence in our study of multilayer N_2 on graphite, and on the effects of using a graphite foam sample.

H. Conclusions

For multilayer N_2 adsorbed on graphite, we have determined the system undergoes layering transitions from x-ray diffraction measurements. We do not measure discrete temperatures where these layering transitions occur, most likely due to temperature broadening from capillary effects. The results of our studies are put in context with previous research on N_2 on graphite in a new, proposed multilayer phase diagram. This is synthesized from careful analysis of both our work, and the combined results of previous work. The effects of capillary condensation on this system are quantified, and we find the primary effect to be a broadening of the layering transition temperatures, from discrete values to a continuous range of temperatures. This point will be further clarified by precision

measuring isotherm measurements using a precision vapor pressure isotherm. The system is capable of determining the existence and extent of capillary condensation on the graphite foam sample.

CHAPTER V

CONCLUSIONS

In this dissertation, we studied several different systems that exhibit asymmetric adsorbate-adsorbate and adsorbate-substrate interactions. We determined rich behavior in these physisorbed systems, due to asymmetries. We now summarize our findings, and address how asymmetry is manifest in these systems as phase transitions in the mono- and multilayer phase diagrams (Sec. A). We also discuss possible extensions of this work (Sec. B).

A. Asymmetries in adsorbed systems

For dipolar molecules on ionic crystal systems, we have two different asymmetric interactions. First, the binding energy is asymmetric with respect to dipole orientation. Secondly, the interactions between dipoles are asymmetric; this is further complicated by induced dipole moments which arise from interaction of the molecule with the strong substrate electric field. These asymmetries allow for dipole ordering, or dielectric phases in the monolayer phase diagram.

In the case of CO on MgO, the binding asymmetries determined a low temperature phase (for all coverages) which is ferroelectric, with all CO adsorbed C-down (the orientation preferred by binding asymmetries). At high temperature, the average spin approaches zero, as entropy effects begin to dominate. If we assume no binding asymmetry, we find a low temperature phase which is also FE, but which

is determined by the lower interaction energy of a raft of CO molecules all adsorbed O-down, as determined by adsorbate-adsorbate interaction asymmetries. Again, at high T, entropy effects destroy this ordering.

In the case of halogenated methanes on NaCl, the molecular dipole moment, and hence the interaction energies are much larger. Additionally, the total dipole moments for the two orientations have different signs; this favors antiferroelectric phases. This system exhibits a low temperature, low coverage FE phase, determined by the binding asymmetry. However, for $\theta \geq 0.5$, the low temperature phase is AFE, as determined by asymmetric dipole-dipole interactions. The AFE phase becomes FE at high temperature. This systems exhibits two phase transitions, a low T FE $\rightarrow$ AFE phase transition with increasing coverage, and a AFE $\rightarrow$ FE phase transition at high coverage driven by temperature.

Indeed, in all of the dipolar molecule on ionic crystal systems studied, the interaction asymmetries determined rich 2D phase diagrams. Let us put these in context with previous work on asymmetries in 2D phase diagrams. Chapter I, Sec. B.4, outlined how asymmeteries add ordering phases to the simple liquid-solid-gas phase diagrams observed for rare gasses adsorbed on atomic substrates such as graphite. The simplest ordering phases occur due to steric interactions, such as for CO on graphite. Electrostatic interactions also cause ordering phases. For example, dipole interactions cause dielectric phases for the halogenated phases; quadrupole interactions

cause orientationally ordered phases for many adsorbates on graphite, such as N_2 on graphite.

For all of the systems presented in the previous paragraph, the graphite is somewhat inert. It provides adsorption sites for the molecules; for some systems (e.g., Kr on graphite) competition between adsorbate-adsorbate interactions and the substrate corrugation potential causes commensurate to incommensurate phase transitions in the 2D solid monolayer. The graphite surface does not have a strong surface electric field, in contrast to substrate such as ionic crystals.

Ionic crystal substrates, such as MgO and NaCl studied here, allow for further asymmetries in adsorbate interactions. For example, the substrate electric field can interact with electric multipole moments of an adsorbate, and cause large differences in binding energies as a function of adsorbate orientation (as seen for CO on MgO and NaCl). Additionally, the substrate surface electric field can induce additional dipole moments in polarizable molecules. A striking example of this is the activation of an ir active dipole stretching mode for the otherwise non-dipolar, ir-inactive N_2 on NaCl. Induced dipoles are also seen for CO on MgO and NaCl.

The systems we study here are among the most difficult to understand and model. Both CO and the halogenated methanes have natural dipole moments, as well as higher multipole moments (although we do not consider these here for the halogenated methane), and both exhibit orientation-dependent adsorbate-adsorbate interactions. When

adsorbed to substrates such as MgO and NaCl (which have strong surface electric fields), new orientation-dependencies occur, through large binding asymmetries, and induced multipole moments.

The model we develop here is an important step in understanding the 2D phase diagrams of dipolar molecules on ionic crystals. We are able to incorporate most interaction asymmetries (to first order) and determine possible dielectric phases and phase transitions for these complicated systems. Dielectric phases seen here could not be realized in systems such as rare gases on ionic crystals, since rare gases have spherically symmetric adsorbate and substrate interactions.

The multilayer N_2 on graphite phase diagram exhibits very complex behavior, caused mainly by asymmetries in the N_2 interactions, such as the quadrupole interaction. Incomplete wetting is found at low temperature. The bulk nitrogen exists in an α-phase, an orientationally ordered phase due to asymmetric quadrupole interactions. At $T_{\alpha\text{-}ß}$, bulk N_2 undergoes an orientational-disordering phase transition (there is no preferred molecular orientation). We find that this 3D phase transition manifests itself as a 2D phase transition. The system undergoes a layering transition, apparently driven by the bulk α-ß phase transition. Subsequent layering transitions occur as the temperature increases. Layering transitions driven by bulk orientational transitions (other than triple point wetting) are not expected for spherically symmetric rare gas systems.

Recall Chapter I, Sec. B.5. We were originally interested in studying whether additional 3D phase transitions (such as

orientational order-disorder transitions) can actuate 2D phase transitions (such as layering), in analogy to triple point wetting. Triple point wetting most likely occurs because bulk melting alleviates strain between the bulk crystal structure and that of the 2D film, allowing for continuous growth of the 2D film. By analogy, we can seek similar arguments for why the orientational α-ß phase transition allows for additional 2D layer growth. One possible explanation is that orientational disorder alleviates strain between the orientational order of the film crystal structure versus that of the bulk. For N_2 on graphite below $T_{\alpha-\beta}$, the uppermost layers of the 2D film are amorphous (and hence likely do not have specific orientational order) while α-N_2 is pinwheel in orientation. Bulk transition to an orientationally disordered state may alleviate strain between the amorphous top layer and the bulk.

Just as triple point wetting is not expected for all adsorbate-substrate systems, layering transitions tied to bulk orientational transitions apparently are also non-universal. In particular, CO and O_2 on graphite, seemingly very similar systems to N_2 on graphite (see Chap. IV, Sec E), do not exhibit layering transitions actuated by bulk structural orientational disordering transitions. A possible explanation may be that additional adsorbate-adsorbate interactions (such as steric or dipole interactions for CO, and magnetic for O_2) cause more complicated behavior. Theoretical modeling, such as molecular dynamics studies, may clarify our understanding of these phenomena.

These results provide interesting insight into the structure and phases of physisorbed systems. We find that in the systems studied here, complicated phases diagrams arise due to relatively simple asymmetric interactions. Particularly interesting is the complex behavior of N_2 on graphite. This rich phase diagram seems to arise solely due to the asymmetric quadrupole interactions between nitrogen molecules. [This is an oversimplification of the problem, as lattice frustration (which one finds for rare gas atoms) also plays an important role.] An interesting theoretical study would be to calculate the nitrogen on graphite phase diagram obtained without quadrupole-quadrupole interactions and compare the results to the actual phase diagram. This should gauge how important asymmetric interactions are in determinig the complex 2D behavior.

The rich monolayer phase diagrams for the dipolar molecules are also a beautiful manifestation of asymmetric interactions causing ordered phases. Our study is particularly satisfying because the results match our initial predictions, and hence our understanding of the complex interactions occuring in these systems. Experimental realization of these phases would complete the picture. However, if these phases are not realized, different interesting studies as to why they do not occur would arise.

B. Future Work

There are many interesting studies that can address asymmetries in physisorbed systems. In this section, the success of the work done

here is critiqued and possible extensions to this work proposed. The discussion is limited to those studies that pertain to the systems studied here.

The general model for adsorbed diplar molecules on ionic crystals produced interesting results for the systems we study here. These results are consistent with our physical understanding of these systems; this gives us confidence in the applicability of the model. The Ising model developed here can be used to study other physisorbed systems. It can be applied most directly to other dipolar adsorbed systems; however, any system which can be mapped onto a Hamiltonian such as Eq (II.3) or Eq (II.4) can be studied in this manner. Indeed, our results are quite general, and map out previously unexplored regions in interaction parameter space.

The model is a first approximation to the real physical situation, and of course has some limitations. For example, we consider only square-symmetric lattices. A more realistic model might include the possibility of rectangular lattices, such as those measured for CO on MgO (see Chap. II, Sec. D.1). Other interesting phase transitions might be found if the model is solved simultaneously for the average spin and coverage as a function of temperature, rather than for the average spin with fixed coverage as a function of temperature (see Chap. II, Sec. D.4). Phenomena such as film desorption ($\theta \rightarrow 0$) might be observed in this manner.

The full Hamiltonian for the AFE case [Eq (II.4)] has not been studied as a function of J, K, L, Δ, and H, as has been done for the

FE case [Eq. (II.3); see Chap. II, Sec. C.3]. This work most definitely should be undertaken. Once completed, determining whether interesting phase transitions occur for any adsorbed system that can be modeled by Eq. (II.4) should be as simple as determining J, K, L, Δ, and H for the system (which is not necessarily simple).

For dipolar molecules on ionic crystals, preliminary studies of the halogenated methanes show that these systems hold particular promise for rich, experimentally measurable 2D monolayer phase diagrams. There has been very little experimental or theoretical work on these systems. It seems that studies of these systems are warranted, in order to determine whether our theoretically predicted phases exist. Theoretical and experimental studies are necessary to determine the energy parameters needed for future modelling studies.

Due to the poor x-ray scattering characteristics of CO, our diffraction studies were unsuccessful. The phase diagram for CO on MgO remains virtually unmapped. Structural studies (other than the LEED measurements mentioned above) of this system are necessary. X-ray diffraction proved not to be an appropriate probe; neutron diffraction studies mentioned in Chap. III, Sec. F, may yield useful structural information. Helium diffraction studies may also be appropriate; such studies were used successfully to study CO on NaCl.

For N_2 on graphite, layering transitions were successfully measured, verifying the results of previous ellipsometry experiments. The x-ray diffraction data provide structural information, which is

not measurable using ellipsometry. This structural information raises some very intersting questions. We observe hysteresis in both the growth of the 2D films and in the α-ß phase transistion of the bulk material. Further study to understand this hysteresis is necessary.

The use of a graphite foam sample raised questions about how capillarity affects multilayer adsorption studies. The results presented here indicate that capillary effects are present as shifted transitions temperatures, but capillarity does not perclude layering. Experimental studies of other systems, and theoretical studies of solid capillary material, are necessary. Also, it should be determined whether capillary effects play a role in the hysteresis we observe.

For multilayer systems, future work might include studies of other asymmetric molecules. Natural systems to consider include O_2 or CO on graphite, as discussed above. Other orientationally ordered systems include CO_2, CS_2, and C_2H_6 [See Chap. I, Sec. B.4]. Determination and analysis of the multilayer phase diagrams of many systems would clarify the mechanisms for layering behavior. Experimental and theoretical studies would be helpful in determining what aspects of asymmetric interactions are important to layering, and to the actuation of layering transitions by bulk orientational transitions. In particular, examination of the roles of such forces as asymmetric steric, electric, and dispersion forces would be elucidating.

REFERENCES

[1]S.J. Gregg and K.S.W. Sing, Adsorption, Surface Area and Porosity, (Academic Press, New York, 1967), p. 1.

[2]D.M. Young and A.D. Crowell, Physical Adsorption of Gases, (Butterworths, Washington, 1962), p. 1-5.

[3]R.E. Peierls, Helv. Phys. Acta Suppl. 7, 81 (1934); L.D. Landau, Collected Papers of L.D. Landau, D. Ter Haar, Ed. (Gordon and Breach, New York, 1965), pp. 201-220.

[4]J.M. Kosterlitz and D.J. Thouless, "Ordering, metastability, and phase transitions," J. Phys. C 6, 1181 (1973).

[5]A. Thomy and Y. Duval, J. Chim. Phys. Phys. Chim. Biol. 66, 1966 (1969).

[6]J.G. Dash, "Between two and three dimensions," Physics Today 38 (12), 26 (1985).

[7]Andrew Zangwill, Physics at Surfaces, (Cambridge University Press, Cambridge, 1988), pp. 185-6.

[8]F.C. Frank and J.H. van der Merwe, "One dimensional dislocations I. Static theory," Royal Soc. Proc. (London) A 198, 205 (1949).

[9]William Steele, "Molecular interactions for physical adsorption," Chem. Rev. 93, 2355 (1993), and references therein.

[10]G.B. Hess, in Phase Transitons in Surface Films 2, edited by H. Taub *et al.* (Plenum Press, New York, 1991), pp. 357-390.

[11]D. P. Landau, in Phase Transitons in Surface Films 2, edited by H. Taub *et al.* (Plenum Press, New York, 1991), pp. 11-40.

[12]R. Wang, S.-K. Wang, H. Taub, J.C. Newton, and H. Schecter, "Orientational oreder in nitrogen monolayers adsorbed on graphite at low temperature," Phys. Rev. B 35, 5841 (1987).

[13]H. Weichert and S.-A. Arlt, "Observation of random-field behavior in $(CO)_{1-x}(N_2)_x$ mixtures physisorbed on graphite," Phys. Rev. Lett. 71, 2090 (1993).

[14]D. Marx, S. Sengupta, P. Nielaba, and K. Binder, "Clarification of the head-tail ordering of CO on graphite: A Monte Carlo study," Phys. Rev. Lett. 72, 262 (1994).

[15]F.Y. Hansen and H. Taub, in Phase Transitons in Surface Films 2,

edited by H. Taub *et al.* (Plenum Press, New York, 1991), pp. 153-168.

[16]P.A. Rowntree, G. Scoles, and J.C. Ruiz-Suarez, "Low energy helium scattering from ordered physisorbed layers of polar molecules," J. Phys. Chem. **94**, 8511 (1990).

[17]K. Knorr and W. Weichert, "Two-dimensional crystalline phases of CH_3F adsorbed on graphite," Phys. Rev. B **37**, 3524 (1987).

[18]W. Weimer, K. Knorr, and H. Weichert, "X-ray diffraction study of CF_3Cl monolayers adsorbed on graphite (001)," Z. Phys. B - Cond. Mat. **73**, 235 (1988).

[19]J.G. Dash, "Clustering and percolation transitions in helium and other thin films," Phys. Rev. B **15**, 3136 (1977).

[20] J.L. Seguin, J. Suzanne, M. Bienfait, J.G. Dash, and J.A. Venables, "Complete and incomplete wetting in multilayer adsorption: High-energy electron-diffraction studies of Xe, Ar, N_2, and Ne films on graphite," Phys. Rev. Lett. **51**, 122 (1983).

[21]R. Pandit and M.E. Fisher, "Wetting transitions near bulk triple points," Phys. Rev. Lett. **51**, 1772 (1983).

[22]R. Pandit, M. Schick, and M. Wortis, "Systematics of multilayer adsorption phenomena on attractive substrates," Phys. Rev. B **26**, 5112 (1982).

[23]U.G. Volkmann and K. Knorr, "Multilayer growth and wetting behavior of nitrogen physisorbed on graphite," Phys. Rev. Lett. **66**, 473 (1991).

[24]S.G.J. Mochrie, M. Sutton, R.J. Birgeneau, D.E. Moncton, and P.M. Horn, "Multilayer adsorption of ethylene on graphite: Layering, prewetting, and wetting," Phys. Rev. B **30**, 263 (1984).

[25]J.R. Dennison, H. Taub, F.Y. Hansen, H. Schecter and R. Brener, "Anomalous layering of $Fe(CO)_5$ adsorbed on graphite," Phys. Rev. B **37**, 2266 (1988).

[26]See e.g., S. Dietrich, in Phase Transitions and Critical Phenomenon, edited by C. Domb and J.L. Lebowitz, (Academic, London 1988), Vol. 12, p. 1.

[27]M. Bienfait, "Wetting and multilayer adsorption," Surf. Sci. **162**, 411 (1985).

[28]T.A. Scott, "Solid and liquid nitrogen," Phys. Rep. **27**, 89 (1976).

[29]R.K. Pathria, Statistical Mechanics, (Pergamon Press, New York, 1972), pp. 392-408.

[30]W. Brakeman and A.L. Mossman, Matheson Gas Data Book, (Matheson, Lyndhurst, 1976), pp. 130-137, 522-530.

[31]J.E. Gready, G.B. Backsay, and N.S. Hush, "Comparisons of multipole moment expansions by direct summation or finite field SCF methods with full electrostatic interaction energies: Application to CO and N_2," Chem. Phys. 31, 375 (1978).

[32]G. Pacchioni, G. Cogliandro, and P.S. Bagus, "Molecular orbital cluster model study of bonding and vibrations of CO adsorbed on MgO surface," Int. J. of Quant. Chem. 42, 1115 (1992).

[33]S.G. Brush, "History of the Lenz-Ising model," Rev. Mod. Phys. 39, 883 (1967).

[34]E. Ising, "Beitrag zur theorie des ferromagnetismus," Z. Phyzik 31, 253 (1925).

[35]J.M. Yeomans, Statistical Mechanics of Phase Transitions, (Oxford University Press, Oxford, 1992), pp. 33-63.

[36]J. Sivardière and J. Lajzerowicz, "Spin-1 lattice gas model. II. Condensation and phase separation in a binary fluid," Phys. Rev. A 11, 2090 (1975).

[37]M. Blume, V.J. Emery, and R.B. Griffths, "Ising model for the λ-transition and phase separation in He^3-He^4 mixtures," Phys. Rev. A 4, 1071 (1971).

[38]M. Schick and W.-H. Shih, "Spin-1 model of a microemulsion," Phys. Rev. B 34, 1797 (1986).

[39]J. Lajzerowicz and J. Sivardiere, "Spin-1 lattice gas model. I. Condensation and solidification of a simple fluid," Phys. Rev. A 11, 2079 (1975).

[40]F.Y. Wu, "Phase diagram of a spin-1 Ising model," Chinese J. Phys. 16, 153 (1978).

[41]W. Hoston and A. Nihat Berker, "Multicritical phase diagrams of the Blume-Emery-Griffiths model with repulsive biquadratic coupling," Phys. Rev. Lttrs. 67, 1027 (1991).

[42]F.Y. Wu, private communication.

[43]V.J. Emery, K. Fahricus, and S.A. Kivelson, "Study of Ising model with competing long-range and short-range interactions," Phys. Rev. Lett. 72, 1918 (1994).

[44]C.N. Yang and T.D. Lee, "Statistical theory of equations of state

and phase transitions. II. Lattice gas and Ising model," Phys. Rev. 87, 410 (1952).

[45]N.W. Ashcroft and N.D. Mermin, Solid State Physics, (Holt, Rinehart, and Winston, New York, 1976), p. 80.

[46]H.H. Richardson and G.E. Ewing, "Infrared spectroscopy of CO on NaCl film and NaCl (100)," J. Electron Spectroscopy and Related Phenomena 45, 99 (1987).

[47]D. Schmicker, J.P. Toennies, R. Vollmer, and H. Weiss, "Monolayer structures of carbon monoxide adsorbed on sodium chloride: A helium atom diffraction study," J. Chem. Phys. 95, 9412 (1991).

[48]R. Gevirzman, Y. Kozirovski, and M. Folman, "Infrared spectra and spectral shifts of CO adsorbed on evaporated alkali-halides," Trans. Fara. Soc. 65, 2206 (1968).

[49]H.H. Richardson, C. Baumann, and G.E. Ewing, "Infrared spectroscopy and thermodynamic measurements of CO on NaCl films," Surf. Sci. 185, 15 (1987).

[50]H.H. Richardson and G.E. Ewing, "Infrared Spectrum of CO on NaCl (100)," J. Phys. Chem. 91, 5833 (1987).

[51]A. Lakhilfi, "Analysis of the interaction potential of a molecule physisorbed on NaCl (100) surface," Mol. Phys. 78, 659 (1993).

[52]R. Dovesi, R. Orlando, F. Ricci, and C. Roetti, "CO adsorption on MgO crystals: Hartree-Fock calculations for regular adlayers on a (001) lattice plane," Surf. Sci. 186, 267 (1987).

[53]E.A. Colburn and W.C. Mackrodt, "Theoretical aspects of H_2 and CO chemisorption on MgO surfaces," Surf. Sci. 117, 571 (1982); "A theoretical study of CO chemisorbed at {001} surfaces of non-defective and doped MgO," 143, 391 (1984).

[54]A. Lakhlifi and C. Girardet, "Potential surfaces and adsorption energy of Xe, CH_4, N_2, CO, NH_3, and CH_3F molecules on MgO surface," Surf. Sci. 241, 400 (1990).

[55]E. Escalona-Platero, D. Scarano, G. Spoto, and A. Zecchina, "Dipole coupling and chemical shifts of CO and NO adsorbed on oxides and halides with rock salt structure," Faraday Disc. Chem. Soc. 80, 183 (1985).

[56]S.A. Pope *et al.*, "A theoretical study of the adsorption of simple molecules on MgO surfaces: CO, HCO, HOC, H_2CO, HCOH, CH_2OH, and CH_3O," Surf. Sci. 139, 299 (1984).

[57]P. Audibert, M. Sidoumou, and J. Suzanne, "CO adsorbed on MgO (100): High resolution LEED study," Surf. Sci. 273, L467-L471 (1992).

[58]D.E. Storgyn and A.P. Storgyn, "Molecular multipole moments," Mol. Phys. 11, 371 (1966).

[59]A. Ben-Ephraim *et al.*, "Predesorption of CO from the sodium chloride (100) surface: Study by complex coordinate method," J. Chem. Phys. 89, 3840 (1988).

[60]P.Hollins and J. Pritchard, "Infrared studies of chemisorbed layers on single crystals," Prog. Surf. Sc. 19, 275 (1985); B.N. Persson and R. Ryberg, "Vibrational interaction between molecules adsorbed on a metal surface: The dipole-dipole interaction," Phys. Rev. B 24, 6954 (1981).

[61]J.-W. He *et al.*, "CO adsorption on ultrathin MgO films grown on a Mo(100) surface: IRAS study," Surf. Sci. 261, 164 (1992).

[62]H.-C. Chang, H.H. Richardson, and G.E. Ewing, "Epitaxial growth of CO on NaCl (100) studies by infrared spectroscopy," J. Chem. Phys. 89, 7561 (1988).

[63]H. You and S.C. Fain, "Structure of carbon monoxide monolayers physisorbed on graphite," Surf. Sci. 151, 361 (1985).

[64]I. Inaba, T. Shirakami, and H. Chihara, "Complete dipolar ordering in solid overlayers of CO physisorbed on graphite basal plane: Heat capacity measurement," Chem. Phys. Lett. 146, 63 (1988).

[65]K. Morishige, C. Mowforth, and R. K. Thomas, "Orientational order in CO and N_2 monolayers on graphite studied by x-ray diffraction," Surf. Sci. 151, 289 (1985).

[66]A. van der Pol, A. van der Avoird, and P.E.S. Wormer, "An *ab-intio* intermolecular potential for the carbon monoxide dimer $(CO)_2$," J. Phys. Chem. 92, 7498 (1990).

[67]K. Knorr, "Monolayers of polar methane derivatives physisorbed on graphite", Physics Rep. 214, 115 (1992).

[68]T.E. Burns and J.R. Dennison, "Polar molecules on ionic crystals: Preliminary calculations for phase transitions in the BEG model," Bull. Am. Phys. Soc. 39, 500 (1994).

[69]J. Heidberg, H. Stein, and E. Riehl, "Resonance rate, and quantum yield of infrared-laser-induced desorption by multiquantum vibrational excitation of the adsorbate CH_3F on NaCl," Phys. Rev. Lett. 49, 666 (1982).

[70]R.D. Singh and A. Shaukat, "Physical interaction of nonpolar gases with ionic solids: adsorption of methane on sodium chloride," Zeitschrift fur Physicalische Chemie Neue Folge **110**, 159 (1978).

[71]F. Kohler and N.V. Nhu, "The second virial coefficients of some halogenated methanes," Molecular Physics **80**, 795 (1993).

[72]J.L. Jordan, J.P. McTague, J.B. Hastings, and L.Passell, "An x-ray diffraction study of krypton adsorbed on MgO (100) surfaces," Surf. Sci. **150**, L82 (1985).

[73]J.L. Jordan, "An x-ray diffraction study of the structure and melting of krypton adsorbed on magnesium oxide," Thesis, UCLA, BNL Pub. Number 33760 (1985).

[74]D.Degenhardt, H.J. Lauter, and R. Frohm, "Kr and Xe monolayers adsorbed on MgO powder studied by x-ray diffraction," Surf. Sci. **215**, 535 (1989).

[75]H. Weichert, C. Tiby, and H.J. Lauter, "Absence of continuous nucleation for ^{4}He on MgO," J. Phys. C **13**, L1039 (1980).

[76]J.P. Coulomb, K. Madih, B. Croset, and H.J. Lauter, "Evidence of a square two-dimensional solid of methane physisorbed on the (100) surface of magnesium oxide," Phys. Rev. Lett. **54**, 1536 (1985).

[77]K. Madih, B. Croset, J.P. Coulomb, and H. Lauter, "Thin methane film growth mode on MgO/100 surface," Europhys. Lett. **8**, 459 (1989).

[78]J. Gay, M. Bienfait, J.P. Coulomb, J. Suzanne, H. Blank, and P. Convert, "Surface premelting of thin films of methane," Physica B **156 and 157**, 273 (1989).

[79]T. Angot, J. Suzanne, and J.Y. Hoarau, "An original *in situ* cleaver for low teperature surface experiments," Rev. Sci. Instrum. **62**, 1865 (1991).

[80]P.Dai, T. Angot, S.N. Ehrlich, S.-K. Wang, and H. Taub, "Structural perfection in physisorbed films: A synchrotron x-ray diffraction study of xenon on the Ag(111) surface," Phys. Rev. Lett. **72**, 685 (1994).

[81]J.R. Dennison, S.-K. Wang, P.Dai, T. Angot, H. Taub, and S.N. Ehrlich, "Ultrahigh vacuum chamber for synchrotron x-ray diffraction from films adsorbed on single crystal surfaces," Rev. Sci. Instrum. **63**, 3835 (1992).

[82]J.P. Coulomb and O.E. Vilches, "Adsorption physique de molécules simples sur une surface homgène de symétrie. I. Préparation et caractérisation du substrat d'oxyde de magnésium," J. Physique **45**, 1381 (1984).

[83]J.G. Dash. R. Ecke, J. Stottenberg, O.E. Vilches, and J. Whittemore, Jr., "Uniform magnesium oxide absorbent," J. Phys. Chem. 82, 1450 (1978).

[84]C.F. Jones, R.L.Segall, R. St. C. Smart, and P.S. Turner, "Size distribution of MgO smoke particle," Philosophical Mag. A 42, 267 (1980).

[85]A.F. Moodie and C.E. Warble, "Electron Microscopic investigations of MgO morphology and surfaces," J. Crystal Growth 10, 26 (1971).

[86]J.P. Coulomb, T.S. Sullivan, and O.E. Vilches, "Adsorption of Kr, Xe, and Ar on highly uniform MgO smoke," Phys. Rev. B 30, 4753 (1984).

[87]A.G. Shastri, H.B. Chase, M. Bretz, and J.Schwank, "Morphology and surface uniformity growth in MgO dehydration," J. Phys. Chem. 89, 3761 (1985).

[88]K. Morishige, S. Kittaka, and T. Morimoto, "Adsorption of Kr on ZnO, SnO_2, MgO, and CdO surface homogeneity and the effect of surface hydroxyls," J. Colloid. Interface Sci. 89, 86 (1982).

[89]N.F. Gmur, W. Thomlinson, and S.M. White-DePace, NSLS User's Manual 139, 299 (1984).

[90]J.P. Coulomb, private communication.

[91]M. Yin, "New opticals system for studying infrared spectra of the electrochemical double layer and surface adsorption," Dissertation, Utah State University, unpublished (1992).

[92]T. Will, "Extension of the metal light pipe infrared spectroscopy technique: Applications to surface adsorption and high T_c superconductors," Thesis, Utah State University, unpublished (1990).

[93]J.R. Dennison and W.N. Hansen, private communication.

[94]S.-K. Wang, J.C. Newton, R. Wang, H. Taub, J.R. Dennison, and H. Schecter, "Multilayer structure of N_2 adsorbed on graphite," Phys. Rev. B 39, 10331 (1989).

[95]Q.M. Zhang, H.K. Kim, and M.H.W. Chan, "Growth mode and phase transistions of multilayer nitrogen on graphite," Phys. Rev. B 33, 413 (1986); "Commensurate-uniaxial-incommensurate transition of nitrogen on graphite," Phys. Rev. B 32, 1820 (1985).

[96]S.F. Shea and M.L. Klein, "Orientational phasea of a quadrupolar bilayer," Phys. Rev. B 25, 5882 (1982); A. Vernov and W.A. Steele, "Simulations of bilayers of N_2 adsorbed on graphite at 25 and 35 K," Surf. Sci. 171, 83 (1986); B. Kuchta and R.D. Etters, "Calculated

properties of monolayer and multilayer N_2 on graphite," Phys. Rev. B 36, 3400 (1987).

[97]J.K. Kjems, L. Passell, H. Taub, J.G. Dash, and A.D. Novaco, "Neutron diffraction study of nitrogen adsorbed on basal plane oreineted graphite," Phys. Rev. B 13, 1446 (1976).

[98]J.Z. Larese, Q.M. Zhang, L. Passell, J.M. Hastings, J.R. Dennison, and H. Taub, "Layer by layer growth of solid argon films on graphite as studied by neutron diffraction," Phys. Rev. B 40, 4271 (1989).

[99]B.E. Warren, X-ray Diffraction, (Dover, New York, 1990), p. 366.

[100]A.F. Schuch and R.L. Mills, "Crystal structures of three modifications of $N_2$14 and $N_2$15 at high pressure," J. Chem. Phys. 52, 6000 (1970).

[101]T.T. Chung and J.G. Dash, "Approach to bulk behavior in N_2 films adsorbed on basal plane graphite," J. Chem. Phys. 64, 1855 (1976).

[102]R. DeFay and I. Prigogine, Surface Tension and Adsorption, (Longman's, London, 1966), p. 1.

[103]CRC Handbook of Chemistry and Physics, (CRC Press, Boca Raton, Florida, 1979), p. B-233.

[104]K. Morishige, K. Kawamura, M. Yamamoto, and I. Ohfuji, "Capillary condensation of Xe on exfoliated graphite," Langmuir 6, 1417 (1990).

[105]E. LeDoux, Vapor Adsorption, (Chemical Publishing Co., Brooklyn, 1945), p. 30.

[106]M.J. Lysek, M. La Madrid, P. Day, and D. Goodstein, Adsorption hysteresis, capillary condensation, and melting in multilayer methane films on graphite foam," Langmuir 8, 898 (1992).

[107]N.J. Wilkinson, M.A. Alam, J.M. Clayton, R. Evans, H.M. Fretwell, and S.G. Usman, "Positron annihilation study of capillary condensation of nitrogen gas in a mesoporous solid," Phys. Rev. Lett. 69, 3535 (1992).

[108]J.L. Tell and H.J. Maris, "Specific heats of hydrogen, deuterium and neon in porous Vycor glass," Phys. Rev. B 28, 5122 (1983).

[109]A.R. Nyaiesh and W.B. Nowack, "Chemisorbed hydrogen an a-carbon films," J. Vac. Sci. A 1, 308 (1983).

[110]R.O. Dillon, J.A. Woolam, and V. Katkanant, "Use of Raman scattering to investigate disordered crystallite formation in as-deposited and annealed carbon films," Phys. Rev. B 29, 3482 (1984).

[111]J.C. Newton, "The structure and phase transitions of linear chain hydrocarbons on graphite," Dissertation, University of Missouri-Columbia, unpublished (1989).

[112]R.M. Suter, N.J. Collela, R. Gangwar, and W. Wang, "High-precision vapor-pressure isotherms: Apparatus, errors, and results," Rev. Sci. Instrum. **58**, 462 (1987).

[113]T.E. Burns, J.R. Dennison, and B. Evans, USU Automated Gas Handling System Manual, unpublished (1993).

[114]H. Chi, in USU Surface Physics Group Databook No. 6, unpublished (1991).

[115]L. Gardner, in USU Surface Physics Group Databook No. 10, unpublished (1993).

APPENDICES

APPENDIX A

POWDER X-RAY DIFFRACTION

A. Principles of Powder X-ray Diffraction

1. Introduction

X rays are electromagnetic radiation with wavelengths on the order of 1 Å. This is comparable to the interplanar distance in crystals. In the same way that visible light will diffract through the slits of a diffraction grating, x rays will diffract if they are passed through a crystal. The diffraction pattern is characteristic of the crystal structure. This phenomenon has made x-ray diffraction a very powerful tool in analyzing crystal structure from very simple cubic structures to the very complex structures of crystallized DNA, or penicillin.

X-ray diffraction can be used to study 2D structures as well as 3D structures. This was made practically possible with the advent of very intense x-ray sources, such as synchrotrons. In this appendix, we describe the very basics of x-ray diffraction, focussing mainly on the aspects used in our research. We will also describe the experimental station we used at the National Synchrotron Light Source, at Brookhaven National Laboratory.

2. Bragg's law and X-ray diffraction

Consider a crystal; it has atoms sitting in well-defined, ordered positions, i.e., it has translational symmetry. If an x-ray

beam impinges on the crystal, each atom in the crystal will scatter x rays. The x rays interact strongly with the electrons of the atoms; an atomic form factor governs the details of the scattering. This atomic form factor depends on the details of the electron density around the atom, and on the angle of scatter of the x rays. The atomic form factor attenuates strongly with increasing angle; the diffracted signal has low intensity at large scattered angle.[45]

Diffraction results when constructive interference occurs between x rays scattered from different atoms. Refering to Fig. A.1, **k** is the wave vector of the incident x-ray beam, and **k'** is the wave vector of the outgoing ray. If this scattering is compared to scattering from an adjacent atom, constructive interference occurs if the path difference is an integral number of wavelengths, or:

$$d \cos \theta - d \cos \theta' = m\lambda, \qquad (A.1)$$

where θ (θ') are defined in Fig. A.1, and d is the distance between adjacent atoms. For specular reflection, $\theta = -\theta'$ and Eq. (A.1) reduces to the well-known Bragg's law ($2d \cos \theta = m\lambda$). We can re-express Eq. (A.1) in terms of the dot product between the vector **d**, which is a vector from one atom to the adjacent atom, and in terms of **n** (**n'**), where **n** (**n'**) is a unit vector in the direction of **k** (**k'**).[45] Eq. (A.1) becomes:

$$\mathbf{d} \cdot (\mathbf{n} - \mathbf{n}') = m\lambda, \qquad (A.2)$$

or mutilpying both sides by the magnitude of k:

$$\mathbf{d} \cdot (\mathbf{k} - \mathbf{k}') = 2\pi m. \qquad (A.3)$$

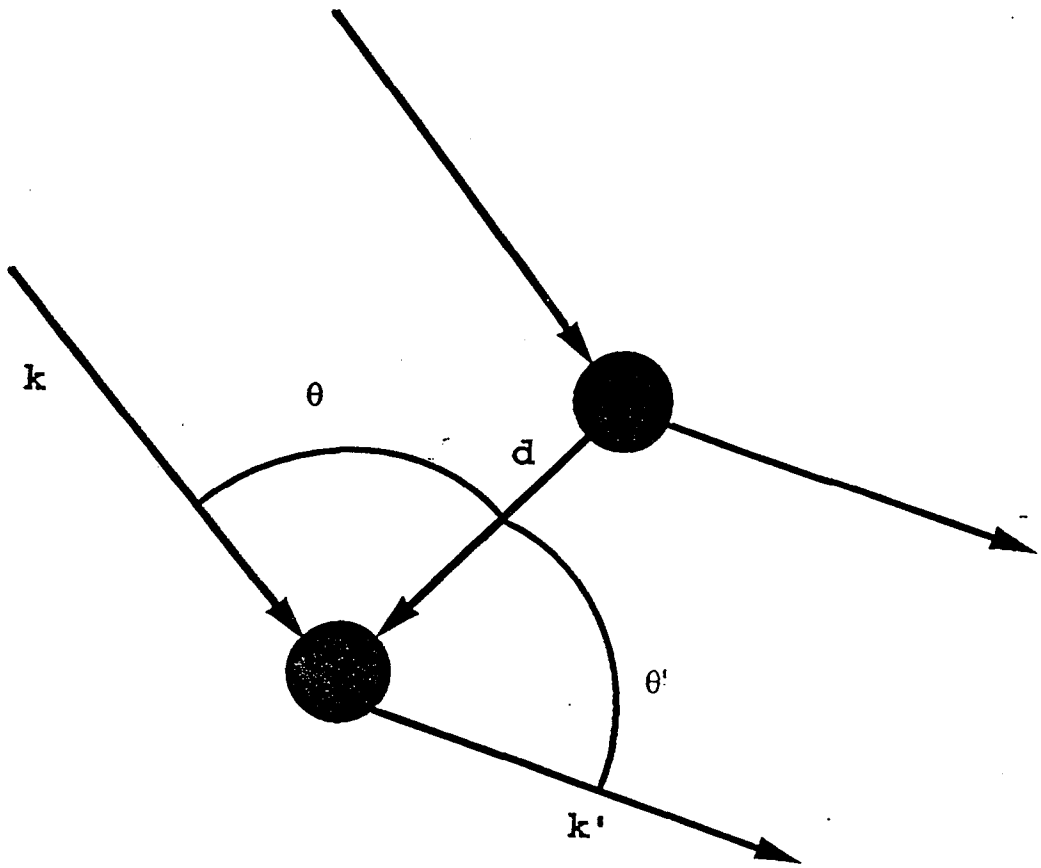

FIG. A.1. Scattering of x rays from two scatterers. Vectors k, k' and d are described in the text.

For a crystal, this equation is satisfied when (k - k′) is a lattice vector of the reciprocal lattice. Eq. (A.3) can be rewritten as the Laue conditions:

$$\begin{aligned} \mathbf{a}_1 \cdot (\mathbf{k} - \mathbf{k}') &= h' \lambda, \\ \mathbf{a}_2 \cdot (\mathbf{k} - \mathbf{k}') &= k' \lambda, \\ \mathbf{a}_3 \cdot (\mathbf{k} - \mathbf{k}') &= l' \lambda, \end{aligned} \tag{A.4}$$

where $\mathbf{a}_n$ are lattice vectors of the crystal, and h′, k′ and l′ are lattice indices.[99] The Laue conditions are satisfied exactly for an infinite number of scatterers in 3D crystal.[99]

The vector (k - k′) is given a special name, the momentum transfer, q. It has a magnitude $q = 2\pi/d$. Its name is derived from the fact that it is the change in the momentum of the incoming to outgoing wave (the momentum transferred). It is preferred over θ as the unit to specify the position of diffraction peaks because it is an inherrent property of the crystal, and does not depend on the incident radiation wavelength, like θ does.

3. Powder diffraction

For single 3D crystals, only very specific wave vectors will satisfy Bragg's law, i.e., those where q is a lattice vector of the reciprocal lattice. This leads to points in momentum space where Bragg's law is satisfied. Bragg's law is not satisfied for most incidence angles, and one must vary either the direction of the wave vector, k, or the orientation of the crystal.

One way to achieve a varying incidence angle with respect to the

crystal is to use powder samples.[45,99] The sample is made of many small crystallites, in random orientation with respect to the incident beam. The points in the diffraction pattern are spread out into cones at specific q magnitudes. The angular positions of these rings are related to the crystal plane spacing through Bragg's law. From the positions of these rings, one can construct the crystal structure of the material. Alternatively, one can measure a diffraction pattern for an unknown material, and by matching the diffraction pattern to those previously measured, identify the material. This is done in conjunction with our N_2 on graphite experiments in Chapter IV.

4. Coherence length of finite-size crystals

If we scatter x rays from a crystal with infinite size, we find that the intensity at the scattered positions is a delta function, i.e., sharply peaked at the q satisfying Bragg's Law. This is because for an infinite crystal, the Laue conditions are satisified exactly. If the crystal has a finite size, there is a relaxation in the Laue condition, and the peaks broaden from delta functions to guassian distributions.[99] Indeed, for small crystallites, the width of the peak is an analytic function of the size of the crystallite, or the coherence length, given by:[99]

$$B(2\theta) = \frac{0.94\lambda}{L\cos(\theta)}, \qquad (A.5)$$

where B is the full peak width at half of the peak maximum (FWHM) in radians, λ is the wavelength of the x rays, L is the coherence length,

and Θ is the scattering angle of the diffracted peak. Conversely, this equation can be used to determine the coherence lengths of crystals, by measuring the FWHM of the peaks diffraction from the crystal.

5. 2D powder diffraction

For 2D crystals, there is translational symmetry in only 2D, and hence only the first two of the Laue conditions (the in-plane components) are uniquely determined. The out of plane component of the incident wave can take on any value. Therefore, there is a minimum wave vector (with l = 0) which satifies the first two Laue conditions. All vectors with h and k, specified specified by the Laue conditions, and with any value l, will produce diffracted intensity. The scattered peak has an asymmetric shape, called the Warren lineshape,[99] shown shematically in Fig. A.2. The peak abruptly begins (and is maximum) at the minimum q satifiying the Laue conditions (with l = 0), and a has long tail; this is because all wave vectors above some minimum contribute to the scattering. Instrumental resolution and finite size effects broaden the both the leading edge and the tail.

The position of the maximum in the Warren lineshape specifies the minimum q to scatter, and hence specifies the lattice structure. It is this minimum wave vector which satisfies the Bragg condition, and the Laue conditions (with l = 0) in 2D. We can also use the shape of a diffracted peak to determine if the peak results from a 2D or 3D crystal structure.

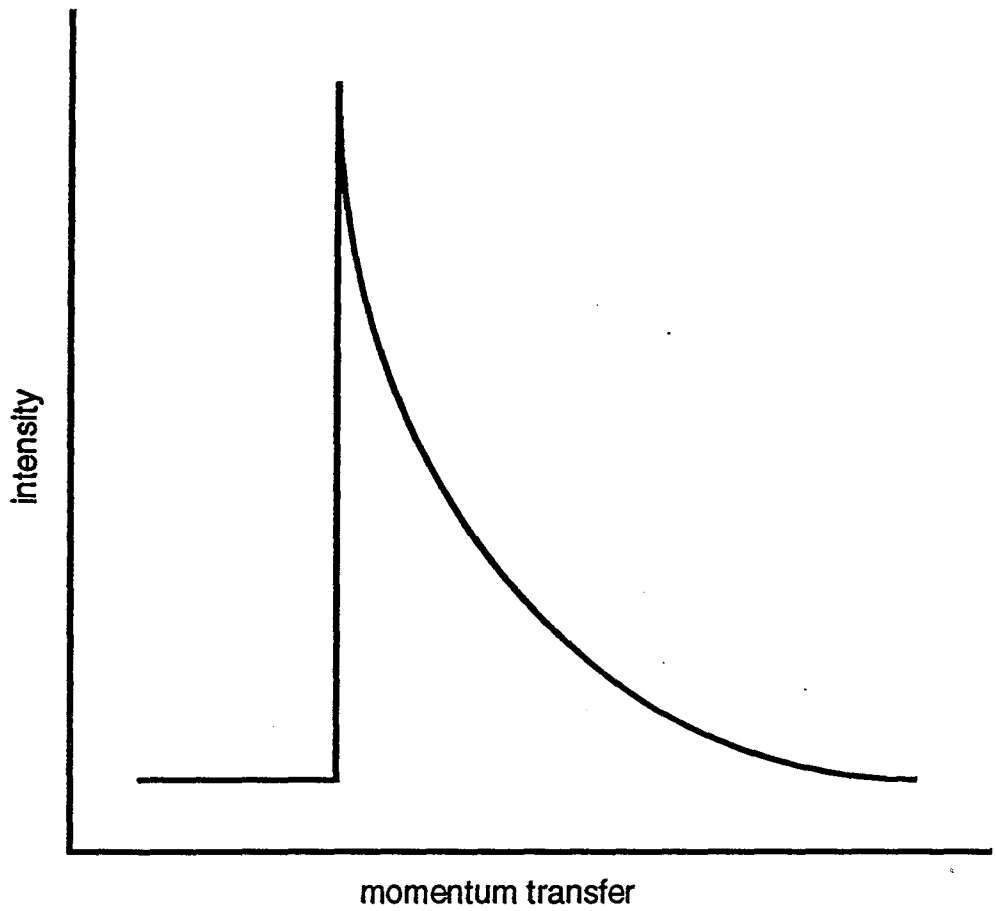

FIG. A.2. Schematic of the Warren lineshape for 2D powder diffraction peaks.

Again, the 2D coherence length of the crystal can be derived from the width of the diffracted peak. It is slightly modified fromthe form for 3D peaks. Indeed, it is:[73]

$$B(2\theta) = \frac{2.95}{L_{2D}}, \qquad (A.5)$$

where, again, B is the FWHM of the difrracted peak, and L_{2D} is the coherence length.

B. Experimental station X18A at the National Synchrotron Light Source at Brookhaven National Laboratory

The National Synchrotron Light Source (NSLS) is a broad-band x-ray source. The synchrotron x-radiation is produced by a beam of electrons traveling in a circular beam path. The radiation produced is plane polarized parallel to the floor of the facility. At each experimental beamline, the x-rays are picked off, and passed through several conditioning stages. These conditioning stages are prescribed by the type of experimental work done at each beamline.

Beamline X18A is operated by MATRIX, a consortium of mid-western universities. It is primarily used for diffuse and surface scattering, and diffraction. We used the beam to do x-ray diffraction experiments. These experiments require that a focussed, monochromatic beam is incident on the sample. In the following, we will explain the various steps taken to produce such a beam.

We begin at the x-ray source, describing the beamline

construction to the sample, which is placed inside an experimental room, called the hutch. Following Fig. A.3, we describe only the most important features. Others are listed for completeness. Photographs are included in Fig. A.4, with main features indexed as in Fig. A.3. A concrete wall (c) separates the experimental floor from the circulating electron beam. Just inside this wall, is a safety shutter (b), which blocks the x-rays; it is maintained and operated by the NSLS staff, and actuated in case of emergency. There are also vacuum valves (a and d) to isolated different parts of the beamline. A Be window (e) isolates the beamline vacuum from the electron beam vacuum. The x-ray beam then passes through a water cooled apperture (f), which determines the maximum incident flux by controlling the acceptance angle of the radiation from the ring, and which sets the horizontal divergence of the beam. From here, the beam enters the monochromator (g). The monochromator is a double crystal Si(111) monochromator, with an energy range of 4-20 keV. The beam then is focussed by a bent cylindrical platinum coated aluminum focussing mirror (h). This decreases the beam size to about 1.5 mm horizontal by 1.0 mm vertical, and increases the beam brightness by a factor of 10. Next is the photon shutter (i). This will only open if the experimental hutch has been properly secured, and will automatically close if emergency buttons are hit. Incident slits (j) fix the beam size at the sample (adjustable from zero to the maximum size set by focussing mirrors). An incident beam flux monitor (k) is used to normalize the counting times for decay of the electron beam, and hence the photon flux.

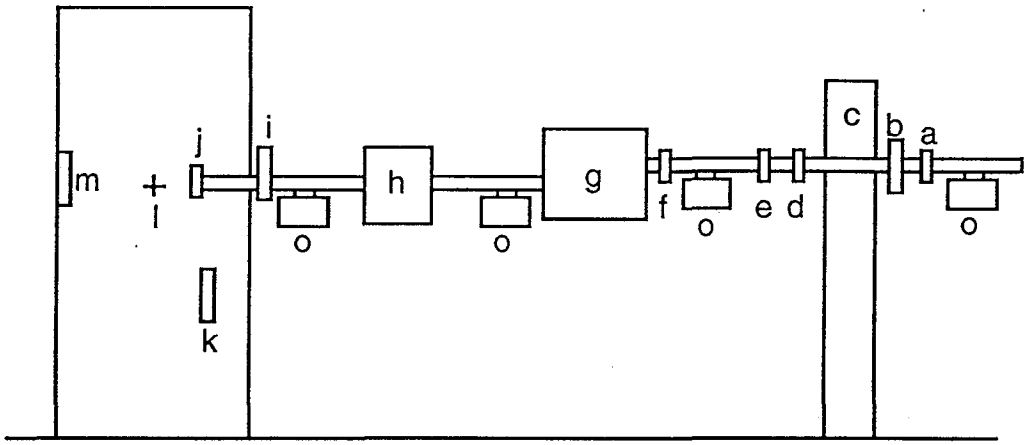

a) Fast valve
b) Safety shutter
c) Shield wall
d) Vacuum valve
e) Be window
f) Water cooled aperture
g) Monochromator box
h) Mirror box
i) Photon shutter
j) Incident slits
k) incident beam monitor
l) Diffractometer center
m) Reflected beam monitor
n) Experimental hutch
o) Ion pump

FIG. A.3. Schematic of beamline X18A at NSLS.

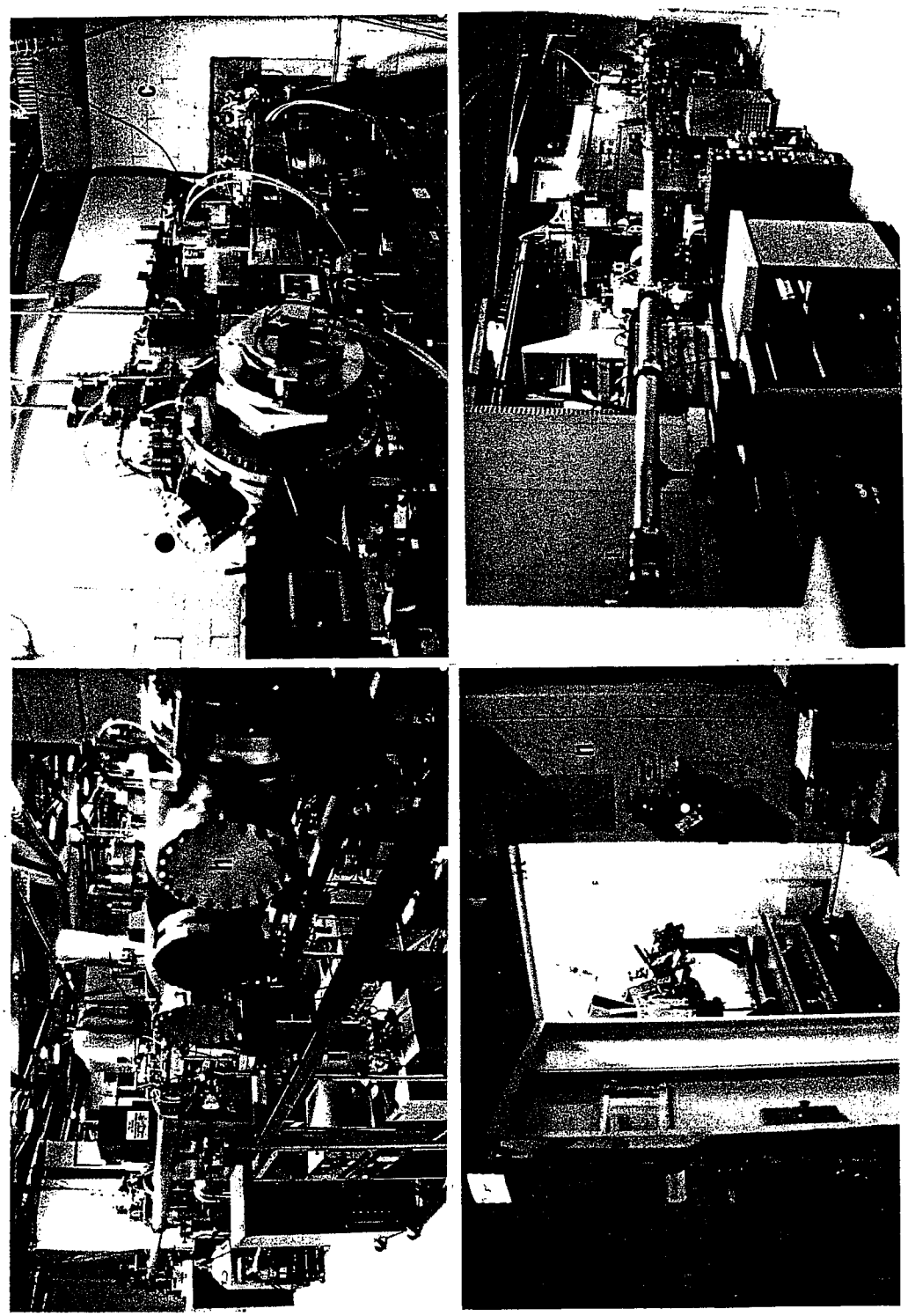

FIG. A.4. Photographs of X18A beamline. Labels defined in Fig. A.3.

The beam is focussed to the center of a 50 cm 4-circle diffractometer (Huber Model 5020 Diffractometer), pictured in Fig. A.5. The diffractometer allows the orientation of the sample to be adjusted in all three Eulerian angles, and for movement of the detector through 2θ. The sample is mounted on the end of a cold finger (see Fig. A.6), which is enclosed in a cryostat cooled by a closed cycle helium refrigerator. The cryostat is fitted with Be windows (see Fig. A.5) to allow the x-ray beam access to the sample. The cryostat is mounted on the diffractometer (Fig. A.5), with the sample rotated 5° from the perpendicular to the plane of the floor (see Fig. A.5).

Diffraction scans are done in a transmission geometry. This is shown schematically in Fig. A.7. The incident beam (a) passes through the sample (b) and leaves the sample at some angular position, 2θ. The beam enters a helium flight path (c). Soller slits (d) resolve the beam to 0.02 $Å^{-1}$. The detector is stepped through 2θ, the range and stepsize of which is determined by the user. The detector moves about an axis perpendicular to the incident beam and parallel to the floor.

The cryostat maintains a sample temperature between 10 and 300 K ± 0.1 K. We used two different sample cells for our experients. The graphite sample cell is a copper block 1.2 cm thick, with 1.9 cm diameter graphite disks enclosed by Be windows. A capillary allows sample dosing. The MgO cell is described in detail in the text (Chapter III, Sec. C) and pictured in Fig. III.1.

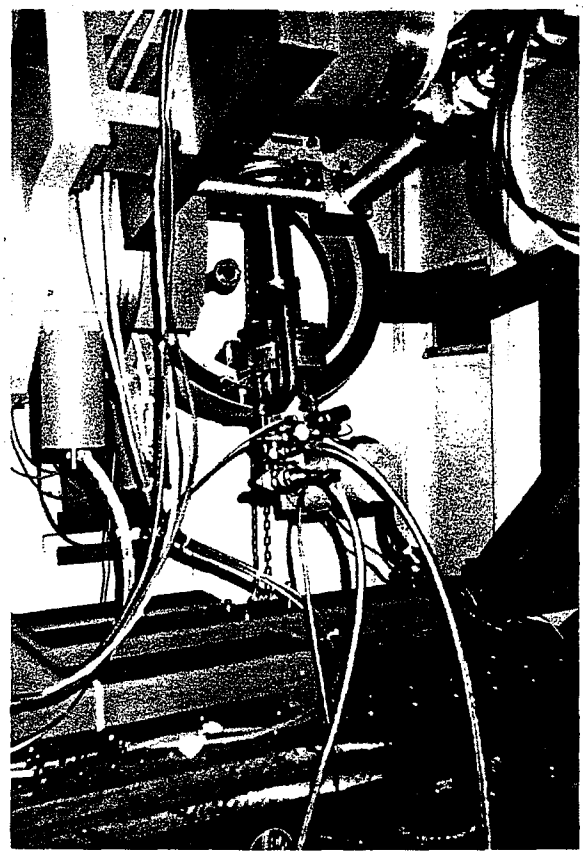

FIG. A.5. Photograph of the Huber diffractometer.

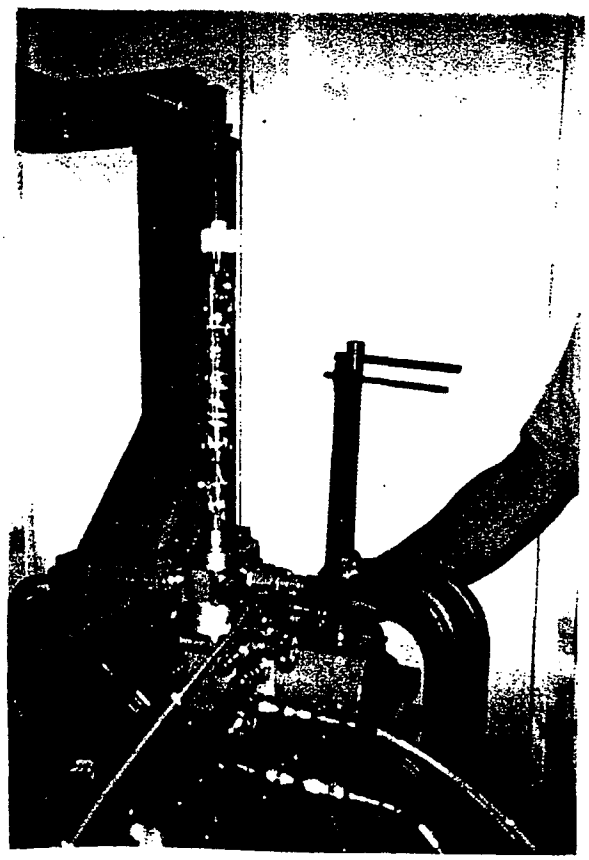

FIG. A.6. Photograph of sample cell mounted on cryostat.

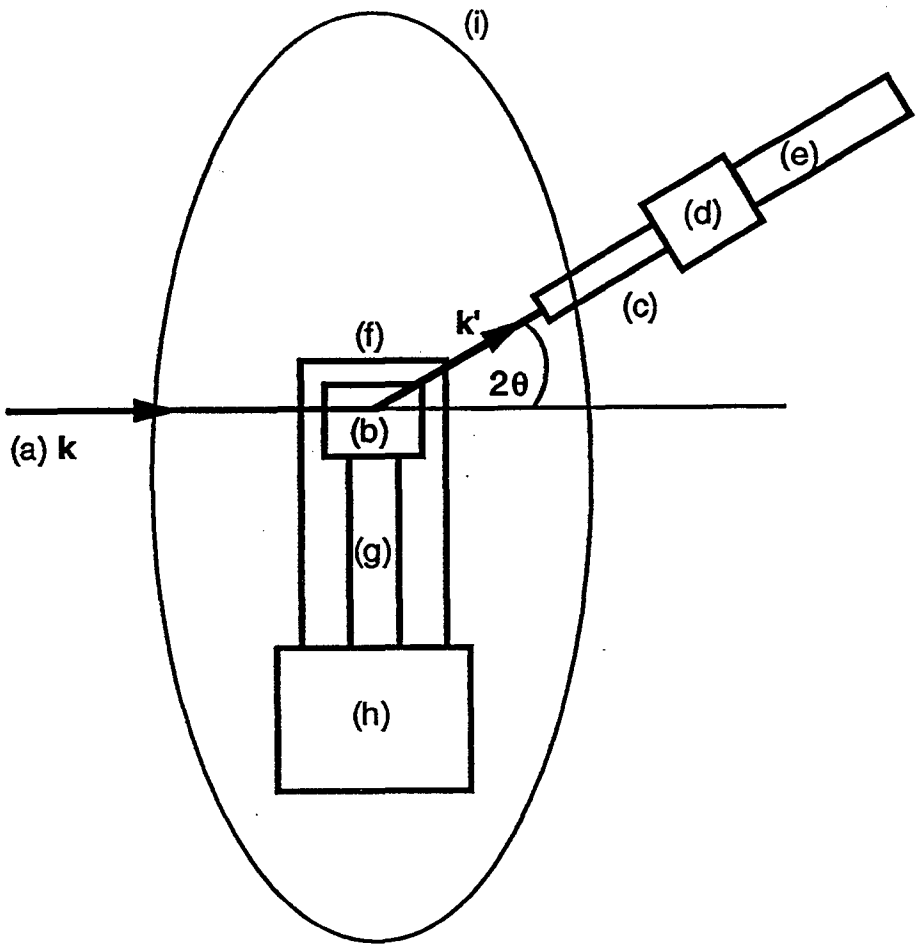

FIG. A.7. Schematic diagram of scattering geometry. The x-ray beam (a) hits the sample (b), and scatters. The scattered beam enters a helium flight path (c), Soller slits (d), and is recorded by the detector (e). The sample (b) is mounted inside on a cold finger (g), vacuum isolated by a Be window (f). The cryostat (h) is mounted inside a Huber diffractometer (i).

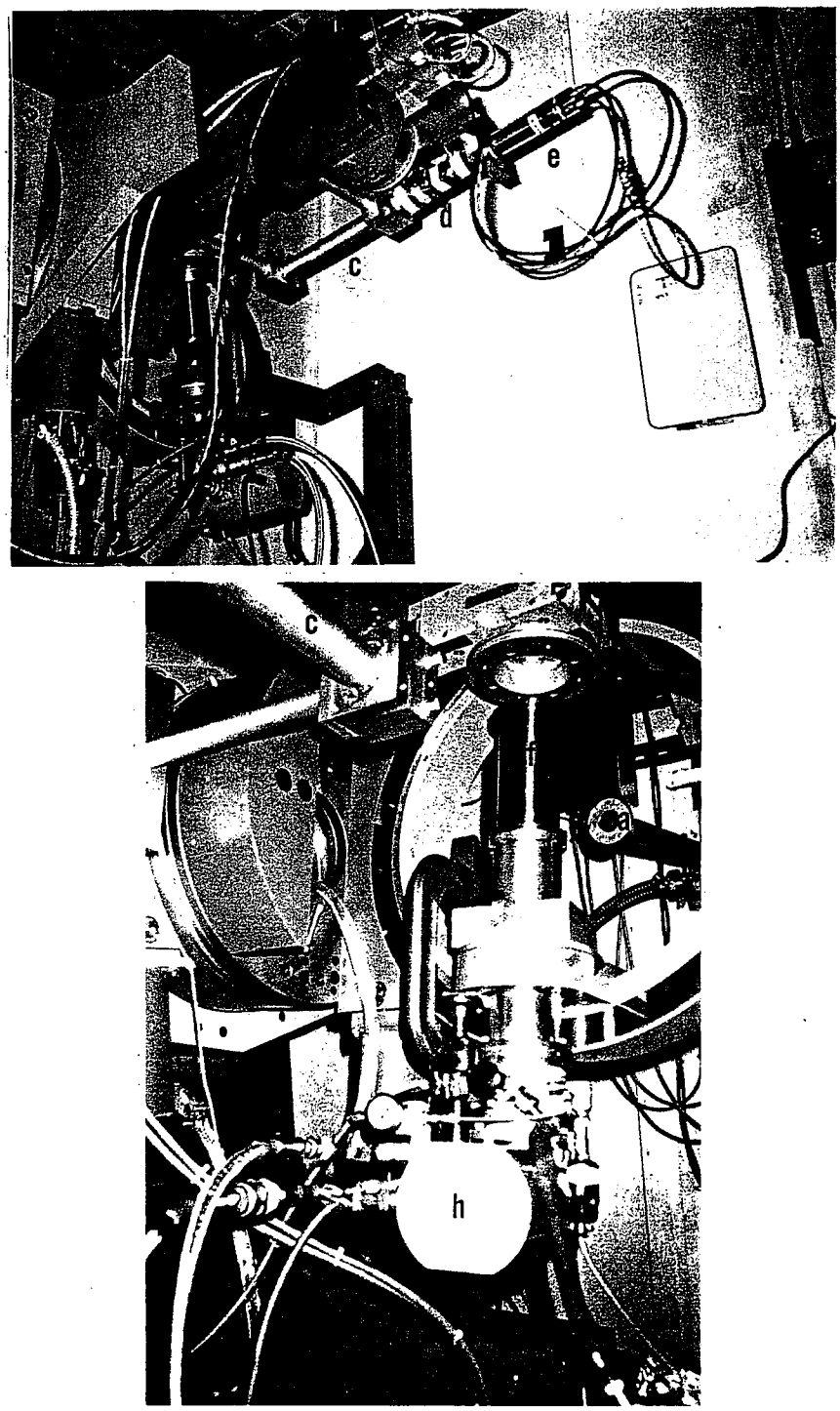

FIG. A.8. Photographs of scattering geometry. Labels are the same as for Fig. A.7.

APPENDIX B

AUTOMATED GAS HANDLING SYSTEM

A. Theory of vapor pressure isotherms

1. Thermodynamic considerations

We begin by briefly reviewing the thermodynamic model of adsorption. Consider the substrate to be a lattice of adsorption sites, where it is energetically favorable for molecules to adsorbed (see Chap. I, Sec. B.2). It is a simple exercise to derive the chemical potential of the adsorbed film at constant temperature (see. e.g., Ref. 29):

$$\mu_{film} = k_B T \ln \frac{\theta}{1-\theta} \tag{B.1}$$

where θ is the coverage of the film, k_B is Boltzmann's constant, and T is the temperature. The adsorbed film is thermal and diffusive equilibrium with the 3D gas phase of the adsorbate above the substrate. We equate the chemical potential of the adsorbed film to the chemical potential of the 3D gas:

$$\mu_{gas} = k_B T \ln \left(\frac{P}{P_o}\right) \tag{B.2}$$

where:

$$P_o = (k_B T)^{\frac{5}{2}} \left(\frac{2\pi m}{h^2}\right)^{\frac{3}{2}} \tag{B.3}$$

where m is the adsorbate mass, P is the pressure and h is Planck's constant.[29]

We can easily measure (described in the next section) the pressure versus the number of atoms adsorbed for an isothermal path. From these measurements we can calculate μ_{gas} ($=\mu_{film}$) along this isothermal path. In this way we gain information about the adsorption characteristics of the adsorbed system.

We can also probe the system for phase transitions by studying the change in the Gibbs free energy:

$$G_o - G(P) = PV_o \ln\frac{P_o}{P} \tag{B.4}$$

where G_o is a reference free energy (the free energy of the system at saturation), G(P) is the free energy at pressure P, P_o is the saturation pressure, and V_o is the volume in the system (i.e., the gas handling system volume). If a phase change occurs, this is evident as a discontinuity in the derivative of the Gibbs free energy.[111] Isotherms can be used to measure the isothermal compressibilty, according to the equation:[112]

$$K_T = n^{-2}\frac{\partial n}{\partial \mu} \tag{B.5}$$

where n is the number adsorbed.

Isotherms can also be measured at several different temperatures, and the chemical potential versus T can be plotted.[9] From measurements of isotherms at several temperatures, the isosteric heat of adsorption for specific coverage can be measured, using the Clausius-Clapeyron equation:[73]

$$q_{st} = -R\left[\frac{\partial \ln P}{\partial\left(\frac{1}{T}\right)}\right]_{\theta} \qquad (B.6)$$

where R is the gas constant, and the subscript θ denotes constant coverage. Indeed, myriad thermodynamic information for a system can be derived from isotherm data. For a good example of information available from experimental measurement of vapor pressure isotherms, see, e.g., Refs. 1, 86, and 112.

2. Measurement of a vapor pressure isotherm

We now review the basic measurement of a vapor pressure isotherm. A known amount of 3D adsorbate gas is allowed to come into thermal and diffusive equilibrium with a cold substrate. Gas molecules will adsorb to the substrate, and leave the 3D gas phase. The difference in the amount of gas in the 3D gas phase before equilibration and after is the number of molecules adsorbed to the surface.

Quantitatively, the process proceeds as follows. We begin with an empty gas handling system (ghs), with a known volume (V_{ghs}) at constant temperature (T_{ghs}, approximately room temperature) [see Fig. B.1 (b)]. We admit adsorbate gas molecules from a reservior into V_{ghs} [see Fig. B.1 (a)] to some pressure (P_i). The number of molecules in V_{ghs} is calculated from the ideal gas law. We then open up the gas handling system to the cold sample at T_{sample} [see Fig. B.1 (c)], and gas molecules adsorb. The number of gas molecules adsorbed is the difference in the number in the gas phase before and the number in the

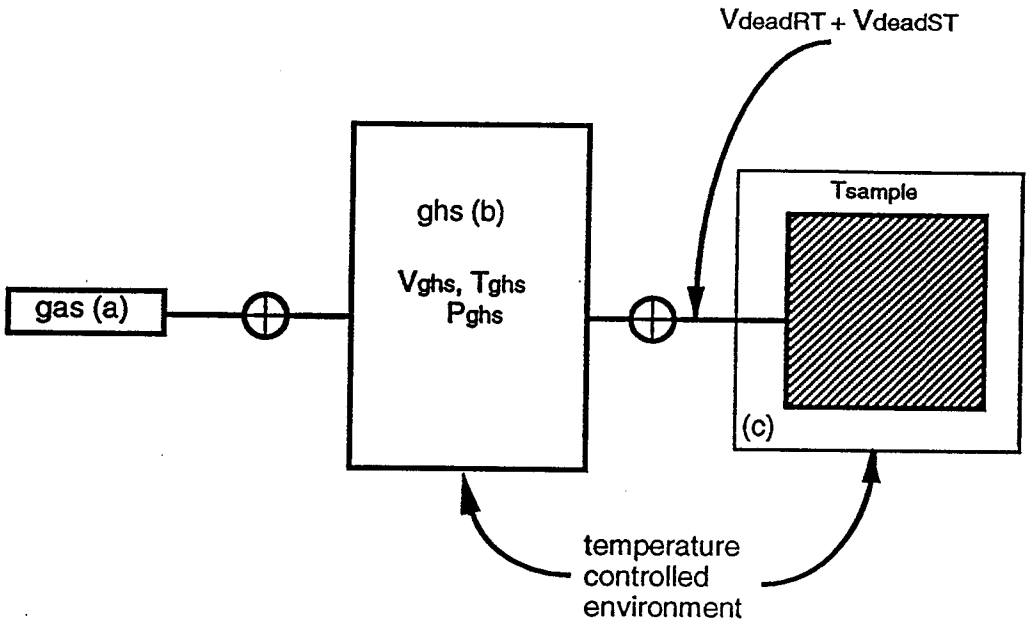

FIG. B.1. Schematic diagram of gas handling system (ghs). Gas is admitted from gas reservoir (a) into ghs (b). The ghs is then opened to the sample cell (c).

gas phase after the valve is opened. When we open up the valve to the sample, we increase the volume accessible to the 3D gas by an amount we denote V_{dead}, which is the sample cell volume not occupied by sample, plus the volume in any connecting tubes from the gas handling system to the sample chamber.We further split V_{dead} into V_{deadRT} and V_{deadST}; V_{deadRT} is the part of the dead volume at room temperature, and V_{deadST} is the part of the dead volume at the sample temperature (see Fig. B.2). The number adsorbed for the first iteration of gas adsorption is:

$$N^1_{ads} = N_{ghs_i} - (N_{ghs_f} + N_{deadRT} + N_{deadST}) \tag{B.7}$$

We can re-express this in terms of the intial and final pressure, P_i and P_f:

$$N^1_{ads} = P^1_i X_{ghs} - P^1_f X_{ghs} - P^1_f X_{deadRT} - P^1_f X_{deadST} \tag{B.8}$$

where:

$$X_y = \frac{V_y}{k_B T_y} \tag{B.9}$$

This is iterated again, i.e., we add more gas to the system and allow it to adsorb and come into thermal and diffusive equilibrium with the 3D gas. The total number adsorbed is then:

$$N^{tot}_{ads} = N^1_{ads} + N^2_{ads} \tag{B.10}$$

where N^2_{ads} is calculated in the same way as N^1_{ads}. Successive gas admission and application of Eq. (B.8) leads to the general formula for the amount of gas adsorbed after n steps:

$$N_{ads}^{n}=\left[\sum_{m=1}^{n}(P_i^m-P_f^m)X_{ghs}\right]-P_f^n(X_{deadRT}+X_{deadST}) \qquad (B.11)$$

An isotherm is plotted by graphing the pressure on the x-axis and the number adsorbed on the y-axis. The thermodynamic data described in the last section can be obtained by the proper data reduction.[1,73,86,111,112]

B. Automated gas handling system

1. Motivation

Vapor pressure isotherms have been used for many decades to study gas adsorption. It is fairly easy to build a system capable of doing gross measurements of adsorption features, such as isotherm shape to test sample heterogeneity (see Sec. III.D), to measure sample specific surface area (see Secs. IV.C and III.D), and to perform global phase diagram surveys. In order to be able to distinguish subtle changes in thermodynamic variables, a very accurate (and precise) system is needed, such as the system detailed by Suter *et al.*[112]

Many steps were taken in building the Suter *et al.* system to ensure accuracy. Pressure sensors were chosen which have a statistical uncertainty of $\approx 10^{-5}$ P_{fs}, where P_{fs} is the full scale pressure, for pressures less than 10 Torr, and $\approx 10^{-4}$ P_{fs} for pressures above 10 Torr, using a 1000 Torr capacitance manometer. The absolute uncertainty is reduced three orders of magnitude if a 1 Torr manometer is employed in their system. The capacitance manometers are

temperature controlled to 0.01 K, to minimize pressure drifts due to temperature. The Suter *et al.* ghs also includes very tight temperature control for both the sample and the ghs environment (± 0.01 K) to ensure a truly isothermal path. The system is built so that surface heterogeneity of the sample is the limit to how sharp steps in the isotherm are, and also limits the smallest reasonable step in the number adsorbed (for a complete description, see Ref. 112).

The system is computer controlled, i.e., system pressures and temperatures, are monitored and recorded by a computer. This allows low-noise pressure readings by computer averaging over many pressure readings. The analog data is converted to digital data and stored by a 18 bit DAC (Analog Devices 1138). The computer also admits gas into the system after each sucessive step, and opens the ghs to the sample. Equilibration of the system can be quantitatively determined (i.e., stability criteria established and used to determine equilibration), hence eliminating exprimentor impatience from degrading data. The system can be used to take data continuously over the life of an isotherm (computers need no sleep, while graduate students need some occasionally), making fine resolution stepsize, and multilayer isotherms experimentally feasible.

2. Design of USU automated gas handling system

We are interested in building a system which incorporates many of the features found in the Suter *et al.* system, and hence there are

many similarities. In this section, we describe our system, which is still in development. We begin with a description of the hardware, and conclude with a breif description of the system software.

Fig. B.2 is a block diagram representing the main gas manifold, which includes the computer-controlled valves and computer-monitored sensors. All letters in parentheses this and the next 3 paragraphs refer to Figure B.2. The automated ghs (aghs) is built out of mainly 1/8" NPT stainless steel (ss) pipe fittings. The central piece, however, is a welded ss cross. Three pneumatically activated Nupro air actuated bellows valves (Model SS-4BK-TH3-1C) (g,l,h) are welded to the cross. These are activated by 40 psi pressure, delivered by copper tubing (not represented). The fourth port on the cross opens directly to the gas manifold. The gas manifold is constructed from 1/8" NPT ss pipe fittings. Attached are a relief valve (Nupro Model SS-4CPA2-3) (a), and two pressure gauges (b,d, described in detail below). One pressure gauge is an absolute pressure gauge (d). The second pressure gauge is a differential pressure gauge (b, low pressure gauge). The differential pressure gauge can be isolated from the manifold by a manual needle valve (c). The reference vacuum is provided by a 1/8" ss tube (e) connected to the vacuum port. The pressure gauges are attached to the system via UltraTorr Cajon Quick Connectors.

The vacuum port (f) is isolated from the gas manifold via a pneumatic valve (g). The reference vacuum tubing for the differential

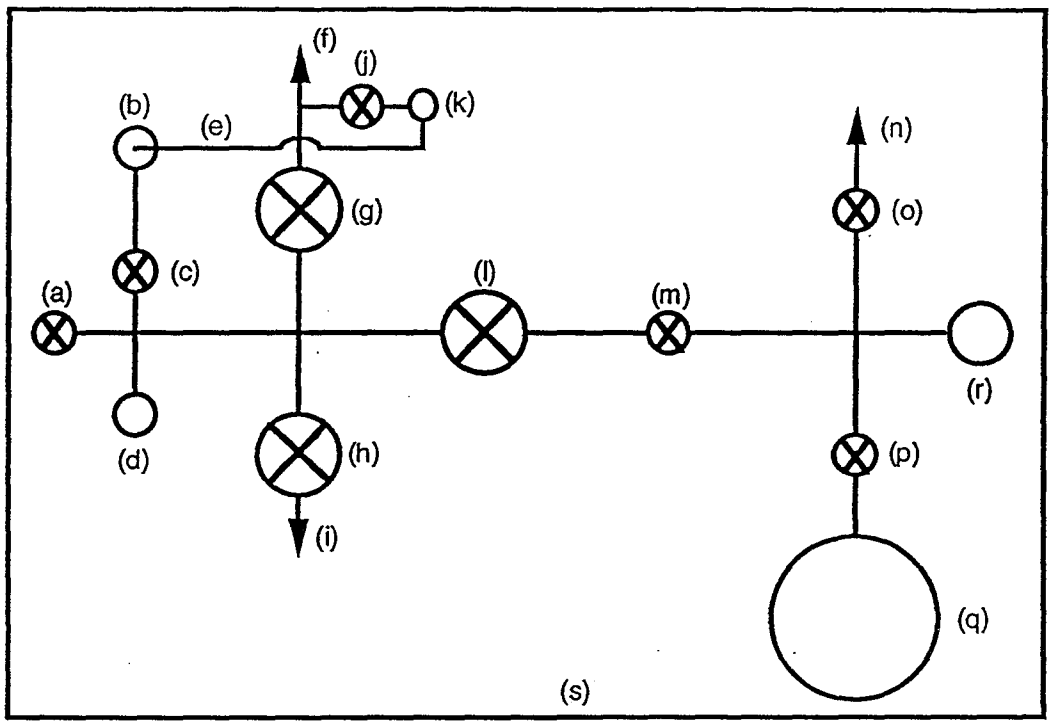

FIG. B.2. Schematic diagram of the USU automated gas handling system manifold (aghs). The components are as follows: (a) relief valve; (b) low (differential) pressure head; (c) valve for differential pressure head; (d) high (absolute) pressure head; (e) reference vacuum line; (f) vacuum port; (g) pneumatic valve to vacuum; (h) pneumatic valve to sample port; (i) sample port; (j) valve for reference vacuum line; (k) reference vacuum port; (l) pneumatic valve for gas supply to agh; (m) gas flow regulator needle valve; (n) gas input port; (o) gas input valve; (p) valve for standard volume; (q) standard volume; (r) vacuum TC gauge; (s) foam insulation.

pressure head is isolated from the vacuum port by a manually controlled needle valve (j). The reference vacuum tubing is attached to the system via UltraTorr Cajon Quick Connectors (k).

The sample port (i) is also isolated from the gas manifold via a pneumatic valve (h). The sample cell is connected to the aghs by a 1/8" ss capillary tube. The sample cell system is described below.

The third pneumatic valve (l) isolates the gas input system from the gas manifold. The gas input to the manifold must be carefully monitored, so the gas input port is designed to leak gas into the gas manifold. This is achieved by a needle valve (Nupro M-2MG4) which can be just cracked open (m) allowing very restricted flow of gas. Also attached to the gas input system is a gas input port (n), which can be manually valved off (o), a standard volume (q) and accompanying valve (p), and a vacuum thermocouple (VTC) gauge (r). The entire system is enclosed in a foam box (s) for temperature stability.

The gas manifold system is part of a larger system, shown schematically in Fig. B.3. The temperature of the aghs [Fig. B.3 (b)] is controlled by a RFL 70-115 proportional temperature controller [Fig. B.3 (a)]. It uses a YSI 44004 thermistor to detect temperature changes, and delivers a variable current proportional to the difference in the measured temperature and set temperature to two 150 Ω heaters inside the aghs foam box. The controller is capable of controlling temperatures to ± 0.05 K. The temperature of the aghs is set to slightly above room temperature (≈ 305 K). The temperature of the system is recorded by the computer, as read from a second similar

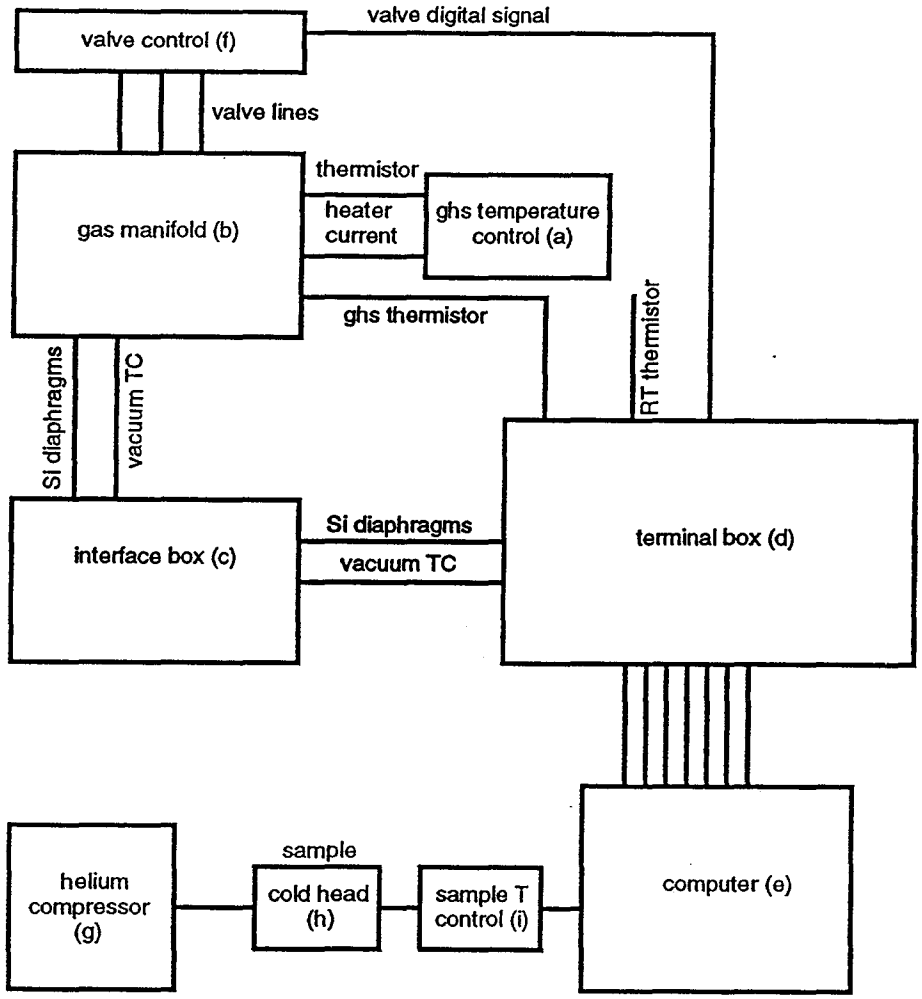

FIG. B.3. Schematic of the automated vapor pressure isotherm system. The components are as follows: (a) ghs temperature control; (b) aghs gas manifold; (c) interface box; (d) terminal box; (e) computer; (f) valve control box; (g) helium compressor; (h) cold head; (i) sample temperature controller.

thermistor. Another similar thermistor also measures the room temperature. These two thermistors are connected to the computer through the terminal box [Fig. B.3 (d), described in detail below].

Other system sensors are connected to the computer through both an interface box [Fig. B.3 (c)] and a terminal box [Fig. B.3 (d)]. The VTC is connected to a gauge meter mounted on the front of the interface box. The output voltage (proportional to the pressure) is read from the gauge; this is passed from the interface box to the terminal box. The pressure in the aghs is monitored by two Si diaphragm pressure transducers. Pressures to 1500 Torr are measured by a Nova Sensor NPH-5-200-AH absolute pressure transducer. Low pressures (to 18.75 Torr) are measured by a Nova Sensor NPH-5-2.5-AD. This sensor is a differential pressure sensor; actually, it could be used to measure pressure differences to 18.75 Torr. However, the reference port is connected to a vacuum port (see Fig. B.2), and therefore the sensor is only used to measured pressure differences from vacuum in our current configuration. Both pressure sensors are excited by a 1.5 mA constant current source, mounted on a small circuit board within the temperature controlled environment of the aghs (to minimize current drifts due to temperature variations). The output voltage of each sensor is interfaced to the computer through the interface box and the terminal box. The accuracy of the sensors is a complicated function of the accuracy of the temprature, the constant current source electronics, and the ADC board; this is detailed in the next section on the system accuracy.

We chose these pressure sensors over conventional capacitance manometers for two reasons. First, they are considerably smaller (about 1 cc dead volume) than capacitance manometers (about 20 cc dead volume). Since the accumulated error in the number adsorbed is directly proportional to the gas handling system volume (See Ref. 112 for complete development), minimizing the aghs volume increases the accuracy of the system at high coverage. Secondly, capacitance manometers are about $1000 and the Si diaphragm pressure transducers cost about $50. The Si sensors are easily interchangable, and the price makes it feasible to purchase a variety and to choose the one most appropriate for each application. In theory the Si sensors are as accurate as the capacitance manometers (quantified below; see Sec. B.3), provided the control electronics and data collection devices have sufficient accuracy.

The opening and closing of the pneumatic valves is controlled by digital I/O from the computer. A digital high closes a solid state relay, which opens a three-way solenoid valve between the pneumatic valve and a 40 psi pressure source. This pressure actuates the pneumatic valve. The solenoid valves and the control electronics are situated in the valve control box [Fig. B.3 (f)]. Copper tubing runs from the box to the pneumatic valves. The solid state relays are connected to the terminal box.

Sample low temperature is achieved by a closed cycle helium refrigerator [Fig. B.3 (f), Varian Cryocompressor] and cryostat [Fig. B.3 (g), a modified Varian cryopump]. The interior of the cyrostat is

shown schematically in Fig. B.4. The cold stage consists of two parts: the 77 K stage [Fig. B.4 (a)], to which we attach a radiation shield [Fig. B.4 (g)]; and the sample stage [Fig. B.4 (b)], to which we attach a copper block extension [Fig. B.4 (c)]. This oxygen-free high-conductivity (OFHC) copper extension houses two rod heaters for temperature control, and a 1000 Ω platinum RTD. The sample holder [Fig. B.4 (d)] mounts on the copper extension. Sample cells [Fig. B.4 (e)] slide into the sample holder and are held in place by set screws. A Si diode thermometer (Lakeshore Model DT-470-SD-13) is mounted to the bottom of the sample cell. This diode is the sensor used by the temperature controller (described below) to monitor andmaintain sample temperature. A capillary tube [Fig. B.4 (f)] is welded to the top of the sample cell, which is sealed with two 1.33" conflat flanges, and a copper gasket. A small heater and a thermocouple clamps to the capillary; this is to prevent gas condensation in the capillary by mildly heating the capillary. The entire system is enclosed inside a ss vacuum container [Fig. B.4 (h)], and sealed with a 8" Viton o-ring [Fig. B.4 (i)].

Sample temperature control [see Fig. B.3.(i)] is maintained by an RMC CR-31 temperature controller. It can read and display two sensors (a Si diode and a 1000 Ω platinum RTD). It puts out a 0 to 1A current which is proportional to the deviation between the measured sample T and the user specified set-point temperature. In our application, we control the sample temperature from the Si diode thermometer by regulating the current to the heaters housed in the

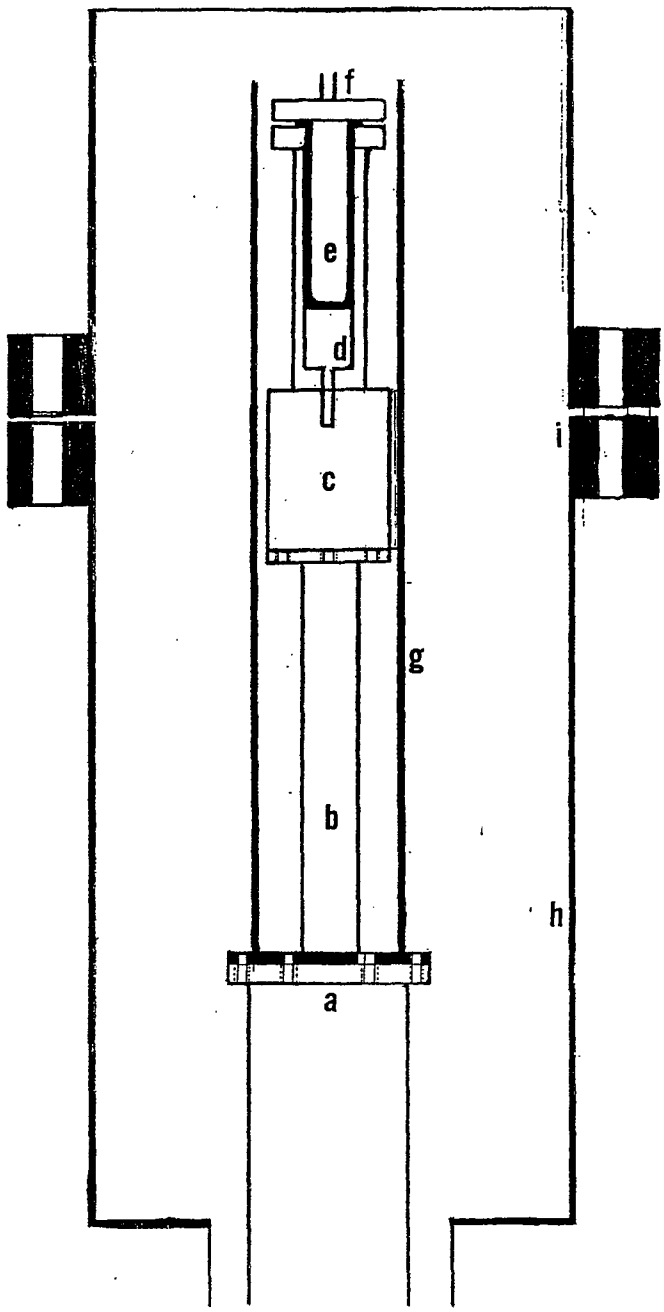

FIG. B.4. Schematic of inside of cryostat. The components are as follows: (a) 77 K stage; (b) cold stage; (c) copper extension; (d) sample holder; (e) sample cell; (f) capillary tube; (g) radiation shield; (h) ss vacuum shroud; (i) Viton o-ring vacuum seal.

copper extension [see Fig. B.4.(c)]. The controller can maintain temperatures from 1.4 K to 475 K ± 0.1 K in this configuration. The controller can also ramp temperatures. The controller is interface directly to the computer through an RS-232 port.

The terminal box [Fig. B.3 (d)] contains a Data Translations DT707 screw terminal. This interfaces directly to the Data Translations DT2811 A/D board inside the computer. The screw terminal is a convenient connection for the 5 input A/D channels, and 3 digital outputs for the valves. In total, the DT707 can accomomdate 16 single ended input A/D channels or 8 differential input A/D channels, 8 digital outputs and 8 digital inputs. Analog input and output has 12-bit resolution.

The DT 2811-PGL A/D board is located in a expansion slot inside a 286 PC. It is a 12-bit, half-size board, capable of analog to digital conversion (A/D), digital to analog conversion (D/A), and digital input and output (I/O). It has jumper selected voltage ranges of 0-5 V, ± 5 V, and ± 2.5 V (we use ± 5 V), a programmable gain (for each channel) of 1, 10, 100, or 500, and can accept data at a maximum rate of 2.5 kHz. Board function is controlled by software; the specific system drivers (i.e, board initialization, and voltage recording on specific channels, etc.) are provided by Data Translations, and are incorporated into our aghs control software. We currently use the A/D board to monitor room temperature, aghs temperature, the differential head pressure, the absolute head preassure, and the VTC.

Control of the aghs (i.e., recording data, or controlling valves) for performing an isotherm is provided by a computer prgoram, written by members of our lab (still in development, see Ref. 113). The program also controls the RMC sample temperature controller. When completed, the control software will allow user input of experimental variables (i.e., sample temperature, equilibrium pressure at which to end isotherm, stepsize in pressure, etc.), initialize and control hardware, and make calculations of N_{ads} from the measured final pressures, and display data in real time.

3. Error Analysis

We are now interested in determining the theoretical system accuracy, i.e., what is the error in the number adsorbed for a measurement at a given pressure. The error in the number adsorbed is the error for Eq. (B.11) (see derivation Ref. 114). For simplicity, we represent the sum over the difference in the intial and final pressure with P^n_{dif}. The error in the number adsorbed for each iteration is given by:

$$\frac{\delta N^n_{ads}}{N^n_{ads}} = \frac{\delta N^n_p + \delta N^n_v + \delta N^n_t}{N^n_{ads}} \qquad \text{(B.12)}$$

where:

$$\frac{\delta N_p^n}{N_{ads}^n} = \frac{\delta P_{dif}^n}{P_{dif}^n} + \frac{\delta P_f^n}{P_f^n}\left(\frac{V_{deadRT}}{V_{ghs}} + \frac{V_{deadST}T_{ghs}}{V_{ghs}T_s}\right) \tag{B.13}$$

$$\frac{\delta N_v^n}{N_{ads}^n} = \frac{\delta V_g}{V_g} + \frac{P_f^n}{P_{dif}^n}\left(\frac{\delta V_{deadRT}}{V_{ghs}} + \frac{\delta V_{deadST}T_{ghs}}{V_{ghs}T_s}\right) \tag{B.14}$$

$$\frac{\delta N_t^n}{N_{ads}^n} = \frac{\delta T_g}{T_g}\left(1 + \frac{P_f^n}{P_{dif}^n}\frac{V_{deadRT}}{V_{ghs}}\right) + \frac{\delta T_s V_{deadST} P_f^n}{T_s V_{ghs} P_{dif}^n} \tag{B.15}$$

where each term is defined in relation to Eq. B.11 and δ denotes the error.

Each term in the error represents the error in the number adsorbed due to the error in the three experimetally measured quantities: the pressure (δN^n_p), the temperature (δN^n_t), and the volumes (δN^n_v). We discuss each term separately.

δN^n_t represents the error due to error in the measurement of the aghs and sample temperature. In the previous section, we state that the aghs system temperature is controlled to ± 0.05 K and the sample temperature to ± 0.1 K. We estimate the sample temperature (T_s) to be 77 K (± 0.1%) and the room temperature (T_{RT}) to be 305.56 K (± 0.02%). For the purpose of error analysis, we also estimated the aghs system temperature to the same as room temperature ($T_{RT} = T_{ghs}$). The error $\delta N^n_t/N^n_{ads}$ is ≤ 0.03%, and is dominated by the error in the aghs temperature.

The error in the number adsorbed δN^n_p is due to error in the volume of the aghs and the dead volume. We have not yet made accurate determination of the aghs volume. However, we have determined

accurately the volume of the stainless steel volume in the aghs [see Fig. B.2 (q)].[115] We use this volume and associated error [V_{ghs} = 40.000 ± 0.015 cc (± 0.04%)]. We estimate the dead volume at room temperature [V_{deadRT} = 4.000 ± 0.001 cc (± 0.03%)], and at sample temperature [V_{deadST} = 3.500 ± 0.009 cc (± 0.03%)] to be the same as that calculated for the manual system used to measure the isotherm shown in Fig. III.3. This estimation introduces neglible error to the the final calculation, as the dead volumes are themselves a small correction. The error in these volumes is overestimated, as the error in the pressure in the manual system (used to measure these volumes) is significantly higher than in the aghs. The error $\delta N^n_v/N^n_{ads}$ is ≤ 0.04%, and is dominated by the error in the V_{ghs}.

The error in the pressure measurement is a complicated function of the control electronics error, the Si diaphragm error, and the data collection error, i.e., the A/D board error.[115] The error in the measured pressure is given by:

$$\frac{\delta P}{P} = \frac{\delta P_{Si}+\delta P_{el}+\delta P_{A/D}}{P} \qquad (B.16)$$

where δP_{Si} is the error due to the error in the Si diaphragm (this is the theoretical limit to the error in pressure), δP_{el} is error in the control electronics (e.g., the drift in the constant current supply due to temperature), and $\delta P_{A/D}$ is error due to analog to digital recording and conversion. Careful analysis of each of these contributions (see Ref. 115) yields:

$$\frac{\delta P_{Si}}{P} = \frac{10^{-5}V}{V_s} \qquad \frac{\delta P_{el}}{P} = \frac{10^{-4}V}{V_s} \qquad \frac{\delta P_{A/D}}{P} = \frac{2x10^{-4}V}{V_s} \tag{B.17}$$

where V_s is the output voltage of the sensors (in volts); $\delta P_{Si} \approx 2$ mTorr for the differential head, and $\delta P_{Si} \approx 200$ mTorr for the absolute head.

The largest contribution to the error in the pressure due to electronics δP_{el} is from the temperature response of the resistors in the control circuit. δP_{el} is easily lowered by a factor of 50 or greater by replacing the carbon resistors with metal film resistors; this is planned. After replacing the resistors, $\delta P_{el} < \delta P_{Si}$.

The error in the pressure due to A/D conversion, $\delta P_{A/D}$, is the largest contribution to the system error. This is currently the limiting factor in the accuracy of our pressure measurements. This can be reduced by a factor 16 by replacing our 12 bit board with higher resolution 16-bit board. Future plans include this replacement. After installation of the 16-bit board, $\delta P_{A/D} \approx \delta P_{Si}$.

We now estimate the error in the number adsorbed based on the system error estimates given in the previous few paragraphs. To estimate this, we use data collected for an isotherm measured on the manual system. This is useful for two reasons. First, it gives us an idea of the error over an entire isotherm, including accumulated error. Second, we can compare the error of the aghs to the manual system.

Using the differential head, we find that the error in the first data point $\delta N^1_{ads} = 0.1\%$ of N_{ads} ($P_f = 0.028$ Torr) and the error after

30 data points δN^{30}_{ads} = 0.4% of N_{ads} (P_f = 6.22 Torr). The error calculated for the manual system is δN^{1}_{ads} = 0.6% of N_{ads} (P_f = 0.028 Torr) and the error after 30 data points δN^{30}_{ads} = 1.3% of N_{ads} (P_f = 6.22 Torr). For the Suter *et al.* system, we estimate the error to be 0.01% for the 30th data point.[112]

We are a factor of 40 less accurate than the Suter *et al.* system. We now analyze the contributions to this error, to see where we can improve our system. For the high pressure sensor, the largest contribution (by a factor of 20) is the error due to δN_p [see Eq. (B.12)]. This can be lowered by a factor of 16 by using a more accurate 16-bit A/D board. Replacing the resistors in the constant current supply reduces δN_p further as noted above, and this error becomes limited by the intrinsic uncertainty in the pressure sensors. For either sensor, δN_p, δN_t, and δN_v become aprroximatley comparable. When $P_f \leq 1/4\ P_{fs}$ for a given sensor, the uncertainty is dominated by the intrinsic sensor error, which is $\geq$ 0.05%. However, when the pressure is higher, or a combination of sensors is used, the error in the number adsorbed due to error in the volume and temperature can become significant. In this case, more accurate ghs temperature control and more accurate aghs volume determination will improve the overall ghs uncertainty ($\delta N_{ads}/N_{ads}$). However, uncertainty in neither V_{ghs} nor T_s can be reduced much further without signficant effort.

4. Future Work

Immediate plans include completion of the hardware and software (system control program) in the current configuration. When

completed, the system will be more than adequate to perform multilayer isotherms of N_2 on graphite, and can be used to address the questions raised by our x-ray studies of this sytem (see Chap. IV, Sec. F.2).

Future plans include the two system hardware upgrades outlined above. Pending funding, the A/D board will be replaced by one an order of magnitude more accurate. The resistors in the Si diaphragm constant current supply source will also be replaced. These two improvements will make our system comparable to the of Suter *et al.*[112] and capable of state of the art measurements.